Final Report for Period: 09/2006 - 08/2007
Submitted on: 12/18/2007
Principal Investigator: Book, Wayne J.
Award ID: 0121663
Organization: GA Tech Res Corp - GIT
Title:
ITR/PE+SY Digital Clay for Shape Input and Display

Project Participants

Senior Personnel

Name: Book, Wayne
Worked for more than 160 Hours: Yes
Contribution to Project:

Name: Allen, Mark
Worked for more than 160 Hours: Yes
Contribution to Project:

Name: Rosen, David
Worked for more than 160 Hours: Yes
Contribution to Project:

Name: Rossignac, Jarek
Worked for more than 160 Hours: Yes
Contribution to Project:

Name: Ebert-Uphoff, Imme
Worked for more than 160 Hours: Yes
Contribution to Project:
Performs research on kinematic architecture for digital clay. Prof. Ebert-Uphoff was on educational leave for the past 2 years, but continued to supervise her students involved in this project through weekly or biweekly meetings.

Name: Shaw, Chris
Worked for more than 160 Hours: No
Contribution to Project:
Dr. Shaw has collaborated with Dr. Rossignac towards the design and validation of several interaction paradigms that were prototyped using a Phantom and two 6DoF trackers. He has expertise in 2-hand interaction for visualization and shape editing. He has received 1/2 month support from this grant that has been initially allocated to Dr. Mynatt, who had to reduce her involvement due to personal reasons.

Name: Glezer, Ari
Worked for more than 160 Hours: Yes
Contribution to Project:
Co-PI on proposal. Performs fluidics research to actuate digital clay.

Post-doc

Name: Yuan, Guang
Worked for more than 160 Hours: No
Contribution to Project:

Graduate Student

Name: Kim, ByungMoon

Worked for more than 160 Hours: Yes

Contribution to Project:

Mr. Kim has worked on the design of the haptic feedback filter and of the mathematical formulation of the behavior of the Digital Clay in response to user gestures. He is a PhD candidate in the College of Computing and is funded through this grant.

Name: Gargus, Joshua

Worked for more than 160 Hours: No

Contribution to Project:

Mr. Gargus has worked on the interface of the clay model with a Phantom haptic device and on the simulation of the forces and reactions to user-pressure on the surface fo the Digital Clay.
He was funded through the spring and summer of 2002 by a Seed Grant from the GVU Center at Georgia Tech.

Name: Llamas, Ignacio

Worked for more than 160 Hours: Yes

Contribution to Project:

Mr. Llamas has worked on the exploration of shape-editing primitives that can be controlled by simple gestures and change the shape of the surface. He has implemented several such techniques using an in terface with 2 trackers. He was funded in the summer of 2002 by a Seed Grant from the GVU Center at Georgia Tech. He is now funded by the project as a Ph.D. student.

Name: Nguyen, Austina

Worked for more than 160 Hours: Yes

Contribution to Project:

Austina is a Graduate Research Assistant in the School of Mechanical Engineering at Georgia Tech. Her responsibilities include the design and fabrication of the deformable kinematic structure that will compose the interior of 'digital clay.'
She presented her Masters thesis, supported by this award, in April 2004 and will graduate in Summer 2004.

Name: Bosscher, Paul

Worked for more than 160 Hours: Yes

Contribution to Project:

Paul worked on the kinematic architecture for the digital clay
(with Dr. Ebert-Uphoff). He completed his Master degree on the topic in Spring 2003. Paul was supported by this award for one year and by a NDSEG doctoral fellowship the second year.

After his work on digital clay Paul pursued his Ph.D. on a different topic (cable-driven robots) and is now an Assistant Professor at Ohio University.

Name: Zhu, Haihong

Worked for more than 160 Hours: Yes

Contribution to Project:

Analyzed the dynamic response of fluid actuation of display concepts. Constructed physical prototypes and experimented with them.

Name: Askins, Stephen

Worked for more than 160 Hours: Yes

Contribution to Project:

Mr. Askins is supported by discretinary funds of the P.I. while he is studying in France at Georgia Tech Lorraine. He has been creating SimuLink models of arrays of cells such as would be used in digital clay. The simulations incorporate example control algorithms, valve properties, and interaction between adjacent cells.

Name: Dessolin, Samuel

Worked for more than 160 Hours: Yes

Contribution to Project:

Mr. Dessolin is a French student participating in the joint program between Georgia Tech and ENSAM in France. He is working cooperatively with Mr. Askins. He is currently using finite element techniques to analyze the effects of membrane covers for digital clay. The resulting shape and the nature of the interaction between neighboring cells is under study. In the Fall of 2002 he

will move to Atlanta to complete his M.S. degree with a thesis on a related topic. During this time he will be supported by discretionary funds available to the P.I.

Name: Bai, Jing

Worked for more than 160 Hours: Yes

Contribution to Project:

Name: Short, Dan

Worked for more than 160 Hours: Yes

Contribution to Project:

Name: Wolff, Sebastien

Worked for more than 160 Hours: Yes

Contribution to Project:

Sebastien first worked on alternative kinematic structures for digital clay. Then he worked on a different aspect of digital clay, namely assembly sequence generation for shape display, which became his Ph.D. topic. He completed his Ph.D. work in August 2006.

While working on Digital clay Sebastien was supported through an NSF IGERT for 1 year and by this grant for 2 years.

Name: Wang, Hongqing

Worked for more than 160 Hours: Yes

Contribution to Project:

Hongqing Wang is a Ph.D. student in Mechanical Engineering. He is developing analysis and synthesis methods for the kinematic structure of digital clay devices.
He presented his Ph.D. proposal in March 2004 on his research that is supported by this award.

Name: Riechel, Andrew

Worked for more than 160 Hours: Yes

Contribution to Project:

Andrew investigated the development of an alternative architecture for Digital Clay, consisting of an array of (n x n) pins that are raised and lowered by only (2 x n) actuators, using a mechanical `and' gate. He was funded by this grant for 1 semester.

Name: Whited, Brian

Worked for more than 160 Hours: Yes

Contribution to Project:

Brian is a Computer Science MS student working on the project but not funded by it. He is working with Rossignac and Shaw.

Name: Brown, Gordon

Worked for more than 160 Hours: Yes

Contribution to Project:

Gordon is a Computer Science student working with Rossignac and Shaw but not funded by the project.

Name: Wu, Sharon

Worked for more than 160 Hours: Yes

Contribution to Project:

Sharon Wu has developed elastomeric MEMS technology for pneumatic microbellows

Name: Anderson, Theodore

Worked for more than 160 Hours: Yes

Contribution to Project:

Designing, modeling, and manufacturing formable surfaces for digital clay devices.

Name: Becker, Gerritt

Worked for more than 160 Hours: Yes

Contribution to Project:

Undergraduate Student

Name: Quicksall, Jake

Worked for more than 160 Hours: No

Contribution to Project:

Jake supported the work of Andrew Riechel by building simple mechanical prototypes.

Name: Powel, Alex

Worked for more than 160 Hours: Yes

Contribution to Project:

Alex is a Computer Science undergraduate student working with Rossignac and Shaw for the duration of 12 months funded by the project.

Name: Shieh, Joy

Worked for more than 160 Hours: Yes

Contribution to Project:

Joy is an undergraduate Computer Science Student working on the project with Rossignac and Shaw but without project funding.

Name: Carter, Elizabeth

Worked for more than 160 Hours: Yes

Contribution to Project:

Name: Sarcione, Lynn

Worked for more than 160 Hours: No

Contribution to Project:

Ms. Sarcione studied the applicability of Field Programmable Gate Arrays programmed in LabVIEW to the control of an array of position actuators. This was considered as an alternative should conventional computers not be adequately fast. For the scale of our prototypes, the FPGA was not necessary.

Technician, Programmer

Other Participant

Research Experience for Undergraduates

Name: Indech, Jennifer

Worked for more than 160 Hours: No

Contribution to Project:

Ms. Indech has recently jointed the project through an REU supplement. She is creating surfaces that immitate possible surfaces for digital clay. This consists of examining alternatives, designing a shape with an array of the elements on a CAD package, downloading the design to a stereo lithography machine for fabrication. She will then experiment with the surfaces and with alternate coverings for the surface. The experiments will be related to the spatial frequency composition of the shape. She has also assisted other parts of the project with a literature search and collecting data on materials.

Years of schooling completed: Junior

Home Institution: Same as Research Site

Home Institution if Other:

Home Institution Highest Degree Granted(in fields supported by NSF): Doctoral Degree

Fiscal year(s) REU Participant supported: 2002

REU Funding: REU supplement

Name: Shieh, Jessie

Worked for more than 160 Hours: Yes

Contribution to Project:
Worked with Jarek Rossignac. Conducted research on a new space warp operator and was responsible for the Internet dissemination of the project's results.

Years of schooling completed: Junior
Home Institution: Same as Research Site
Home Institution if Other:
Home Institution Highest Degree Granted(in fields supported by NSF): Doctoral Degree
Fiscal year(s) REU Participant supported: 2003
REU Funding: No Info

Name: Powell, Alex
Worked for more than 160 Hours: Yes
Contribution to Project:
A new REU student, who has replaced Jessie Shieh and is responsible for completing the design and implementation of a new space warp operator.

Years of schooling completed: Junior
Home Institution: Same as Research Site
Home Institution if Other:
Home Institution Highest Degree Granted(in fields supported by NSF): Doctoral Degree
Fiscal year(s) REU Participant supported: 2003
REU Funding: No Info

Name: O'Connor, Kevin
Worked for more than 160 Hours: Yes
Contribution to Project:
Mr. Kevin O'Connor has been working on the development of a compact, self contained actuator module.

Years of schooling completed: Junior
Home Institution: Same as Research Site
Home Institution if Other:
Home Institution Highest Degree Granted(in fields supported by NSF): Doctoral Degree
Fiscal year(s) REU Participant supported: 2003
REU Funding: No Info

Name: Shukla, Ashutosh
Worked for more than 160 Hours: No
Contribution to Project:
Assisted Jennifer Indech and Wayne Book in conducting surveys of the perception of digital clay parameter.

Years of schooling completed: Junior
Home Institution: Same as Research Site
Home Institution if Other:
Home Institution Highest Degree Granted(in fields supported by NSF): Doctoral Degree
Fiscal year(s) REU Participant supported: 2003
REU Funding: No Info

Name: Bergeron, Anne
Worked for more than 160 Hours: No
Contribution to Project:
Just began. Will assist Wayne Book with control of prototypes.

Years of schooling completed: Junior
Home Institution: Same as Research Site
Home Institution if Other:

Home Institution Highest Degree Granted(in fields supported by NSF): Doctoral Degree
Fiscal year(s) REU Participant supported: 2003
REU Funding: No Info

Name: Dillard, Daniel
Worked for more than 160 Hours: No
Contribution to Project:

Years of schooling completed: Sophomore
Home Institution: Same as Research Site
Home Institution if Other:
Home Institution Highest Degree Granted(in fields supported by NSF): Bachelor's Degree
Fiscal year(s) REU Participant supported: 2002
REU Funding: No Info

Name: Davis, Harrell
Worked for more than 160 Hours: Yes
Contribution to Project:

Years of schooling completed: Sophomore
Home Institution: Same as Research Site
Home Institution if Other:
Home Institution Highest Degree Granted(in fields supported by NSF): Bachelor's Degree
Fiscal year(s) REU Participant supported: 2003 2003
REU Funding: REU supplement

Name: Michaud, Alexander
Worked for more than 160 Hours: No
Contribution to Project:
Continued our work on the design and manufacture of digital clay kinematic structures. Worked for one semester as an REU student.

Years of schooling completed: Other
Home Institution: Same as Research Site
Home Institution if Other:
Home Institution Highest Degree Granted(in fields supported by NSF): Doctoral Degree
Fiscal year(s) REU Participant supported: 2005 2004
REU Funding: No Info

Organizational Partners

Other Collaborators or Contacts

Activities and Findings

Research and Education Activities: (See PDF version submitted by PI at the end of the report)

Findings: (See PDF version submitted by PI at the end of the report)

Training and Development:

The Ph.D student and the research staff participating in this research have the chance to develop skills in advanced MEMS design and fabrication techniques. They could also broaden their view through the cooperation with the other research teams involved in the digital clay project and gain from the highly interdisciplinary research areas of fluid mechanics, robotics and control, rapid prototype and computer graphic technology.

The 3 Computer Science undergraduates involved in this project have been taking an active part in the research. In fact, Ignacio Llamas has been accepted to the PhD program in CS at Georgia Tech and will continue working on the project. He has developed a strong taste for research and an excellent handle on the prior art on 3D sculpting.

The Digital Clay project has provided an umbrella for involving two PhD, two Master's, and two undergraduate students from the College of Computing in exciting research projects. In addition to the research aspects of each investigation, these students experienced successful interdepartmental collaborations and the production of tangible artifacts.

Samuel Dessolin completed the MS thesis leading to his MS in Mechanical Engineering Degree. He has returned to France to seek employment. Steven Askins will complete his thesis and degree before the end of this second year. Haihong Zhu has passed his Ph.D. qualifying exam and will write his proposal in the coming months, his thesis on the topic of this research. Two undergraduates, Jennifer Indech and Ashutosh Shukla have been supported as REU students and have entered graduate school. Lynn Sarcione served as an REU under this project and evaluated the applicability of FPGA devices for controlling the cells of Digital Clay. She is in the process of applying to graduate school in Mechanical Engineering. Haihong Zhu received his Ph.D. degree in August, 2005 and then served as a post doctoral fellow continuing on this project.

Over the past three years, three graduate students, Paul Bosscher, Sebastien Wolff and Andrew Riechel, and one undergraduate student, Jake Quicksall, have been involved on the kinematics side of this project. (The three graduate students were funded by the Clay project for 9-12 months each, but for most of them their involvement with the project extended far beyond that period of time.) All of these students learned about interdisciplinary research and about the development of new types of mechanisms, from brainstorming to simulation and construction of simple prototypes to test their ideas. Sebastien Wolff started work on this project investigating alternate architectures. More recently he has focused on alternates of shape display, namely assembly sequences for automated assembly of identical blocks. He has obtained a M.S. and has completed all requirements for a Ph.D., which he will be receiving in December. During this process he has learned how to work on interdisciplinary teams, brainstorm, build prototypes, write software, and more.

Being involved in this interdisciplinary research has shaped the students and has helped them to develop a career in a related area, as highlighted by their track record:
ò Paul Bosscher won a NDSEG fellowship and is anticipated to obtain his Ph.D. in December 2004. He has already accepted a position as faculty member in Mechanical Engineering at Ohio University starting in January 2005.
ò Andrew Riechel, who graduated with a M.S. degree in May 2004, will work on the design of mechanisms at Harris Corporation starting in June 2004.
ò Sebastien Wolff completed his Ph.D. on one aspect of this project, namely the study of assembly sequences for robots seeking to create shapes by assembling building blocks.
ò Jake Quicksall, the undergraduate involved in this research, has accepted a position at JPL where he will most likely work on Mechatronic systems. Furthermore, JPL will fund his return to graduate school in 2005 to get a M.S. degree,
Thus it is clear that this project has already greatly impacted the career and life of these four students and that it has helped them build a solid foundation for future success in related areas. In turn, these students will bring their multidisciplinary training and way of thinking to a variety of workplaces, making an impact there as well.

Austina Nguyen presented her Masters thesis in April 2004 and is completing her thesis at present. Hongqing Wang presented his Ph.D. proposal in March 2004. Two undergraduate students, Daniel Dillard and Harrell Davis, have worked on this project as REU's. Both are juniors in mechanical engineering and are contemplating graduate school. Hongqing Wang defended his Ph.D. dissertation in November 2005 and graduated in December. Ted Anderson has worked on the project during calender year 2006 and expects to graduate with his MSME degree in December 2006. During the summer of 2005, one undergraduate student, Elizabeth Carter, worked on the project during her last semester before graduating with a BSME degree. Simultaneously, a graduate student, Gerritt Becker, worked on the project as part of his Masters degree requirements at the Technical University of Darmstadt in Germany.

Daniel Short has developed an experimental set up for time-dependent diagnostics of the digital clay fluidic system. During the current reporting period, Mr. Short has gained considerable experience in the design and implementation of his sophisticated sensors and actuators and real-time digital data acquisition. Mr. Kevin O'Connor has been working on the development of a compact, self contained actuator module.

Mr. Short and O'Connor have had formal training in stereolithographic rapid prototyping technology using 3D Systems software and hardware. They have also expanded their skills with SolidEdge, and SolidWorks. Mr. Short expects to take his PhD qualifiying exam in fall 2003 and Mr. O'Connor expects to complete his BS degree in fall of 2003 and pursue a graduate degree.
Opportunities include the development, design and construction of a sophisticated, fully instrumented fluidic actuation system including the classification and characterization of the working fluid (e.g., viscosity, chemical compatibility, dissolution of gasses, vapor pressure, etc.), investigation of the primary and secondary flows within the system to further understand the flow topology. Dave Garth completed his MS degree working on these problems.

Jing Bai has passed her preliminary examination.

Guang Yuan has been trained on and has access to laser equipment, injection-molding machines, etc. She has been gaining skills in advanced MEMS fabrication techniques and will continue research and fabrication work on the PZT hysteretic valve and fluidic cell.

Xiaosong (Sharon) Wu has passed the 1st part of her qualify examination. She has also been trained on and has access to clean room. She has been gaining skills in advanced MEMS fabrication techniques and will continue research and fabrication work on the fluidic cell. She has presented her proposal for her Ph.D. thesis which was approved and she should be graduating soon.

Opportunities include the development, design and construction of a sophisticated, fully instrumented fluidic actuation system including the classification and characterization of the working fluid (e.g., viscosity, chemical compatibility, dissolution of gasses, vapor pressure, etc.), investigation of the primary and secondary flows within the system using flow visualization and advanced optical diagnostics (i.e., small-scale particle image velocimetry, PIV) to further understand the flow topology.

Outreach Activities:

Wayne Book and Imme Ebert-Uphoff are the faculty advisors of the robotics club on the Georgia Tech campus, the RoboJackets. Together they supervise several outreach activities to local high schools. (1) PI Book and Co-PI Ebert-Uphoff serve as the primary faculty advisors of the RoboJackets, the Robotics Club on the GT campus. The club is very active in several national and international activities, as well as outreach programs to local high schools. About 30 students from Georgia Tech are involved in the club, mainly undergraduates.
Dr. Book is the advisor for the FIRST group which has mentored a local high school team in the FIRST Robotics Competition. The high school won first place in the Peachtree Regional and performed well at the National Competition. The Georgia Tech students also conducted tutorials for approximately 100 students each week for six weeks before the competition began in the basic principles they would need to design and build their robot. They were very active in bringing the regional competition here two years ago and the National competition this year.

Dr. Ebert-Uphoff is the advisor for all the other activities of the club, most notably the Lego Robot Challenge, the Intelligent Ground Vehicle Competition, the VacuBot Competition and Battle Bots. The Lego Robot Challenge is an annual workshop which brings student teams from six local high schools to Georgia Tech for an extended weekend. Schools and student teams are selected so that under-represented and female students make up a large percentage, usually 30-40%! The students are first trained in the use of the Lego Mindstorm kits, learn how to build mobile robots that can perform certain tasks and finally have the robots compete in the Final Challenge.

The other activities of the club, such as the Intelligent Ground Vehicle Competition, are directed towards engineering and computer science students at Georgia Tech, providing them with fun & hands-on experience in robotics and mechatronics throughout the year. These activities help the students early in their studies to see the relevance of the material learned in their classes and to connect that material to real-world systems.

The Digital Clay Project has been promoted throgh web sites, conference presentations, publications, and lectures in graphics classes at Georgia Tech.

Journal Publications

P. Bosscher and I. Ebert-Uphoff, "Digital Clay: Architecture Designs for Shape-Generating Mechanisms", Proceedings of the 2003 IEEE International Conference on Robotics and Automation, Taipei, Taiwan, September 2003, p. 834, vol. , (2003). Published,

P. Bosscher and I. Ebert-Uphoff, "A Novel Mechanism for Implementing Multiple Collocated Spherical Joints", Proceedings of hte 2003 IEEE International Conference on Robotics and Automation, Taipei, Taiwan, September 2003, p. 336, vol. , (2003). Published,

Jarek Rossignac, Mark Allen, Wayne J. Book, Ari Glezer, Imme Ebert-Uphoff, Chris Shaw, David Rosen, Stephen Askins, Jing Bai , Paul Bosscher, Joshua Gargus, ByungMoon Kim, Ignacio Llamas, Austina Nguyen, Guang Yuan, Haihong Zhu, "Finger Sculpting with Digital Clay: 3D Shape Input and Output through a Computer-Controlled Real Surface", Shape Modeling International Conference in Korea, Seoul, p. 1, vol. May, (2003). Published,

Haihong Zhu and Wayne J. Book, "Control Concepts for Digital Clay", Proceedings of the 7th IFAC Symposium on Robot Control (SyRoCo 2003), p. 405, vol. 2, (2003). Published,

Wayne Book and Davin Swanson, "Reach Out And Touch Someone: Controlling Haptic Manipulators Near And Far", Proceedings of 7th IFAC Symposium on Robot Control, SYROCO 2003, p. 13, vol. 1, (2003). Published,

Askins, Steven and Wayne J. Book, "Digital Clay: User Interaction Model for Control of a Fluidically Actuated Haptics Device", First International Conference on Computational Methods in Fluid Power Technology, p. 15, vol. 1, (2003). Published,

Zhu, Haihong and Wayne J. Book, "Speed Control and Position Estimation of Small Hydraulic Cylinders for Digital Clay Using PWM Method", Japan-US Conference on Flexible Automation, p. 1, vol. , (2004). Published,

Zhu, Haihong and Wayne J. Book, "Practical Stucture Design and Control for Digital Clay", 2004 ASME International Mechanical Engineering Congress and Exhibition, p. 1051, vol. , (2004). Published,

Book, Wayne J. and Davin K. Swanson, "Reach Out and Touch Someone: Controlling Haptic Manipulators Near and Far", Annual Reviews in Control, p. 87, vol. 28, (2003). Published,

Ignacio Llamas, Byungmoon Kim, Joshua Gargus, Jarek Rossignac, and Chris D. Shaw, "Twister: A space-warp operator for the two-handed editing of 3D shapes", ACM Transactions on Graphics (TOG), Proc. ACM SIGGRAPH, p. 663, vol. 22, (2000). Published,

Ignacio Llamas, Alex Powell, Jarek Rossignac, Chris Shaw, "Bender: Deforming and animating 3D shapes by bending and twisting a virtual ribbon with both hands", ACM Symposium on Solid and Physical Modeling, p. 89, vol. , (2005). Published,

Rosen, D.W., Nguyen, A., and Wang, H, "On the Geometry of Low Degree-of-Freedom Digital Clay Human-Computer Interface Devices", Proceedings ASME Computers and Information in Engineering Conference, Chicago, Sept. 2-6, 2003, p. 48295, vol. DETC, (2003). Published,

ByungMoon Kim and Jarek Rossignac, "GeoFilter: Geometric Selection of Mesh Filter Parameters", Eurographics, p. 295, vol. , (2005). Published,

Ignacio Llamas, Jarek Rossignac, "FlowFixer: Using BFECC for Fluid Simulation", Eurographics Workshop on Natural Phenomenon, p. 51, vol. , (2005). Published,

Haihong Zhu, Wayne Book, "Structure and control for cells of Digital Clay", ASME Journal of Dynamic Systems, Measurement, and Control, p. , vol. , ( ). Submitted,

Xiaosong Wu and Mark Allen, "Kinematically-Stabilized Microbubble Actuator Arrays", Proceedings of IEEE Micro Electro Mechanical Systems, p. 554, vol. , (2005). Published,

ByungMoon Kim, Yingjie Liu, Ignacio Llamas, Jarek Rossignac, "Advections with Significantly Reduced Dissipation and Dif", IEEE Transactions on Visualization and Computer Graphics, p. , vol. , ( ). Accepted,

S. Wolff, I. Ebert-Uphoff, "Preliminary Results on Generating Assembly Sequences for Shape Display", ASME International 26th Computers and Information in Engineering Conference, p. , vol. , (2006). Published,

Rossignac, J, "Shape complexity", VISUAL COMPUTER, p. 985, vol. 21, (2005). Published, 10.1007/s00371-005-0362-

Rossignac, J; Kim, JJ; Song, SC; Suh, KC; Joung, CB, "Boundary of the volume swept by a free-form solid in screw motion", COMPUTER-AIDED DESIGN, p. 745, vol. 39, (2007). Published, 10.1016/j.cad.2007.02.01

Kim, B; Liu, Y; Llamas, I; Jiao, X; Rossignac, J, "Simulation of bubbles in foam with the volume control method", ACM TRANSACTIONS ON GRAPHICS, p. , vol. 26, (2007). Published, 10.1145/1239451.123954

Kim, B; Rossignac, J, "GeoFilter: Geometric selection of mesh filter parameters", COMPUTER GRAPHICS FORUM, p. 295, vol. 24, (2005). Published,

S. Wolff, I. Ebert-Uphoff and H. Lipkin, "Statically Stable Assembly Sequence Generation for Many Identical Building Blocks", Journal of Computing and Information Science in Engineering, p. , vol. , (2007). Submitted,

Rosen, D.W., "Cellular structures for high stiffness, compliance, and other multifunctional applications", International Mechanical Engineering Congress and Exposition, p. , vol. , (2005). Published,

Rosen, D.W. and Nguyen, A.N., "Simulation Methods for formable crust skins of digital clay human-computer interface devices", ASME Journal of Computing and Information Science in Engineering, p. , vol. , (2005). Submitted,

Wang, H. and Rosen, D.W., "An Automated Design Synthesis Mehtod for compliant mechanisms with application to morphing wings", ASME Journal of Mechanical Desing, p. , vol. , (2006). Submitted,

Kim, B; Liu, YJ; Llamas, I; Rossignac, J, "Advections with significantly reduced dissipation and diffusion", IEEE TRANSACTIONS ON VISUALIZATION AND COMPUTER GRAPHICS, p. 135, vol. 13, (2007). Published,

Y. Chen, H. Wang, D. Rosen, J. Rossignac, "Filleting and rounding using a point-based method", ASME Design Engineering Technical Conferences, p. , vol. , (2005). Published,

X. Wu, S-H. Kim, C-H.Ji and M.G. Allen, "A piezoelectrically-driven high flow rate axial polymer microvalve with solid hydraulic amplification", IEEE Microelectromechanical systems (MEMS ?08), p. , vol. , (2008). Accepted,

X. Wu, H. Zhu, S-H Kim and M.G. Allen, "A portable pneumatically-actuated refreshable Braille cell", Tech. Dig. The 14th International Conference on Solid-State Sensors, Actuators, and Microsystems (Transducers ?07), p. 1409, vol. , (2007). Published,

X. Wu, G. Yuan, S-O Choi, Y-K Yoon and M.G. Allen, "Lateral lamination approach for multilayer piezoelectric microactuator", Tech. Dig. Solid-State Sensor, Actuator, and Microsystems Workshop (Hilton Head ?06), p. 372, vol. , (2006). Published,

H. Zhu and W. Book, "Practical Embedding and Multiplexing Large Scale Sensor Arrays for Digital Clay", Proceedings of the ASME International Mechanical Engineering Congress and Exposition, p. , vol. , (2005). Published,

H. Zhu and W. Book, "Digital Clay: Next Generation Human-computer Interface", IEEE International Conference on Robotics and Automation, p. , vol. , (2006). Published,

W. Book and H. Zhu, "Haptic Surfaces through Mechatronic Design", IEEE International Conference on Robotics, Automation and Mechatronics, p. 896, vol. , (2006). Published,

H. Zhu and W. Book, "Construction and Control of Massive Hydraulic Miniature-actuator-sensor Array", IEEE Conference on Computer Aided Control Systems Design, p. 820, vol. , (2006). Published,

H. Zhu, B. Paul and W. Book, "Control Issues of Digital Clay - Massive Hydraulic Actuator Array for Man-machine Communication", International Mechanical Engineering Congress and Exposition, p. , vol. , (2006). Published,

H. Zhu and W. Book, "Active Shielding for a Novel Sensor", International Mechanical Engineering Congress and Exposition, p. , vol. , (2007). Published,

Books or Other One-time Publications

Web/Internet Site

URL(s):

http://www.cc.gatech.edu/gvu/reports/2002/
http://www.me.gatech.edu/digitalclayproject/

Description:

ôFinger Sculpting with Digital Clayö, Joshua Gargus, Byungmoon Kim, Ignacio Llamas, Jarek Rossignac, and Chris Shaw, Technical Report GIT-GVU-02-22, October 2002.

This is a preliminary public site to share information. An internal site is dedicated to working issues.

Other Specific Products

Product Type:

Other inventions

Product Description:

The concept of digital clay, comprising a valve inflating a bladder which articulates a kinematic structure for purposes of shape input and display with or without a artificially generated haptic sensation.

Sharing Information:

Digital clay might be of use in medicine, mechanical design, aids to the visually handicapped, and many other areas.

Product Type:

Instruments or equipment developed

Product Description:

Reusable molds, bubble prototypes

Sharing Information:

Unlikely to have immediate use by others at this time.

Product Type:

Other inventions

Product Description:

A new joint mechanism was developed that implements several concentric spherical joints. The joint is described in a paper and a patent application was also filed. The paper reference is P. Bosscher and I. Ebert-Uphoff, ôA Novel Mechanism for Implementing Multiple Collocated Spherical Joints,ö to appear in the Proceedings of the 2003 IEEE International Conference on Robotics and Automation, 2003.

Sharing Information:

This joint mechanism has applications beyond digital clay, including variable geometry trusses, parallel robotic manipulators and many other robotic mechanisms.

Product Type:

Other inventions

Product Description:

A device to actuate N*N fluid actuators with 2N valves

Sharing Information:

This invention will assist in moving any device with a large number of degrees of freedom. It is particularly well suited to array structures but could also be used for other structures.

Product Type:

Software (or netware)

Product Description:

ANSYS batch program files for design/simulation of corrugated bubbles and PZT stack actuator need for hysteretic valves.

Sharing Information:

Interested parties should contact Prof. Mark Allen, ECE, Georgia Tech.

Product Type:

Other inventions

Product Description:

The new LVDT differs from traditional LVDTs which have two secondary coils and one primary coil in that it has only one each secondary and primary coil. This design was chosen because it provides many of the benefits of the traditional LVDT without some of the drawbacks. The two-coil LVDT is easy to manufacture and can be readily miniaturized (the length of the core is the length of the entire sensor).
The piston and the sensor that are be embedded into the valve cell are shown schematically in the body of the report under Findings. The primary core is excited with an AC voltage and an induced current is measured from the secondary coils. The coupling occurs through the core, which must have good ferromagnetic properties. The inner cavity of the LVDT makes up the cylinder and the piston rod makes up the core to create a piston cylinder device that has a built in position measuring system as stated above. The valve housing module is simply fabricated in two separate pieces that allow the insertion of the position measuring system. Variable coil LVDTs will also be used in future implementations. In this design, the core material does not need to have high permeability (or other desirable ferromagnetic properties), but in this case, the piston head has to be made out of a material that has good ferromagnetic properties.

Sharing Information:

Other devices with need for compactness and position measurement would benefit.

Product Type:

Interactive session demonstration at the 2004 American Control Conference

Product Description:

A demonstration of a 1x5 array of the working prototype of digital clay was demonstrated at the 2004 American Control Conference in Boston, MA.

Sharing Information:

The interactive sessions were heavily attended.

Product Type:

Technical Report

Product Description:

Sebastien J. Wolff, Imme Ebert-Uphoff, Harvey Lipkin, ``Statically Stable Assembly Sequence Generation for Many Identical Assembly Blocks", Technical Report, Georgia Tech, College of Computing, GIT-IC-07-06, October 2007.

Sharing Information:

Available on the web at http://www.cc.gatech.edu/research/reports

Product Type:

Other inventions

Product Description:

Position of the hydraulic piston is measured by capacitively coupling the piston and a film on the cylinder. An ac current is impressed across the length of the film. The resistance of the film up to the position of the piston determines the amplitude of the response. This response is processed electronically to give an accurate reading of the film positon.

Sharing Information:

Postion sensing is widely used in industry, science and consumer products. The low cost and small footprint of the sensor created results in tremendous advantages for measuring the positon of a piston and also for a stand alone sensor to measure positon. A spin-off company, Sentrinsic, LLC, has been created to commercialize this invention and several major companies have become its customers and/or have expressed interest in the product.

Product Type:

Software (or netware)

Product Description:

Matlab files to optimize the interior of a structure, and to design, animate, and statically evaluate assembly sequences.

Sharing Information:

Sharing Information: Files can be found at http://helix.gatech.edu/wolff/matlab.htm

Contributions

Contributions within Discipline:

A scheme for commanding the cells of digital clay has been devised and illustrated on a single cell constructed with conventional components. It has been examined in simulation as well. Simplified models of membrane behavior have been developed for fast dynamic simulation.

A new position sensor has been developed that can be incorporated into a fluidically actuated cylinder has been created and shown to have high accuracy at potentially low cost. Control techniques for large arrays of actuators have been developed.

A new joint mechanism was developed that implements several concentric spherical joints. This joint mechanism has applications beyond digital clay, including variable geometry trusses, parallel robotic manipulators and many other robotic mechanisms. The joint is described in a paper and a patent application was also filed.

New MEMS fabrication technologies, including laser micromachining and lamination-based polymeric approaches to microstructures, have been developed. These new technologies have been applied to the fabrication of micro-fluidic sensors and actuators, digital clay cells, and the fluidic-electronic interface. MEMS technology, including dicing and photo patterning have been employed for the fabrication of micro PZT stack actuators for hysteretic valves, fluid sensors and actuators, digital clay cells as well as the fluidic-electronic interface. MEMS fabrication technologies, including declined exposure, Parylene coating have been applied to the fabrication of micro-bubble actuators.

MEMS technology, including dicing and photo patterning have been employed for the fabrication of micro PZT stack actuators for hysteretic valves. MEMS fabrication technologies, including inclined exposure, micromolding, and parylene coating have been applied to the fabrication of micro-bubble actuators.

The TWISTER model for 3D shape deformation developed by the Finger Sculpting team offers a significant improvement over previous models of 3D warps, which were limited to translational constraints only, and did not accommodate orientation constraints.

The work on Bender provides the theoretical basis for solving the tearing problem that is intrinsic to all wire-based warps. The tearing problem results from the following situation. Imagine two points, P and Q, on the surface that are close to one another. Let P' be the point on the wire that is the closest to P. Let Q' be the point on the wire that is the closest to Q. As the wire is deformed by the user, P will tend to follow P' and Q will tend to follow Q'. If P' and Q' lie on different portions of the wire, the wire deformation may pull them apart by an arbitrary distance, pulling P away from Q. Instead of restricting the influence of the wire on a point P to only its closest point P', we blend the influence of all points on the wire where the distance to P goes through a local minimum. We have proven that when a bi-arc is used as wire, only 2 such local minima exist.
The work on Poker has demonstrated that PDEs can be solved directly on a triangle mesh representation of a surface and that the connectivity graph of the mesh may be used to localize the solver. This initial work demonstrate that in some Direct Human-Shape interaction applications PDEs may be solved in realtime.

The experiments with the Tritops prototype have opened new opportunities for mapping small three-dimensional gestures with limited range into parameters that control the six degrees of freedom of a control pose. A lower dimensional version illustrating this challenge would be the use of two short pistons (one per finger) to control the height and orientation of an object on a large screen. The Tritops prototype represents an exploration of a new part of the haptic display design space.

The math models for predicting formable crust shape contribute to the understanding of highly parallel mechanisms. These models represent one approach to modeling highly parallel mechanisms and to computing their forward and inverse kinematics. This work also impacts the area of compliant mechanism design and analysis.

The focus of the fluidic component of the project is to develop the means and medium for actuation of and sensing at the digital clay surface. It is anticipated that fluidic actuation will enable the creation of a three-dimensional haptic computer interface. The fluid mechanics research will lead to better understanding of the fundamental flow mechanisms within small scale fluidic channels, tubes and passages and will shed light on

the stability characteristics of the entire system.

In the context of shape display with identical building blocks, a multi-hierarchical rule-based system was developed that can develop statically stable assembly sequences in a time-feasible manner. Previous methods could not be applied to obtain statically stable assembly sequences. This rule-based system was tested on a number of structures, and is described in a submitted journal paper. The differences between generating assembly sequences by virtually assembling or disassembling the structure were also derived and presented in a conference paper.

Contributions to Other Disciplines:

Stereo-lithography techniques together with subsequent molding from liquid elastic material into structures or as transferring molds, traditional press molding, injection molding and polymer coating have been carried out to fabricate structure and actuating parts. All these parts, in a macro-scale model of the clay, will be used in the first prototype being constructed now.

The collaborations between students in CS and ME has demonstrated that 3D simulations may be developed for very complex articulated mechanisms, involving hundreds of moving parts and springs and that these simulations provide results that are sufficiently accurate for exploratory design tasks.

It is anticipated that the digital clay project will have an impact on medical hardware, consumer electronics, and educational systems.
It is anticipated that the outcome of the project will pave the way towards the implementation of fluidic drivers in other small scale mechanical systems (e.g., MEMS).

The work on Bender opens the avenue to extremely intuitive and powerful human-shape interaction, not previously possible. This interaction style is currently tested in two settings. The first one is in the context of surgery planning, where surgeons wish to explore alterations of the model of a surgically-created vein junction in an attempt to balance the flow of blood to both lungs. Preliminary tests involving surgeons from Emory University Medical School have defined a road map for developing additional functionality.

Contributions to Human Resource Development:

A large number of graduate and undergraduate students in mechanical engineering, electrical engineering and computer science are involved with this highly interdisciplinary project. These students are learing about research in their disciplines and they are learing how to cooperate with other disciples. They will be receiving degrees in their respective fields with their work on this project fulfilling one of their degree requirements (except for undergraduates). The undergraduates have expressed an interest in graduate study and we expect their work here to encourage and enable this work. Two undergraduate students, Harrell Davis and Alex Michaud, have worked on this project as REU's. Harrell is a senior and is contemplating graduate school. Alex is a now a graduate student at Georgia Tech.

Being involved in this interdisciplinary research has provided all the students involved with a very unique and valuable experience. Many of them are already beginning careers in related areas û see examples of the four students involved in the kinematics area under 'Opportunities for training and development' above û, bringing their multidisciplinary training and way of thinking to a variety of workplaces, making an impact there as well.

The Ph.D student and the research staff participating in this research have the chance to develop skills in advanced MEMS design and fabrication techniques. They could also broaden their view through the cooperation with the other research teams involved in the digital clay project and gain from the highly interdisciplinary research areas of fluid mechanics, robotics and control, rapid prototype and computer graphic technology.

Contributions to Resources for Research and Education:

Matching funds for this project have expanded our resources in the rapid prototyping of mechancial systems by partially funding the purchase of a new, high resolution SLA machine.

Contributions Beyond Science and Engineering:

The broader impacts of Digital Clay research include education, assistance for the visually impaired, medical applications, international cooperation and industry linkage.

In particular the digital clay concept has great potential for the visually impaired in displaying mathematical functions as shapes with much greater ease than previously.

The twister model may be useful as a new 3D sculpting tool for artistic and entertainment applications.

Categories for which nothing is reported:

Organizational Partners
Any Book

FINDINGS

Overview

Findings are presented in the same order as activities: The conceptualization of basic approach from a kinematic and structural viewpoint by Imme Ebert-Uphoff and her student is presented first in Section 1. The MEMS research produced valves and actuators which were a basic component of implementation and thus Mark Allen's detailed report is presented second, Section 2. Next, the work by David Rosen studying how one of the implementations could be manufactured is presented in Section 3. Ari Glezer and his student, Section 4, present studies of the fluid mechanics issues in an implementation using fluid power for an implementation. The production of an integrated device that is capable of communicating with both the user and various computer programs is then presented as composed by Wayne Book and his student in Section 5. Finally, shape creation and modification approaches that might employ the integrated device are presented by Jarek Rossignac in Section 6. This last presentation could have arguably been presented first, but some of the devices used in that research are more easily understood if it is last.

Section 1

Assembly Sequence Generation for Shape Display (Ebert-Uphoff)

Comparing Assembly versus Disassembly: The first major finding in this work was the identification of the difference between generating an assembly sequence by *assembly* versus *disassembly* according to a single criterion. Analysis was performed by comparing assembling the lowest block (small Z) at each step, and disassembling the highest block at each step then reversing the order. Disassembly has generally been preferred in past research because it guarantees that no dead-ends due to accessibility or connectivity will occur. Interestingly, this research showed that generally speaking, using assembly rules is preferable from a static stand-point. Critical assembly groups (defined in the conference paper) lead to changes in direction, and therefore cantilever beams. Assembly rules will assemble all possible blocks prior to these critical assembly groups, which allows for better load distribution in supporting the cantilever. Therefore, statically speaking, assembly should be preferred.

1.1 A time-feasible algorithm for Assembly Sequence Generation: The main contribution of this work was to make assembly sequence generation for a large number of parts time-feasible. Sebastien Wolff introduced a multi-hierarchical assembly rule system to solve this problem. One key feature is that one can use assembly rules (virtually assemble one block at a time) or disassembly rules (virtually remove one block at a time then reverse the overall order) interchangeably, with either one leading to assembly sequences. Combinations are also possible. For instance in Figure 1.1, assembly rule 1 might be applied first, and disassembly rule 2 could be applied second. The result is two intermediary structures that only require a reduced task to assemble/disassemble from one to the other.

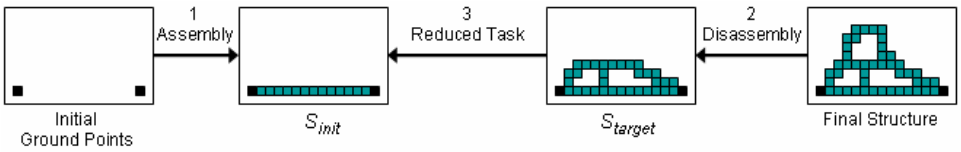

Figure 1.1. Example of Combining Assembly and Disassemby Rules

Three "levels" of rules are established. Low-level rules enforce constraints by observing the structure and determining which blocks *can* be assembled / disassembled next. Mid-level rules are rules which take in a structure, and at each step determine which block *should* be assembled (disassembled) next according to static considerations, after calling the low-level rules to determine which blocks *can* be assembled next. While an entire structure can be assembled by mid-level rules, each step considers only which block is assembled next, without considering future steps. High-level rules are rules which take a structure and at each step identify a *portion* of the structure that should be assembled next. The portion of the structure, which consists of one or more blocks, can then be assembled by applying a mid-level rule.

1.1.2 Typical Time Required by Algorithm: The run-time of the algorithm consists of the time for assembly sequence *generation* and the time for *testing* the sequence for static stability. The time required to *generate* an assembly sequence is very small. For example for typical mid-level rules, the entire assembly sequence generation takes less time than a *single* static stability test of the structure. Thus the critical criterion for algoriithm time is the number of static tests that have to be performed. While previous methods would need to perform static stability testing many times for every single block selection, our approach typically requires the *minimal* number of static tests. Specifically, as a result of the open-loop approach, for a structure with N blocks, our algorithm typically only requires static stability *testing* N times, namely one test for each step of the final assembly sequence.

1.2 Performance of Rules: After establishing the overall rule-based system, the bulk of the work was in developing, analyzing, and testing the rules on a large number of sample structures, according to the procedure described under "Activities" above. The overall finding was that one high-level rule performed so well that it was recommended as the single rule to apply in all situations. Other rules should only be applied in the unlikely scenario that this rule fails. The high-level rule in question, Connect_Ground_Local_Recursive_Unique_Close, should be applied with the mid-level rule Disassemble_D_Solid_Local. Table 1 shows how this rule ranked among the 27 rules that were tested extensively. This table indicates that the average performance of this rule (over all tested structures) was the best for both moments and forces, and its worst-case performance (over all tested structures) was also better than the worst-case performance of every other rule. Further details and numerical results are presented in the journal paper and the dissertation by Sebastien Wolff.

Table 1.1. Sample Average and Worst-Case Rule Rankings

	Moments		Forces	
	Rank of Average	Rank of Worst-Case	Average Rank	Rank of Worst-Case
MID-LEVEL:				
assemble_random	24	25	24	19
disassemble_random	27	27	27	27
disassemble_solid_d	15	14	3	4
assemble_d_z	5	3	8	12
disassemble_d_z	3	4	9	13
assemble_d_solid	6	6	4	7
disassemble_d_solid	4	2	6	7
HIGH-LEVEL, WITH ASS._D_SOLID:				
C. G. L. Recursive Unique	7	8	2	**1**
C. G. L. Recursive Close	2	5	5	**1**
C. G. L. Rec. Close Unique	**1**	**1**	**1**	**1**

Section 2

Development of Actuators for Scalable Arrays (Allen)

2.1 Development of microfluidic valves:

2.1.1 Piezoelectric multilayer actuator

A design of 150 μm wide PZT stacks with electrodes on both sides separated by a 165 μm wide SU-8 epoxy pillar was utilized. The fabrication process consists of dicing of a high-d_{33} piezoelectric coefficient lead zirconate titanate (PZT) material, photolithographic high-aspect-ratio SU-8 definition of electrical isolation, metallization, laser micromachining for electrical isolation and micromolding of epoxy in order to fortify the structure by filling the gap between PZT grooves.

Alternatively, An electrically conductive polymer composite (ECPC, silver-PMMA: 40 vol% Ag) has been utilized for making moldable electrodes in order to simplify the fabrication process. The optimized fabrication scheme consists of dicing, photolithography and micromolding of conductive polymer electrodes. Backside and inclined UV exposure has been exploited to secure the 1mm-thick SU-8 pillar definition of internal electrodes and to prevent the formation of a tapered SU-8 pillar shape that allows electrical short paths. Figure 2.1 shows an electrically isolated PZT stack actuator by laser micromachining. Figure 2.2 shows an electrically isolated PZT stack actuator by micromolding of ECPC electrode.

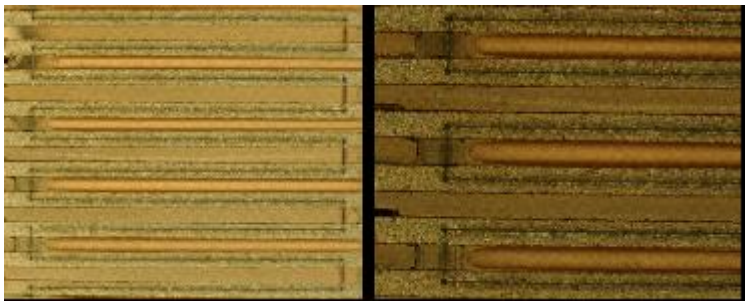

Figure 2.1 Optical microscopy image of metal coated PZT grooves filled with SU-8. (Right) magnified image of the fabricated PZT grooves.

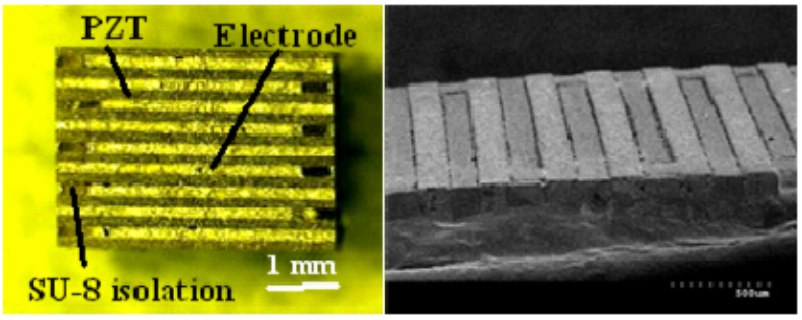

(a) (b)

Figure 2.2 (a) Optical microscopy image of a 10-layer PZT actuator with conductive polymer electrode, (b) scanning electron microscopic (SEM) image of an 8-layer PZT actuator.

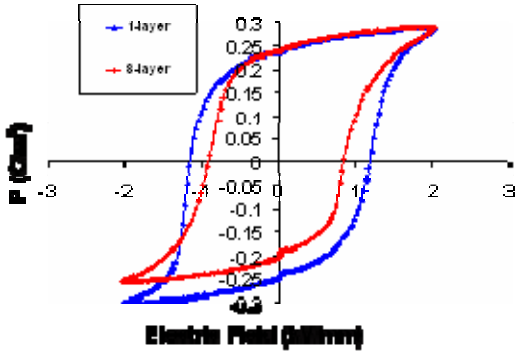

Figure 2.3. P-E hysteresis loop for a single PZT layer and an 8-layer actuator.

Figures 2.2(a) and 2.2(b) show a 10-layer and a part of an 8-layer stack actuator, respectively. Figure 2.3 shows the P-E hysteresis loops of a single PZT slab and of an 8-layer actuator with the same type of electrodes.

As shown in Figure 2.3, the multilayer PZT actuator has a hysteresis loop similar in shape to that of a single layer structure, with the former having a lower coercive field value (0.84 kV/mm) than the latter (1.17 kV/mm), which indicates better polymer electrode coverage on the sidewall of the multilayer actuator.

Finite element simulation is carried out to obtain the displacement of an 8-layer actuator as a function of applied electric field using ANSYS. The simulated displacement result for an 8-layer actuator at a driving voltage of 100V is 0.505 μm as shown in Figure 2.4. Experimental results for actuator displacement are measured using a laser displacement sensor (LK-G32, Kenyence Co.) under quasistatic conditions (0.5Hz). Figure 2.5 illustrates comparison of FEM results and experimental results of the top layer displacement of the actuator as a function of electric field for an 8-layer device. The experimental results for displacement exhibit obvious linearity and agree reasonably well with the simulation result.

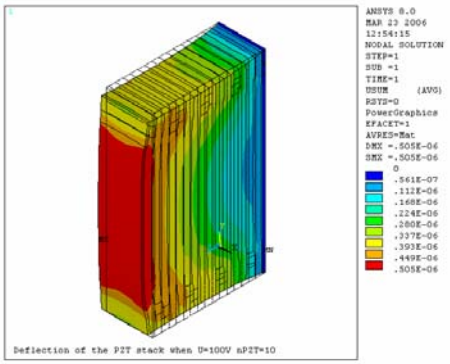

Figure 2.4. FEM simulation result for an 8-layer actuator at a driving voltage of 100V

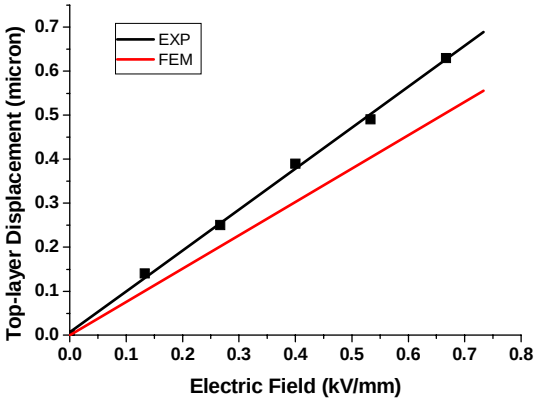

Figure 2.5. Top layer displacement of an 8-layer actuator as a function of applied electric field (maximum field of 0.66 kV/mm achieved at a voltage of 100V)

Piezoelectrically actuated microvalve with solid hydraulic amplification

Figure 2.6 illustrates the designed microvalve with three primary components: a PZT driving element and housing; a hydraulic transmission chamber filled with PDMS elastomer; and a valve chamber with outlet, inlet, and valve seat. The deformed PDMS acts both as a hydraulic amplification medium and as a valve head. The on-off switching is realized by the opening and closing of the channel gap between the valve seat and the movable valve head as shown in Figure 2.7. When a voltage difference is applied, the piezoelectric actuator expands axially and pushes the bottom layer of PDMS upwards, generating a small deflection. The upper surface of the incompressible PDMS undergoes a much larger deflection, ideally proportional to the ratio of the area at top and bottom. All three layers are fabricated primarily using SLA, but the fabrication sequence is compatible with micromolding and lamination for mass production at reduced cost. Figure 2.8 shows the fabricated microvalve.

As shown in Figure 2.9, an amplification ratio, the ratio between the PDMS valve head deflection and the piezoelectric element deflection, of 3.5 is obtained. Figure 2.10a

shows the flow rate-actuation voltage characteristics of the microvalve under three differential pressures. The maximum flow rates for nitrogen at 31.3, 60.5 and 94.4kPa are 385, 595 and 750mL/min, respectively. The closing voltages are 130, 140, and 150V, respectively. Figure 11(b) compares the maximum flow rates of the microvalve as a function of the differential pressure at four driving voltages: 0, 30, 60V. We also demonstrated the function of the microvalve as an on-off switch for a pneumatic microbubble tactile actuator as shown in Figure 12. The measured characteristics suggest its application in other liquid or gas microfluidic systems that require control of high differential pressure flow with high flow rate.

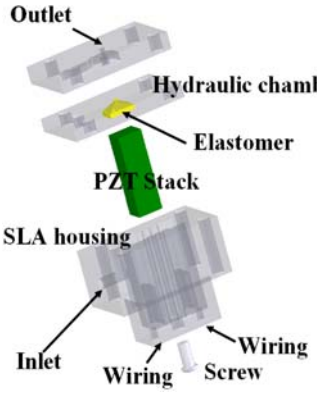

Figure 2.6. 3-D exploded schematics of the microvalve configuration, showing the geometry of the hydraulic chamber and the path of inlet and outlet

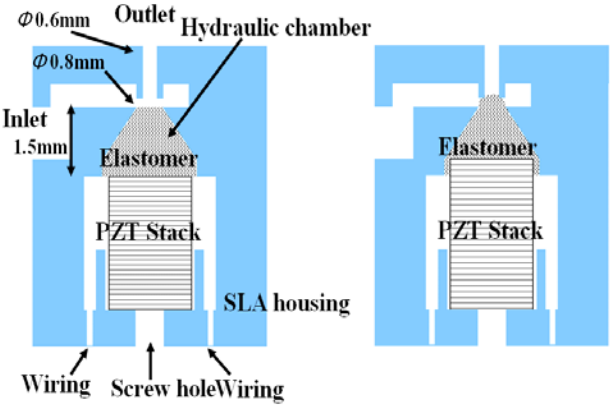

(a) valve open *(b) valve close*

Figure 2.7. Operating principle of the normally open piezoelectric polymer microvalve. Applying a voltage to the piezoelectric stack pushes the elastomer valve head against the seat rim. Thus, the channel between the seat and the head is closed.

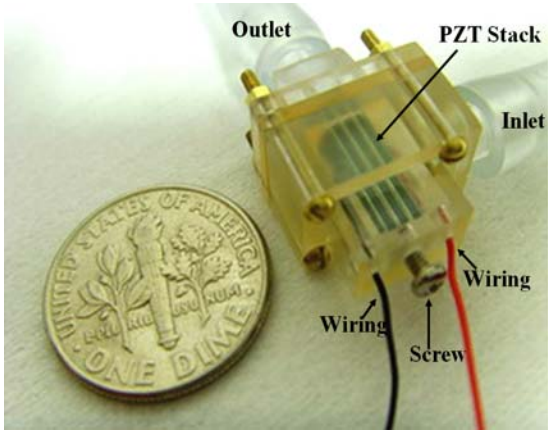

Figure 2.8. Photograph of a three-layer piezoelectrically driven hydraulically amplified polymer microvalve. Dimensions of

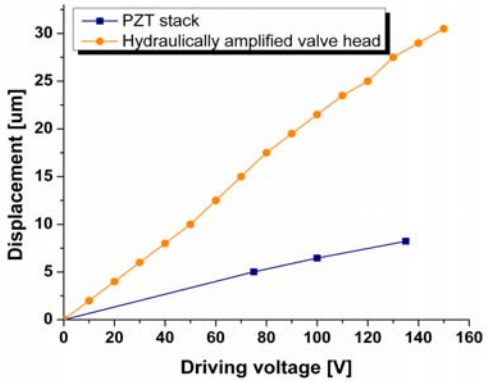

Figure 2.9. Displacement measurements of PZT driving element and hydraulically amplified valve head

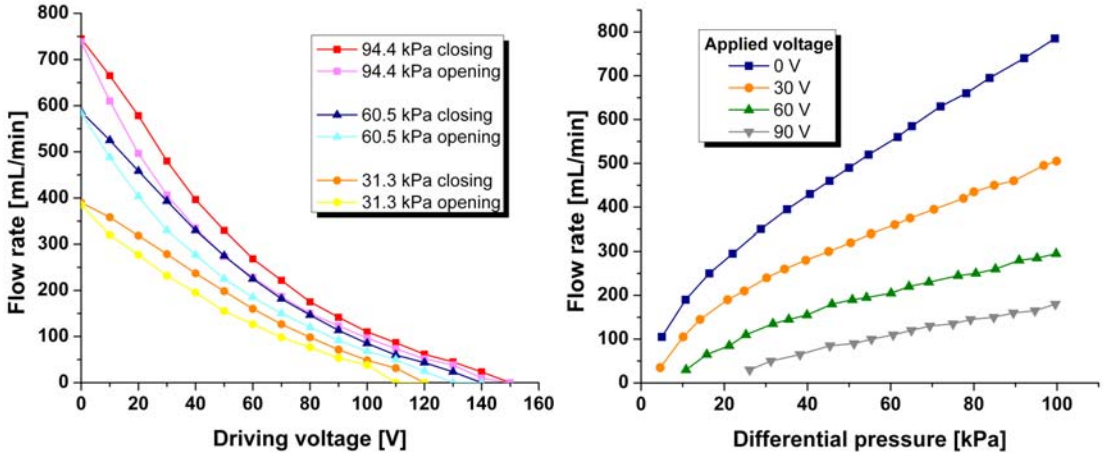

(a) *(b)*

Figure 2.10. Measured N_2 flow rate as a function of (a) actuation voltage (DC) under various differential pressure and (b) differential pressures at different actuation voltage (DC)

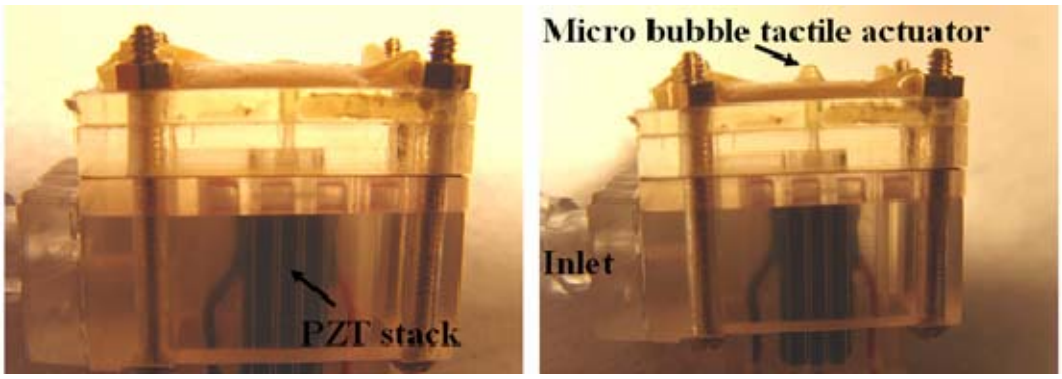

(a) Bubble actuator OFF *(b) Bubble actuator ON*

Figure 2.11: Demonstration of microvalve successfully controlling a pixel element of a tactile display. The valve is closed first by applying voltage. It successfully keeps the bubble at OFF-state when high pressure is applied to inlet (a).Then, the valve is opened and the bubble is pressurized (ON-state). Finally, the valve is closed again. The bubble remains ON-state after removal of the inlet pressure (b).

2.2 Development of micro-bubble Actuators:

2.2.1 Endoskeletal microbubble actuator

A mass-manufacturable endoskeletal micro bubble actuator capable of reversible vertical deflection has been developed. In our study, the skeletal corrugated sections of the microbubble array were achieved using a single lithographic mask by continuous rotating inclined exposure followed by sacrificial material molding and parylene coating. This approach to endoskeletal bubble actuators is not only mass-manufacturable, but can also be scaled down to even smaller dimensions if required.

SEM photomicrographs of a single corrugated SU-8 master pattern and a corresponding PEG replica pattern are shown in Figure 2.12. The molded PEG structure faithfully follows the original SU-8 microcorrugation, the inset of which shows the cross-sectional view of the combinational corrugation with a trapezoidal shape on top and a triangular shape on bottom. Figures 2.13(a) and 2.13(b) show an SU-8 microcorrugated mold array and a batch-transferred corrugated PEG mold array mounted on a stereolithographically-fabricated manifold substrate, respectively.

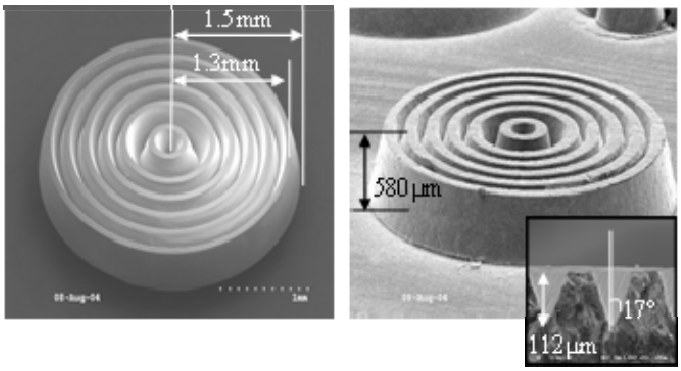

(a) *(b)*

Figure 2.12. Comparison of (a) SU-8 mold and (b) replicated PEG mold: inset shows a cross-sectional image of corrugation profile

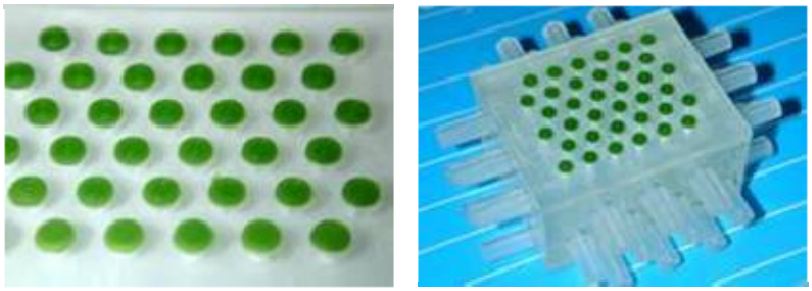

(a) *(b)*

Figure 2.13. Corrugated pattern array: (a) batch-transferred corrugated PEG array on SLA substrate, (b) final device for testing

(a) (b)

Figure 2.14. Shape comparison of (a) endoskeletal bubble and (b) pure-bubble

Figure 2.14 shows inflated and restored shapes for (a) an endoskeletal bubble actuator and (b) a pure-bubble actuator (PU skin-only). For the endoskeletal structure, the inflation of the membrane is observed to be confined to one direction, i.e. out-of plane, and the displacement is a reasonably linear function of the applied pressure. After the applied pressure is removed, the membrane almost returns to its original position and shape. The pure-bubble actuator shows similar stability and one-directional movement with small inflation while the membrane shows an omni-directional balloon-like expansion in large inflation, resulting in plastic deformation of the material. Note that when the membrane is deflated by removing the applied pressure, it becomes flaccid and does not return to its original shape.

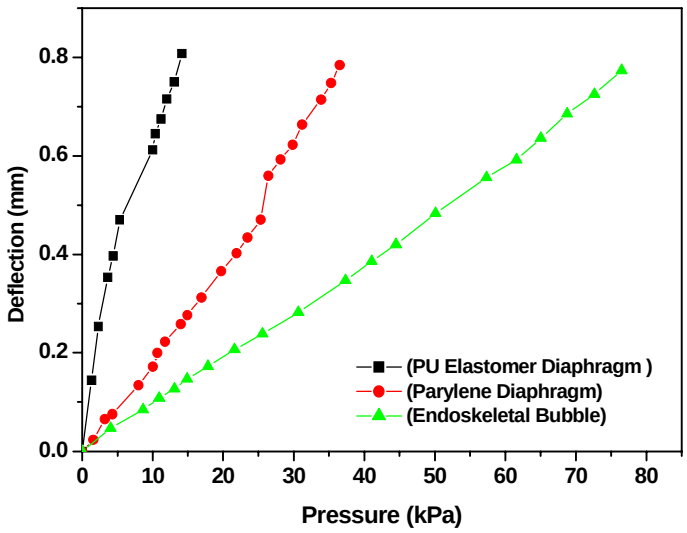

Figure 2.15. Diaphragm deflection as functions of applied pressure for three actuators: a PU elastomer diaphragm, a parylene diaphragm, and an endoskeletal bubble.

The static pressure-deflection characteristics are tested for the parylene diaphragm, PU elastomer diaphragm, and endoskeletal bubble. The thicknesses of the parylene diaphragm and PU elastomer diaphragm are 5 μm and 150 μm respectively. The endoskeletal bubble actuator has parylene and PU layers with the same thicknesses as those of the parylene diaphragm and PU elastomer diaphragm. The results are plotted in Figure 2.15. Among the three actuators compared, the PU elastomer diaphragm has an extremely low Young's modulus, and requires the smallest pressure to achieve a given deflection. The endoskeletal bubbles require the largest pressure for the same deflection, because they consist of a composite of two materials: PU and parylene, each layer of the composite having the same thickness as that of the other two diaphragms, thereby resulting in the largest effective stiffness.

The distinct "jumps" in the pressure-deflection curve for the parylene diaphragm indicate "unfolds" of one or more corrugations, which results in the large deflection. The unfolded corrugation does not always "refold" upon release of pressure because the unfolding has led to another minimum energy state. The addition of elastomer greatly enhances the linearity in the pressure-deflection relationship of the endoskeletal bubbles, while maintaining the unidirectional deflection of the actuator.

2.2.2 Application of miniaturized microbubble actuator: refreshable Braille display

A design of miniaturized microbubble actuator with 6 corrugations, an inclined angle of 17°, and a diameter of 1.5 mm has been adopted for the fabrication of RBD cell. Deeper corrugations in the center of the diaphragm enhance the vertically-oriented center deflection. The schematic view and the dimensions of the corrugated diaphragm are shown in Figure 2.16.

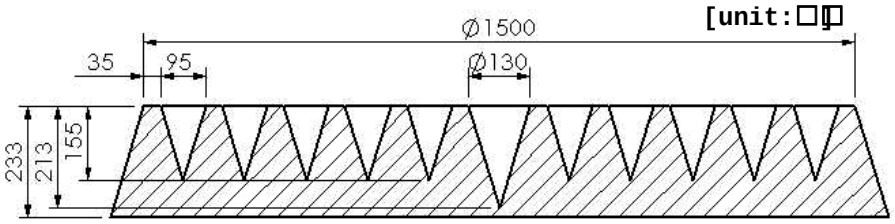

Figure 2.16. Illustration of the profile and dimension of corrugated diaphragms.

Array of sacrificial Polyethylene glycol (PEG) corrugated diaphragm molds on epoxy substrate are fabricated using inclined rotational UV lithography, micromolding, pattern transfer technology. Microscopic photomicrographs of the corrugated SU-8 molds and corresponding PEG replicates on epoxy substrate are shown in Figure 2.17.

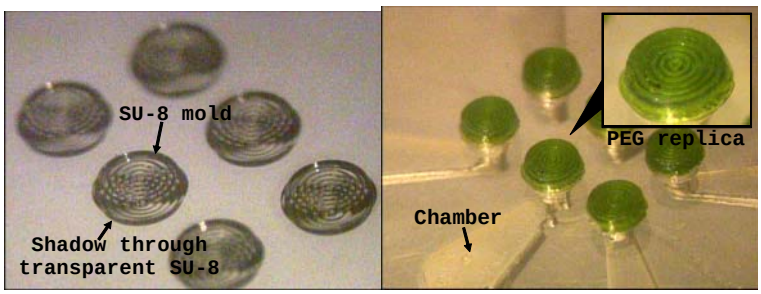

(a) original SU-8 mold *(b) PEG replica*

Figure 2.17. Fabricated SU-8 mold and PEG replica

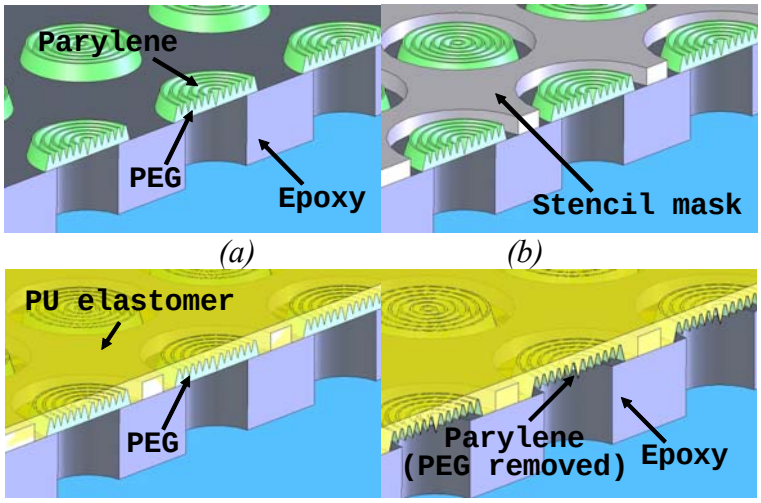

(a) *(b)*

(c) *(d)*

Figure 2.18. Fabrication process for the endoskeletal microbubble actuators

Subsequent fabrication process for the Endoskeletal microbubble actuators is shown in Figure 2.18. A parylene layer is conformally deposited on the PEG corrugation diaphragm molds array (2.18a). An epoxy stencil mask is placed on the epoxy substrate to planarize the top surface (2.18b). A thin layer of polyurethane (PU) elastomer is spin-coated on top and cured (2.18c).The sacrificial PEG is dissolved in water (2.18d). The epoxy substrate is then bonded to a manifold fabricated by SLA. Finally, 3-way solenoid

valves are assembled to the manifold to control individual actuator. The assembled device is shown in Figure 2.19.

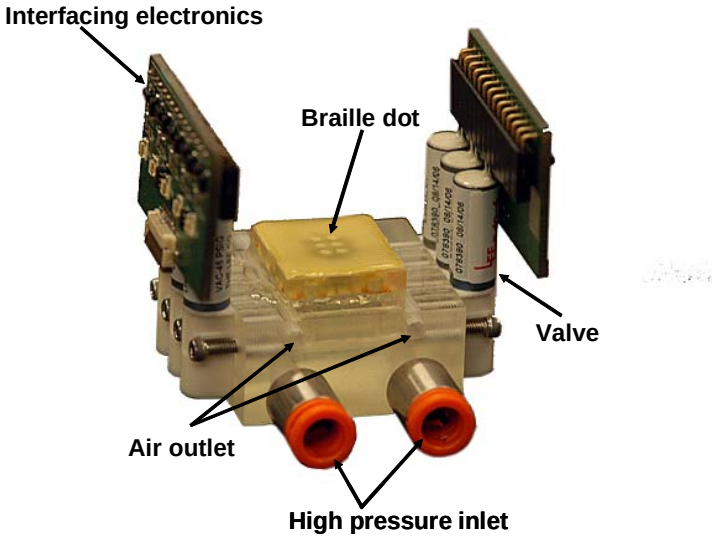

Figure 2.19. Assembled device

The performance of RBD device is assessed from the following perspectives: spatial resolution, displacement, force generated, mechanical bandwidth and pneumatic power consumption. The RBD system was designed and implemented to have a spatial resolution of 2.5mm.

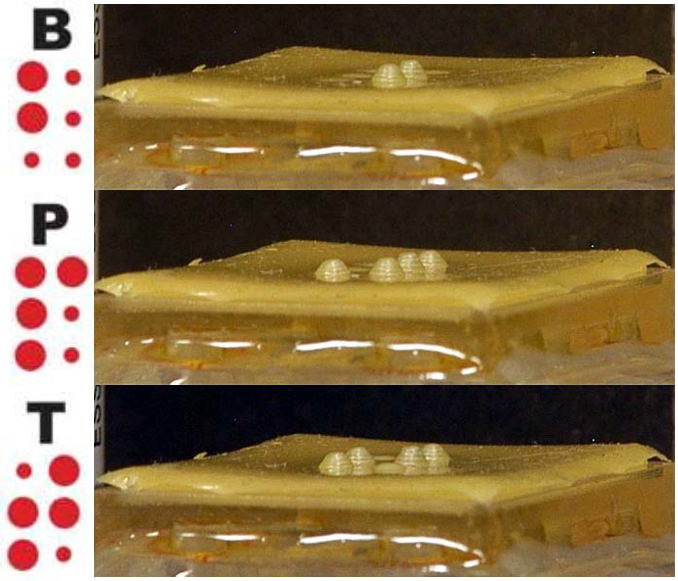

Figure 2.20. Actuation of the Braille dots corresponding to the Braille characters

Figure 2.20 shows the pictures of selective actuated Braille dots representing the characters “B”, “P” and “T” in American Braille style. The center to center distance between two adjacent dots is approximately 2.5mm.

Magnified pictures of a dot at inactivated and activated state are shown in Figure 2.21. Note that large deflections are achieved preferentially in the vertical direction, which makes the shape more distinguishable than the hemispherical shape of a pure elastomer diaphragm actuator.

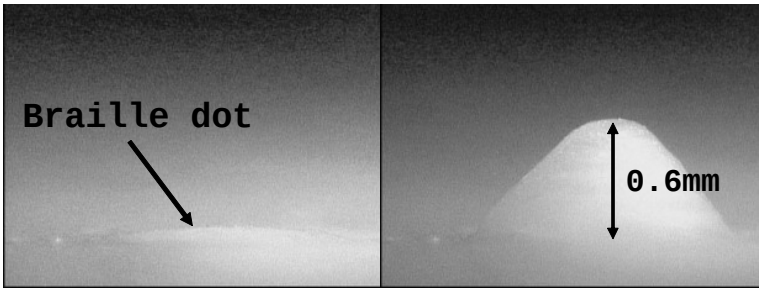

(a) unactuated dot *(b) actuated dot at 100kPa*

Figure 2.21. Inactivated and activated Braille dot

Center displacement of a Braille dot (i.e. the actuator) as a function of applied pressure has been quantitatively characterized using a laser displacement sensor. The results for a Braille dot with 2.5-μm-thick parylene and 200-μm-thick PU are plotted in Figure 2.22. It shows that the maximum displacement of the dots without load is 0.56mm. Reduction in the thickness of either parylene or PU will enable a further increase of the maximum displacement with the trade-off of reducing the generated force.

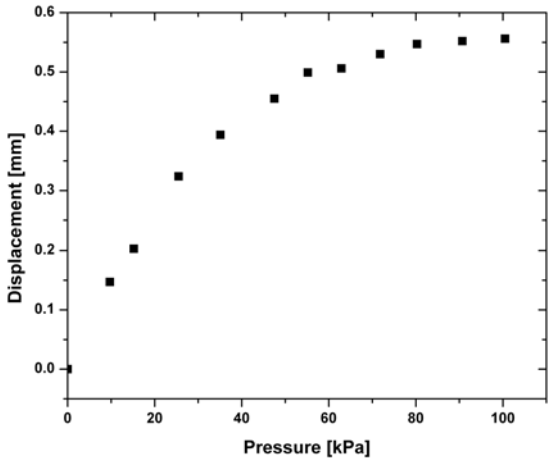

Figure 2.22. Measured dot height as function of applied pressure

Based on a survey of psychophysical experimental data which indicates that a 50-100mN force is applied during a fine-touch object exploration, each Braille dot should be designed to withstand at least 50mN contact force while maintain at least 0.25mm displacement in order to be able to stimulate the shallowest mechanoreceptor under skin. A force evaluation is carried out for the RBD device. As can be seen in Figure 2.23, a 10 g and a 20 g weight are lifted up to 0.43mm and 0.48mm by three actuated dots at 60 kPa and 100 kPa, respectively. That's correspond to 33mN and 66mN generated force per dot at 60 kPa and 100 kPa while maintain 0.4mm displacement.

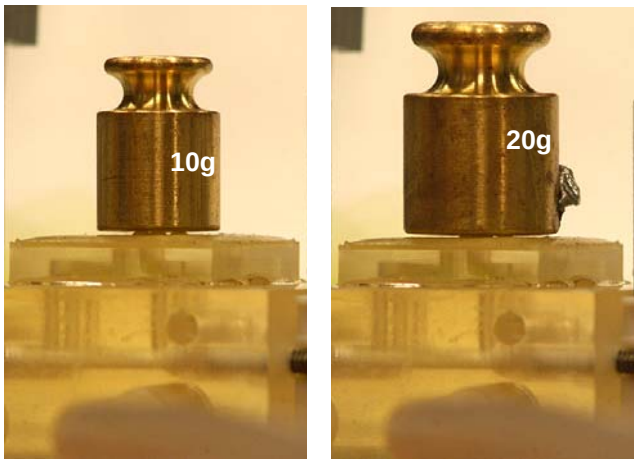

Figure 2.23. A 10g and 20g weight is lifted by three actuated Braille dots

Section 3
Creation of Formable Surfaces (Rosen)

Deformed Surface Modeling: The two mathematical models previously described have been thoroughly tested. The test consisted of a grid type design that has every nodal point on the same plane except the center node. The center node had a different z-value than the rest of the nodes. By increasing the height of this node, we can see what the affects are on the other nodes of the surface. The results of the two formulations take seconds to compute the shapes of the formable surface. The results from the mathematical models produced shapes that were to be expected. As the center node increases in height, a larger protrusion is produced in the surface. Figure 3.1a shows an example of a 9x9 surface being actuated at the center-point which produces the aforementioned protrusion in the surface. Additionally, the mathematical models do not exhibit a linear movement but exhibit a parabolic behavior. The second mathematical model was used to produce the results illustrated in Figure 3.1. A comparison between the first mathematical model and the second mathematical model shows the second

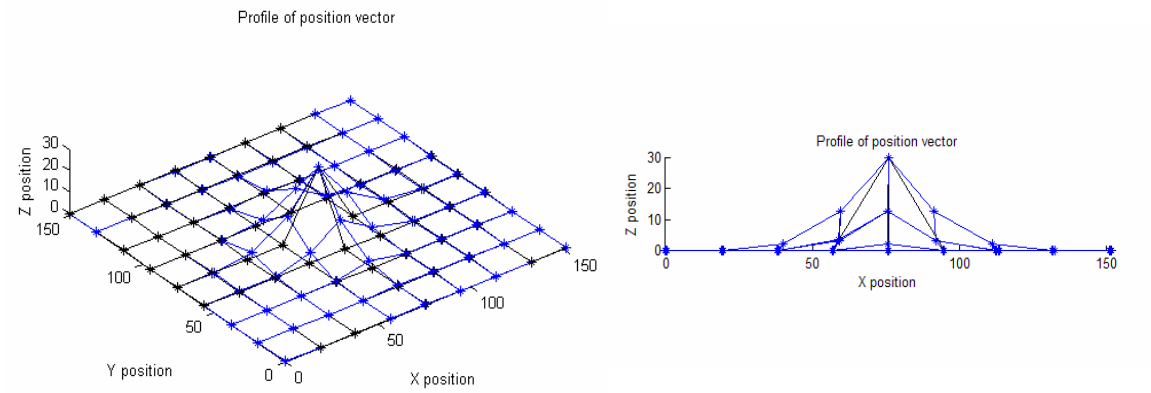

a) Illustrates bump caused by center actuation. b) Side view illustrates a parabolic affect.

Figure 3.1 – Results of a 9x9 surface being actuated at the center.

mathematical model more accurately represents the stiffness of the manufactured unit cells and the results of the surfaces are smoother than the first model.

Spring Constant Determination: The second mathematical model was used to obtain the displacement between two unit cells. The displacement that is experienced between the unit cells is concentrated on the leaf springs. An one-eighth model of the unit cell was constructed in the ANSYS workspace, shown in Figure 3.2a, and the displacement obtained from the mathematical model was implemented on the leaf spring to calculate the amount of force that was needed. This force value was then used on manufactured unit cells, and the displacements were measured enabling the value of the spring constants to be calculated. Figure 3.2b shows an ANSYS model of the deformed unit cell. Tests conducted on the manufactured unit cells show good agreement between the experimental values for the spring constants and the mathematical values for the spring constants obtained using ANSYS.

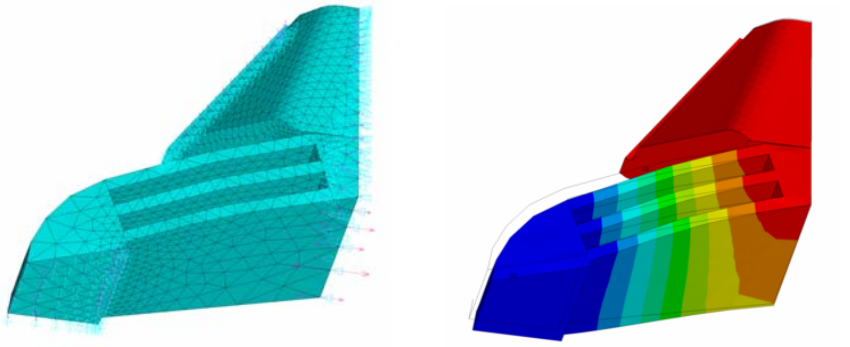

a) Model of unit cell with boundaries

b) Results showing displacement of unit cell.

Figure 3.2 – An eighth model of the unit cell in ANSYS.

Device Development: Several CAD models of the surface have been developed to enable the unit cells to attach to the bed of nails. One model involves the use of hardware to attach the surface to the bed of nails actuating device. The other models involve additional structures added to the unit cell by using a stereolithography machine. These models will be manufactured and compared for their functionality of holding the surface to the bed of nails.

Section 4
Fluidic Driven digital clay (Gleazer)

Findings

This section focuses on the characterization of the system and its individual components. An overview of the closed-loop control algorithm is presented in section II.1. The details of the system implementation of the Proportional Integral (PI) controller used in this work are presented in section II.2. Section II.3 describes the tests which are conducted to characterize the response of the PI controller and the solenoid valves. The data management techniques used for the presentation of data in this work are described in section II.4. The velocity and acceleration of the piston are computed from time traces of its trajectory and are presented in section II.5. Pressure measurements are used for diagnostics and are presented in section II.6. The pressure measurements are also used to calculate the friction forces acting on the piston, which are presented in section II.7.

4.1 Closed – Loop Controller

A closed-loop PI controller is used to control the position of the piston based on trajectory measurements obtained from the Variable Core Transformer (VCT). In a closed-loop control system, (Figure 4.1) feedback allows for the system output to be continuously compared to the desired system output.

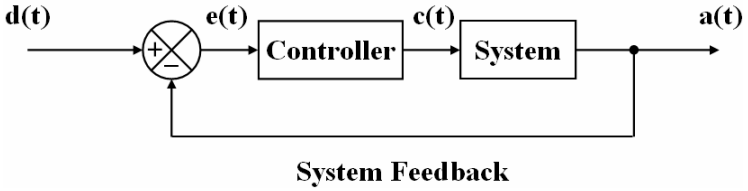

Figure 4.1: General Form of Closed-Loop Control System

The output of the controller and the desired output of the system are defined as c(t) and d(t) respectively. As seen in Figure 4.1, the controller output, c(t), is used as an input parameter to the system, and a(t) is the corresponding system output. The difference in the desired output of the system and the output of the system is represented by e(t) and is defined as the system error, as shown mathematically in Equation 1 and schematically in Figure 4.1.

$$e(t) = d(t) - a(t) \tag{1}$$

However, a controller using only the system error to control a given parameter of interests often does not provide sufficient control because a very small system error can cause a controller output which can lead to system instability. Therefore, more sophisticated control algorithms are usually employed. One such control algorithm is a specific form of closed-loop control known as Proportional Integral, or PI control. PI controllers provide greater control than a controller which uses only the system error by introducing a user specified proportional gain as well as the calculation of an integral

error and a subsequent integral gain. Figure 4.2 shows the implementation of a PI control algorithm.

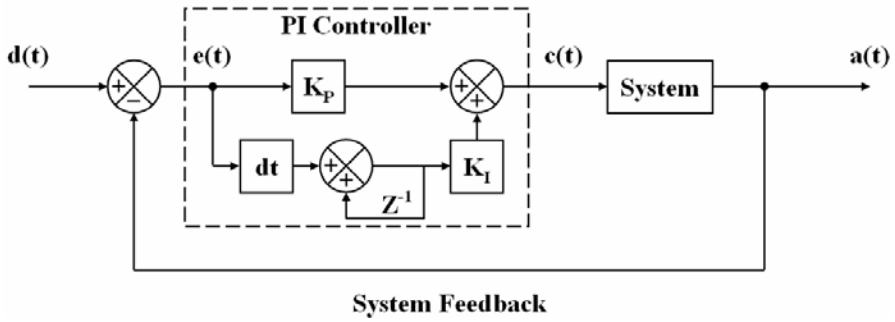

Figure 4.2: PI Closed-loop Control Algorithm

The proportional contribution of the controller algorithm is the product of the system error, e(t), and a user specified proportional gain, K_P, which affects the controller output, c(t), as defined by Equation 2.

$$c(t) = K_P * e(t) \tag{2}$$

With a proportional control algorithm, the controller output changes in proportion to the system error by a factor of K_P. The integral contribution of a PI controller is the integration of the system error with respect to time multiplied by a user specified integral gain, K_I as shown in Equation 3.

$$c(t) = K_I * \int e(t) * dt \tag{3}$$

With an integral controller, any system error eventually grows to a detectable state, which increases the accuracy by which the controller can control the output of the system. The mathematic combination of Equation 2 and Equation 3 gives the output of a PI controller as shown in Equation 4 while their schematic combination is shown in Figure 2.

$$c(t) = K_P * e(t) + K_I * \int e(t) * dt \tag{4}$$

A PI controller supplies an output which is proportional to the system error and also integrates that system error over time for increased accuracy. The value of this controller output is used to modify the physical system and is based on the user specified values of K_P and K_I as well as the continuously calculated system error. The controller output is used as an input parameter to the system being controlled.

4.2 System Implementation of Closed – Loop Controller

The PI controller controls the position of the piston using trajectory measurements of a Variable Core Transformer (VCT) by actuating two solenoid valves which are embedded in the fluidic actuator described in section I. However, certain modifications to the general description of a PI controller presented in section 4.1 are necessary.

In order to optimize the control loop rate, two computers are utilized in this work. The control-loop is implemented on a laboratory PC using LabView RT while a separate data acquisition PC using LabView is used to sample and save the position of the piston and the pressure of the working fluid in various system locations. With this setup, the data acquisition computer handles the load of saving data while the target machine's only task is to run the control loop, thereby isolating the control loop and alleviating potential internal system interruptions associated with saving data. The PI controller algorithm (Figure 4.2) is written in LabView RT and downloaded onto the target.

As show by Equation 1, the control-loop requires a desired system output as a continuous input parameter. While the controller will accept any analog function as an input parameter, a square wave, generated by a function generator (HP 33120A), is chosen in order to move the piston between two predetermined positions. Using the function generator to generate the desired values allows for precise flexible control of the controller input parameters, and therefore the desired output of the piston position.

Figure 4.3 shows the overall system implementation of the PI controller shown in Figure 4.2 and its interaction with the physical setup. Digital output values are produced by the PI controller software, which runs on the target machine, based on the output value of the PI controller and used as input values to the valves in the physical system. The actuation of V1 or V2 moves the piston down or up respectively as described in section 4.1. After the appropriate valve has been actuated the position of the piston is measured by the Variable Core Transformer (VCT) and used to calculate an updated system error value, which is used as an updated input parameter to the PI controller.

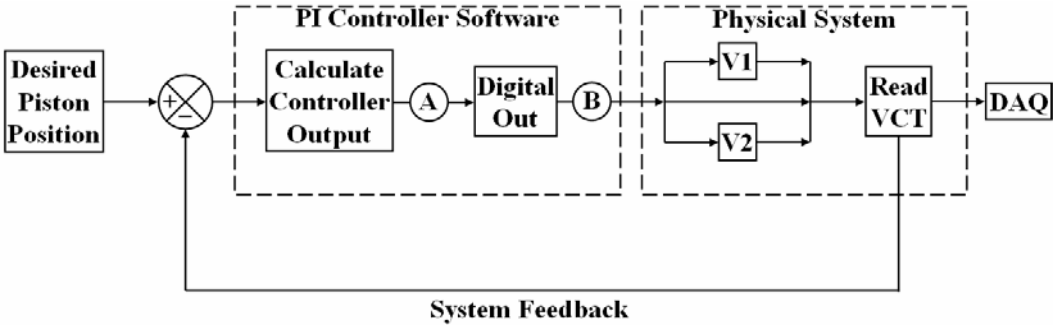

Figure 4.3: PI Controller Implementation showing PI controller software and physical system components

A proportional integral controller is used because a proportional control algorithm is only partially functional for the control of the non-proportional solenoid valves used in this work. This is because the only valve configurations are fully open and fully closed. Therefore, as the system error decreases, the controller output decreases to the point that only a slight change in the system output is needed to match the desired output, which is not attainable by fully opening, or closing, the valve. As a result, the valve is fully opened and closed rapidly to try to achieve the desired system output, which creates unwanted oscillations. A possible solution is to specify an error bound on the system output, within which the controller does not output anything, allowing the system to maintain its current state. This error bound is necessarily introduced at location A in Figure 4.3, after the controller operations and before the digital output operation. While

the addition of an error bound alleviates problems of system instabilities, it decreases the accuracy with which the controller can control the system output by introducing the possibility of a steady state bias error. One of the solutions to this issue is to incorporate integral control in addition to proportional control, yielding a PI controller output as governed by Equation 4. As seen in Figure 4.3, there are three distinct possible output values from the PI controller software, which are detailed in Table 4.1. The controller output voltages are sent to solid state relays which actuate the valves in order to move the piston as indicated by the last column of Table 4.1

Table 4.1: *Controller Output Configuration*

Controller Output Configuration	Controller Output Voltage		Physical System Meaning
	Channel 1 (V1)	Channel 2 (V2)	
1	5	0	Move Piston Down
2	0	0	No Piston Motion
3	0	5	Move Piston Up

When the position of the piston, as measured by the VCT, is above the user specified desired piston position, the output of the controller is described by configuration 1 shown in Table 4.1. Similarly, when the measured position of the piston is below the desired piston position configuration 3 is utilized. If the piston position is within the user specified error bound described above then configuration 2 is used and the piston maintains its current position. An error bound of 1 mm is chosen for this work because it is greater than the system error (section 4.3) and is attainable with noise in the system.

As described by Equation 3, any system error will cause the integral error to grow. Therefore, if the desired piston position is in the form of a square wave, which causes an instantaneous system error, then while the appropriate solenoid valve is fully opened to reduce the system error the integral error will also begin to grow. The fact that the integral error begins to grow the moment a system error is detected is not an issue. However, complications arise in the fact that the valve is already fully opened and any additional growth of the integral error will not achieve the desired result of further opening the valve. Therefore, if the integral error is allowed to grow at the onset of a system error then when the piston reaches the desired position the integral error will still be non-zero. This non-zero integral error will produce a non-zero PI control software output, which will move the piston past the desired piston position and unnecessarily decrease the accuracy of the controlled piston position. For this reason a user specified bound is added to the integral error which only allows the integral error to grow while the system output is close to the system error bound. Therefore, a proportional controller is effectively used to move the piston close to the desired piston position and an integral controller is effectively used to alleviate any steady state bias error in the controlled piston position.

Controlling only position and using on-off solenoid valves makes it impossible to control the velocity or acceleration of the piston because the valve is either fully open or fully closed. Therefore, if an arbitrary curve is used as the desired piston position, then the PI controller software will move the piston either up or down to reduce the error. However,

as shown in Figure 4.4, if the desired position is a curve then the resulting motion of the piston can not match it because the only options that the controller has are to fully open or fully close the valves, which gives the position response shown in Figure 4.4. It is noteworthy that the "steps" in position are attributable to the fact that the position is controlled by on-off valve actuation. The response time of the valves is on the order of 1-2 ms, and the steps shown in Figure 4.4 are on the order of 30 ms.

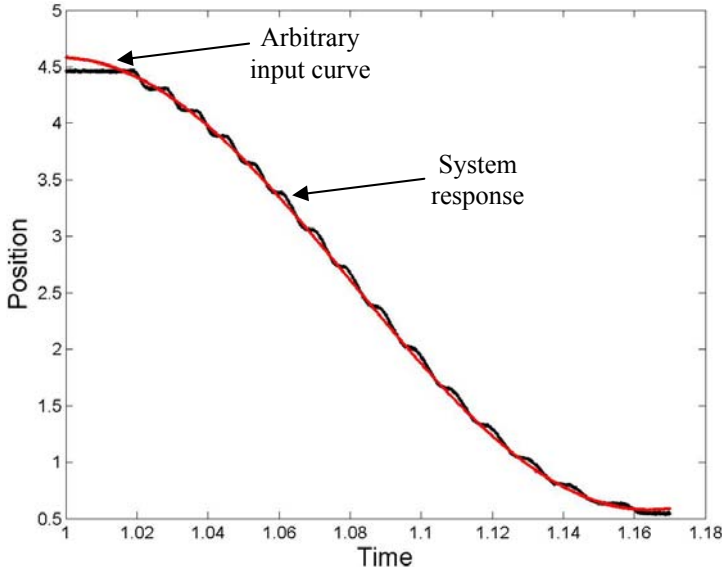

Figure 4.4: System response to arbitrary input curve

4.3 Control-Loop Characterization

This section describes the tests that are conducted in order to determine the performance of the PI controller described in section II.2. Sampling the digital output of the controller at a rate of 140 KHz for 14,000 cycles of the control-loop gives an average control-loop rate of 687 μs with a standard deviation of 8 μs, as shown in Figure 4.5. The data shown in Figure 4.5 represents both upward and downward actuation of the piston and is approximately normally distributed about 687 μs; confirming that the control-loop response time is independent of the direction of the actuation of the piston.

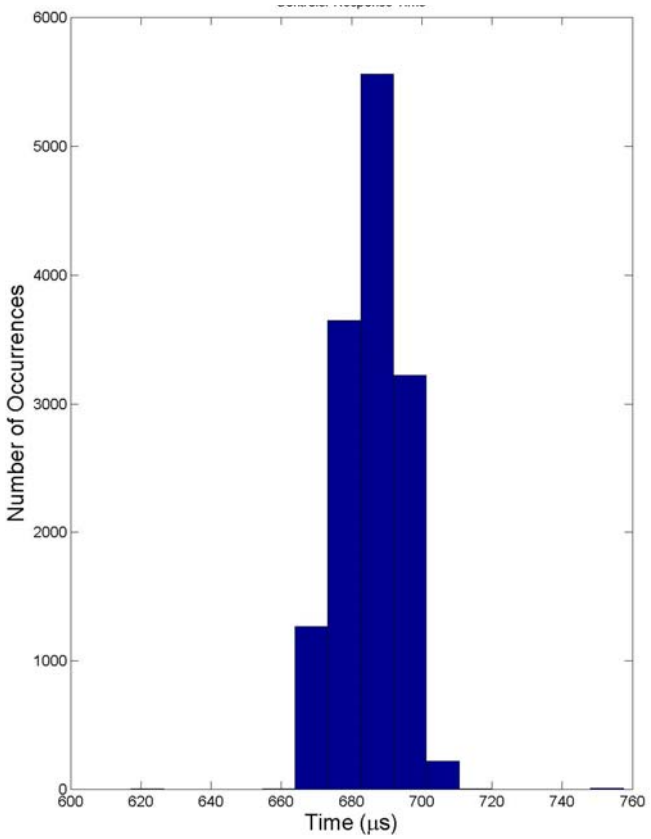

Figure 4.5: Histogram of Controller Response Time

As described in section 4.2, the controller has analog input values (function generator) for the desired system output and the piston position (VCT) as well as two digital outputs which correspond to the actuation voltages for the valves as described by Table 4.1. The channels on the data acquisition board need to be initialized before any signals can be passed through the board. This initialization takes place when the control-loop program is started, but before the controller actually starts as illustrated by Figure 4.6.

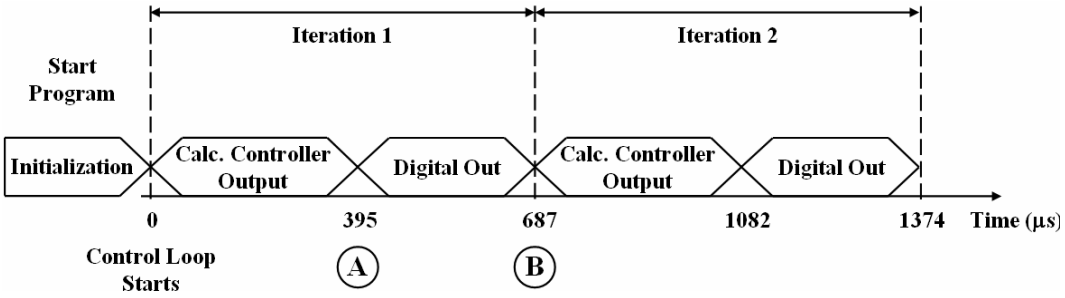

Figure 4.6: Controller Timing Diagram

The portions of the controller timing diagram labeled as A and B in Figure 6 correspond to the same labeled positions in PI controller implementation diagram shown in Figure 4.3. Therefore, the controller takes an average of 395 μs to sample the appropriate analog channels and compute the controller output. The creation and output of the TTL

signals needed to actuate the valves consumes an additional 292 μs to bring the control-loop rate to approximately 1455 Hz.

As mentioned in section 4.2, the valves are actuated by TTL signals through solid state relays. Figure 4.7 shows the response time of one of the valves obtained by recording the voltage across a shunt resistor in series with the output of the solid state relay (sampled at 10 KHz for 500 cycles of the piston). Figure 4.7 also shows the pressure response. When the voltage is first applied to the solenoid valve the solenoid has to induce high enough voltage into the coil of the valve to switch it mechanically. When the valve switches, the current through the coil changes and produces a local minimum in voltage (for $0.6<t<2.8$). The pressure difference across the valve begins to change when the valve is opened.

V1 has an average rise time of 1.68 ms and a standard deviation of 0.17 ms and V2 has an average response time of 1.28 ms with a standard deviation of 0.40 ms, which are within the manufacturer's specified 1-2 ms response time. The system is driven with 15 psi in the pressure reservoir. For this reason, the pressure difference across the valve at the time of excitation is 15 psi. As seen in Figure 4.7, the pressure difference across the valve does not change until approximately 1.7 ms, further confirming the response time of the valve.

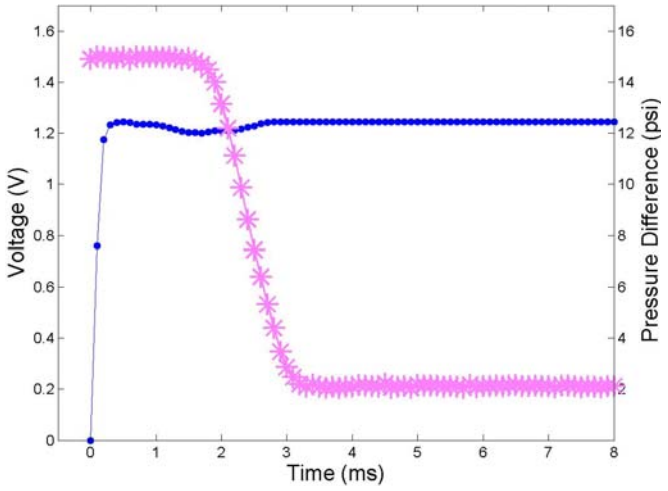

Figure 4.7: Average Voltage (•) and Pressure Response (*) for V1 (500 Cycles) with a driving pressure of 15 psi

4.4 Data Management

Due to the cyclic nature of the piston's motion, it is desirable to present phase averaged position and pressure data. The stroke is the maximum displacement of the piston (either bottom to top or top to bottom) within the cylinder while a cycle is defined as an upward stroke followed by a downward stroke. Unless otherwise specified, all of the present data are measured during 20 consecutive cycles of piston motion. All position and pressure data is phase locked to the desired system output and phase averaged. The upward and downward piston motion are separated to provide the ability to analyze each directional data set individually.

With a signal to noise ratio of the position, measured by the variable core transformer, of approximately 161, the averaged cyclic position data is further reduced by passing a window over it and averaging the data inside the window. The resulting single data point from each window is reassigned to the time which corresponds to the middle time step of each window.

4.5 Velocity and Acceleration of Piston

Piston position data is recorded at 1 KHz for 20 100 mHz cycles of the piston and reduced using the method described in section 4.3. The piston position data y(i) is numerically differentiated using central differencing to obtain velocity and acceleration approximations of the piston such that

$$v_P(i) \approx \frac{y_{i+1} - y_{i-1}}{2\Delta t} - O(\Delta t^2) \tag{5}$$

and

$$a_P(i) \approx \frac{y_{i-1} - 2y_i + y_{i+1}}{\Delta t^2} - O(\Delta t^2) \tag{6}$$

(Press 1992) where Δt represents the time difference between two adjacent data points and y(i) represents the position of the piston. The errors of the velocity and acceleration approximations are on the order of Δt^2. With a time difference (Δt) of 1 ms, the errors in the velocity and acceleration are both significantly less than 0.01% of the calculated values.

Figure 4.8a and b show the piston trajectories for 20 cycles of upward and downward piston motion respectively as a function of time for multiple driving pressures. Since each line type in Figure 4.8 represents 20 cycles, the minimal dispersion as shows the stability of the velocity of the piston. The time required for the piston to move through its range of motion increases as the pressure is decreased (5 seconds for 6 psi vs 0.8 seconds for 25 psi). Note that at 6 psi (the system's lowest operating pressure) the piston's motion does not reach the end point within the shown time.

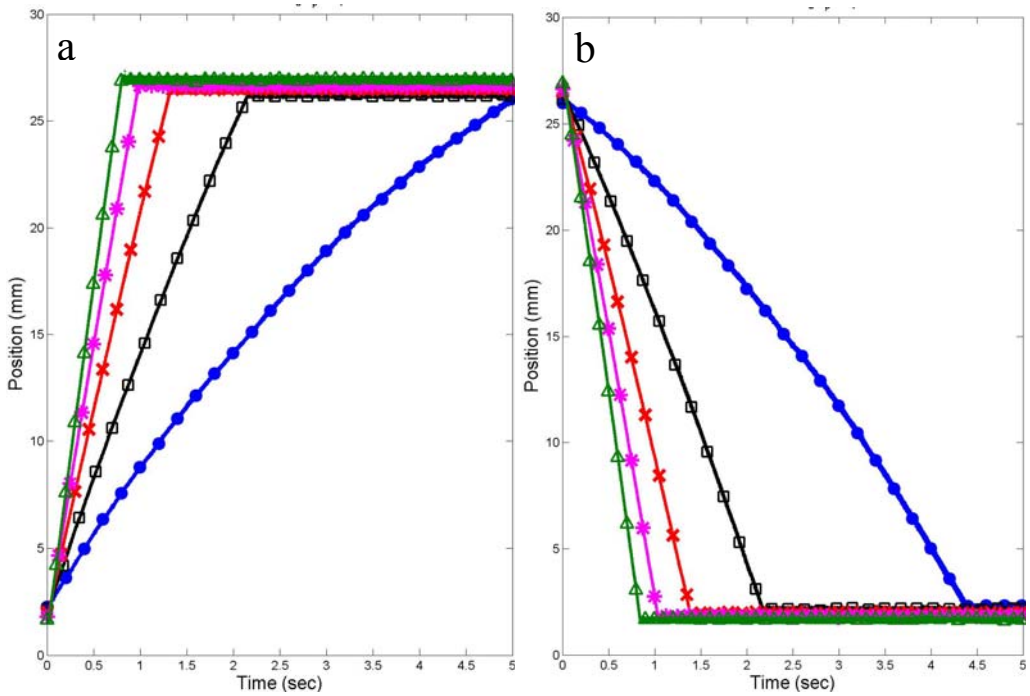

Figure 4.8: *Piston position for upward (a) and downward (b) motion of the piston respectively for driving pressures of 6 (•) 10 (□) 15 (×) 20 (*) and 25 (Δ) psi*

Figure 4.9 shows samples of the velocity and acceleration approximations of the upward and downward motion of the piston as a function of position for multiple driving pressures.

Figure 4.9a and c represent the upward motion (2-28 mm) of the piston while Figure 9b and d represent the downward motion (28-2 mm) of the piston. Therefore, the velocity of the piston is globally increasing as it moves down and globally decreasing as it moves up.

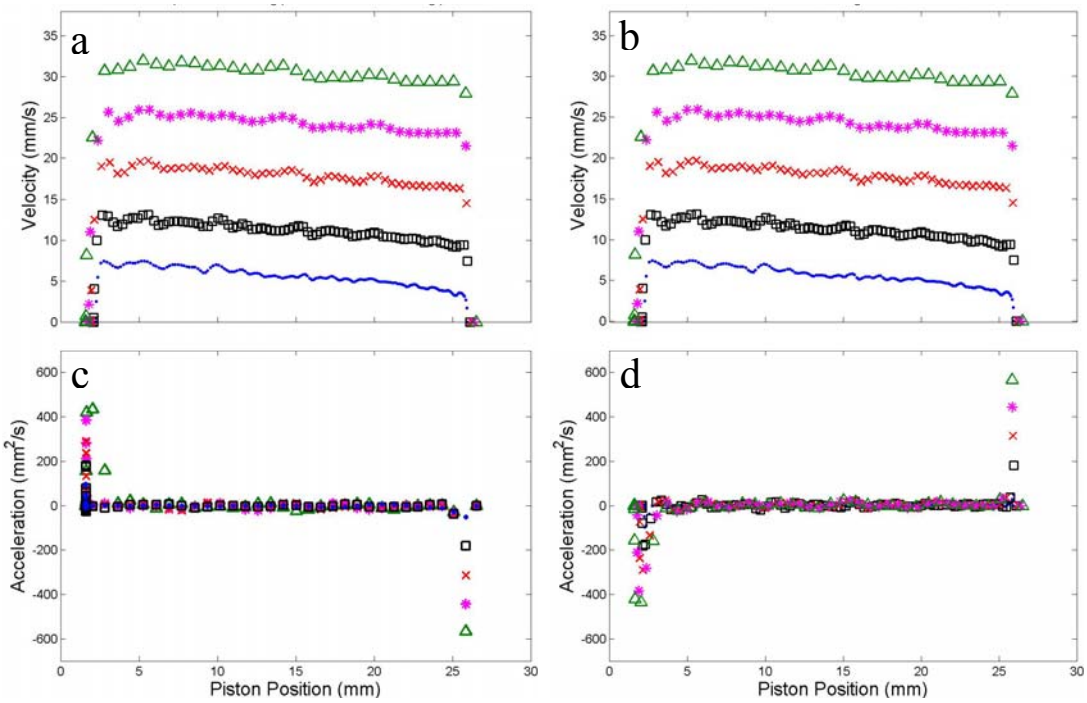

Figure 4.9: *Piston velocity and acceleration for upward (a,c) and downward (b,d) motion of the piston respectively for driving pressures of 6 (•) 10 (□) 15 (×) 20 (*) and 25 (Δ) psi*

A comparison of Figure 49a and b shows that the downward velocity of the piston is generally greater than the upward velocity of the piston. This is because the viscous losses associated with the channels employed for the downward motion of the piston are less than those associated with the upward motion of the piston due to the internal geometry of the fluidic actuator. Comparison of Figure 4.9c and d shows that the acceleration of the piston as it moves up and down are approximately zero while the piston is in motion when compared to the respective accelerations at the commencement and termination of the piston's motion. The piston accelerations are higher for both the upward and downward motion of the piston when the piston is beginning its motion than they are when the piston is ending its motion. This is because there is a larger pressure spike when the valves are opened than there is when the valves are closed.

The velocities shown in Figure 4.9a and b are averaged over the time that the piston is in motion and plotted in Figure 4.10. As seen in Figure 4.10, the velocity of the piston varies linearly with the variation of the driving pressure for both the upward and downward motion of the piston.

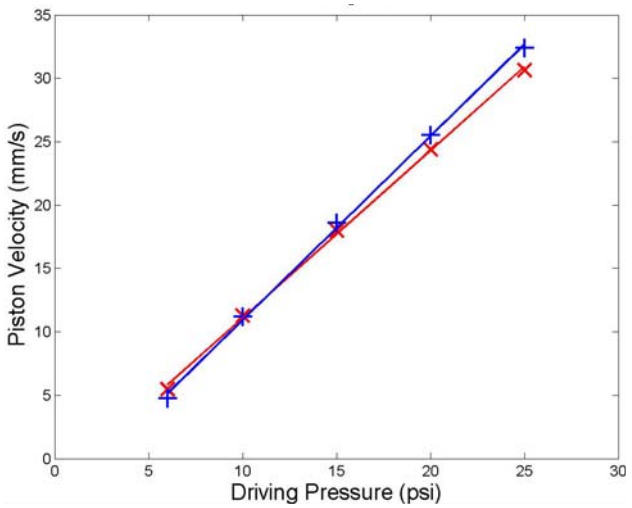

Figure 4.10: Average p*iston velocities as a function of driving pressures upward (×) and downward (+) motion of the piston*

As noted above, the piston accelerates as is moves down and decelerates as is moves up. The reason is a misalignment of the piston with the piston rod, which is described in more detail in section 4.7. The range of piston motion shown in Figure 9 does not represent the entire range of motion of the piston. The piston is commanded to move through the middle 25 mm of its 30 mm range of motion to prevent a potential collision of the piston with the top or bottom of the cylinder cavity.

4.6 Pressure Measurements

Figure 4.11 shows the fluid channels that are utilized for piston actuation. When the piston is commanded to move, fluid moves from the pressure reservoir to the fluidic actuator, through valve V1 or valve V2, through the cylinder cavity and into the return tank. As described in the Activities section 4.2.2, the fluidic actuator is instrumented with six pressure ports. Two transducers, T1 and T2, are used to monitor the pressure in ports 1-6 (Figure 4.11) while T3 is connected to port 7.

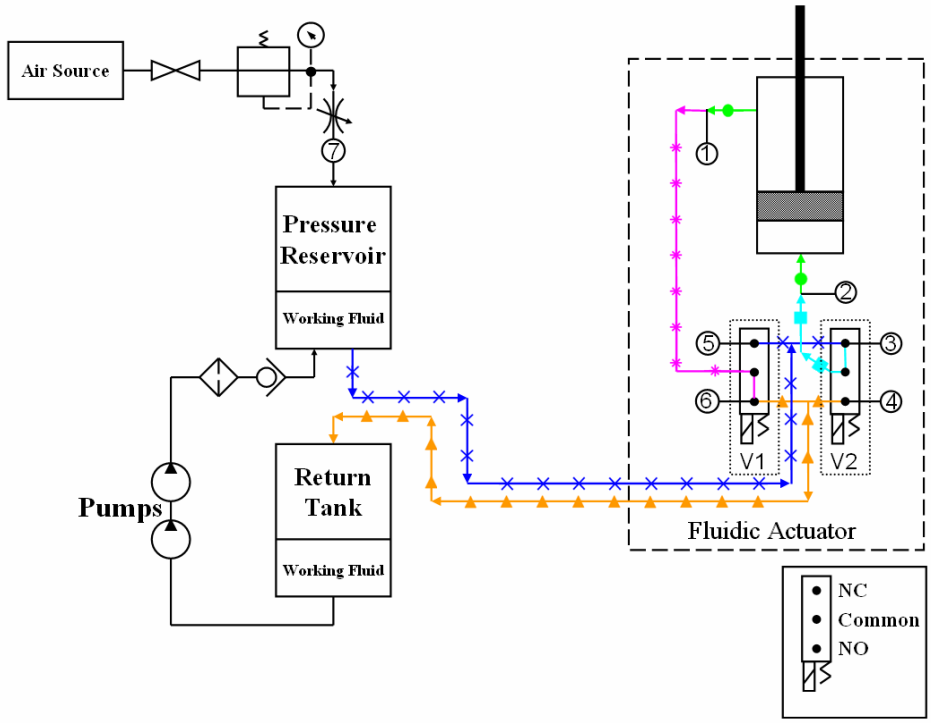

Figure 4.11: Fluidic system schematic showing fluid paths from pressure reservoir to fluidic actuator ( ), across V1 ( ), across V2( ),across the piston ( ), and into the return tank ( )

The pressure difference across the piston is of particular interest because it corresponds to the force that the piston produces at a given operating pressure. Figure 4.12 shows the pressure differences across the system components shown in Figure 4.11 at a driving pressure of 15 psi. The pressure differences across valves V1 and V2 for the upward and downward motion of the piston at 0 mm and 22 mm are 15 psi because the system was driven with 15 psi for these measurements. Therefore, the pressure difference across the valve when the valve is closed is equal to the driving pressure of 15 psi. Comparison of Figure 4.12a and Figure 4.12b shows that the pressure difference across the piston generally decreases in magnitude as a function of position for the downward moving piston and generally increases in magnitude as a function of position for the upward moving piston.

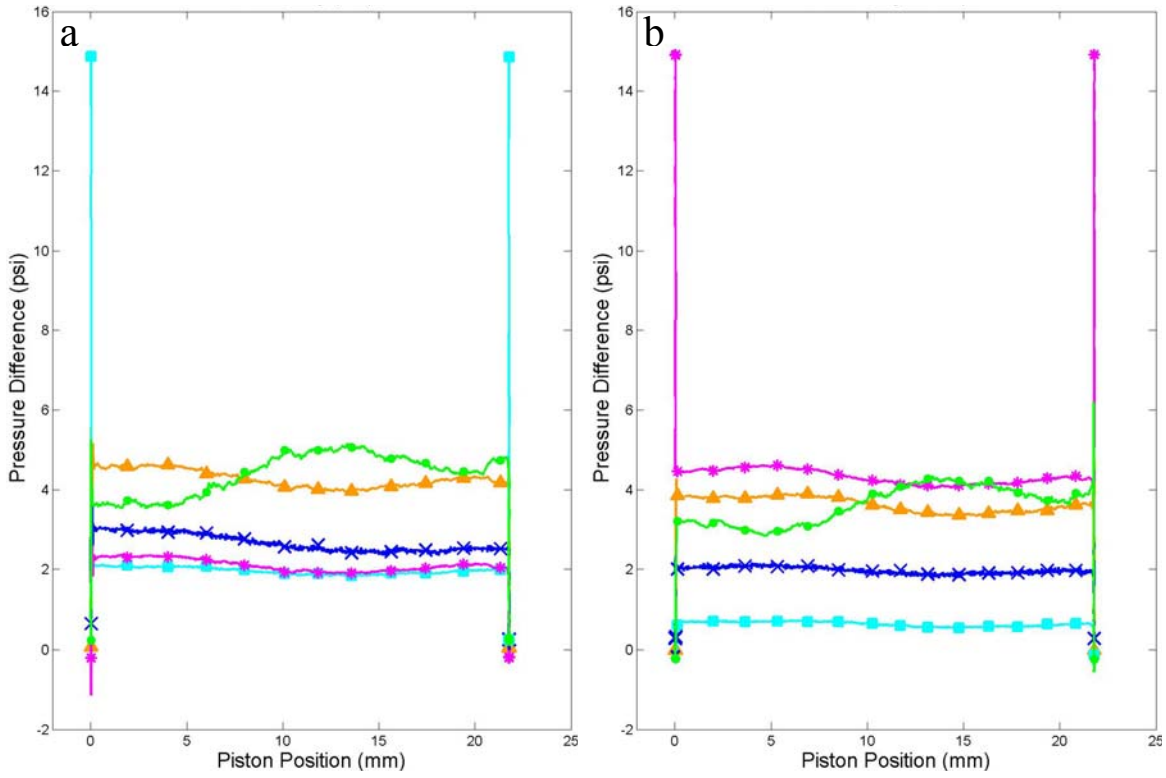

Figure 4.12: System pressure difference for upward (a) and downward (b) motions of the piston (symbols as in Figure 4.11)

However, all of the other system pressure differences shown in Figure 4.12 exhibit the opposite trend; decreasing in magnitude as a function of position for the upward moving piston and increasing in magnitude as a function of position for the upward moving piston. Comparison of Figure 4.12a and Figure 4.12b shows that the pressure variations for the upward and downward motion of the piston are nearly identical. The large range of motion over which the major variation in the pressure difference across the piston occurs (5-20 mm) indicates that the fluctuations in pressure are not location specific and are, therefore, not attributable to localized surface irregularities on the shaft, cylinder, or top seal.

The reason that these pressure difference profiles generally increase as a function of piston position is because the piston head is actually mounted off center. This misalignment is present because when the piston rod was glued to the piston, the piston rod was centered on the piston head by inserting the piston rod to a location approximately 5 mm from the bottom of the cylinder and leaving it there until the glue dried. Since the glue was allowed to dry at this location there is no side loading on the piston due to misalignment when the piston position is approximately 5 mm. For this reason, the pressure differences across the piston for the upward and downward motion of the piston have minimums at approximately 5 mm (Figure 4.12). Figure 4.13 shows a schematic of the piston inserted into the cylinder at depth d. The side loading on the piston increases as the piston moves up because distance d is the length of the shaft that is flexed as the piston moves. As the piston moves up, distance d decreases, which increase the rigidity of the shaft, and therefore, the force needed to flex the shaft.

The increasing side loading on the piston slows the ascent of the piston and therefore increases the pressure difference across the piston head. This also decreases the pressure differences across all of the other fluid channels because the pressure difference across all of the channels is proportional to fluid velocity, and the fluid velocity is decreasing due to the decreasing velocity of the piston.

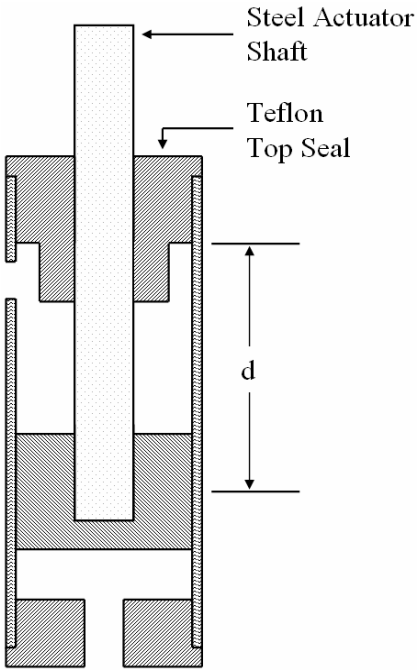

Figure 4.13: Schematic of piston showing steel actuator shaft, Teflon top seal, and piston depth d.

This is visible in Figure 4.12a by the increase in pressure difference across the piston from approximately 5 to 13 mm and in Figure 4.12b by the decrease in the pressure difference across the piston over the same range of motion. The downward motion of the piston has the opposite behavior as the upward moving piston because as the piston moves down the side loading is decreased and the piston accelerates downward, decreasing the pressure difference across the piston head and increasing the pressure differences across the other fluid channels.

Because the upper and lower cylinder cavities are connected to the common ports of the valves (Figure 4.11) and the normally closed ports of both valves are connected to the pressurized fluid, only one valve needs to be activated to actuate the piston (V1 and V2 for motion upward and downward respectively). The pressure differences across V1 and V2 change simultaneously for the upward and downward motion of the piston. The characteristic response times are somewhat different (e.g. 1.68 ms vs 1.28 ms for up/down motions respectively).

4.7 System Friction Forces

This section describes the test stand that was developed to characterize the friction forces acting on the piston. The contributions to friction are the friction force due to the Teflon top seal (f_{teflon}), the inertia of the fluid in the upper cylinder cavity ($f_{inertia}$), and the reactionary force acting on the side of the piston head due to the misalignment of the actuator shaft (f_{side}). Figure 4.14a shows the free body diagram of the upward moving piston while Figure 4.14b shows the labeled system components. The accompanying force balance equations are shown in Equation 7. As seen by Equation 7, the friction force due to the side loading on the piston (f_{side}) is obtained by using the forces due to the driving fluid in the upper, $(pA)_u$, and lower, $(pA)_l$, cavities, the force due to the weight and acceleration of the piston and shaft and the friction force exerted by the Teflon top seal (f_{teflon}).

$$\begin{aligned} \sum F_y : (pA)_l - (pA)_u - Mg - f_{teflon} - f_{side} &= F_{available} \\ (pA)_l - f_{inertia} - Mg - f_{teflon} - f_{side} &= Ma_{piston} \\ (pA)_l - f_{inertia} - M(g + a_{piston}) - f_{teflon} &= f_{side} \end{aligned} \tag{7}$$

As shown in Equation 7, the force due to the driving fluid in the upper cavity has been labeled as $f_{inertia}$. This is done because when the piston is moving up, the lower cavity is pressurized and the upper cavity is connected to the return tank through the pathways shown in Figure 4.11. Therefore, the pressure measured in the upper cavity for the case where the piston is moving up is due to the inertia of the fluid along with the friction due to the respective channels. However, the friction force due to the Teflon top seal is unknown. For this reason, an isolated experiment is described whereby the friction force due to the Teflon top seal is obtained.

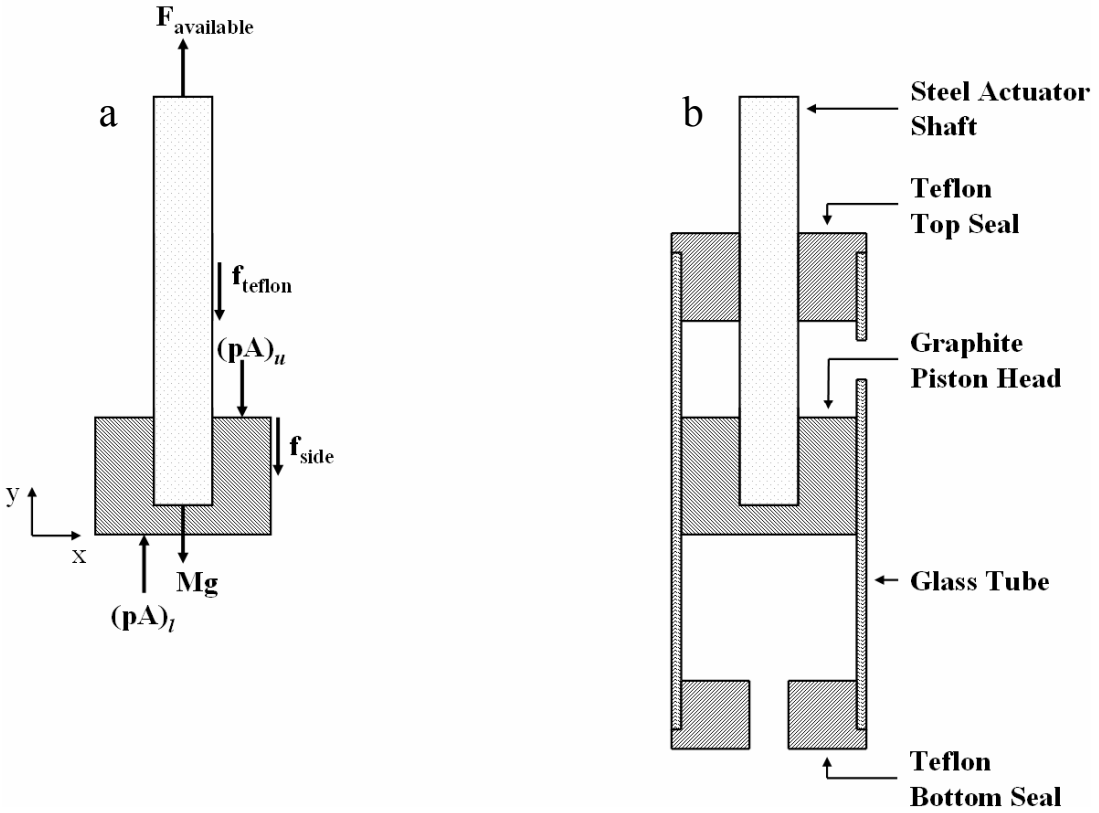

Figure 4.14: Free body diagram for upward motion of the piston (a) and labeled system components (b)

The friction force test stand (Figure 4.15) was used to isolate the friction force due to the Teflon top seal from the other friction forces in the system. Figure 4.15 shows the basic structure of the friction force test stand, the forces acting on the piston rod, and the force balance equation during the upward and downward motions of the piston. In this stand, the actuator shaft is pulled through the Teflon top seal by a given weight (40 g). The piston position is measured at 100 KHz by the Optical Displacement Measurement System for 20 strokes of the piston. The friction force between the Teflon top seal and the steel actuator shaft is obtained by calculating the acceleration of the piston. As shown in Figure 4.15, the friction force test stand does not include the side loading on the piston head within the glass tube.

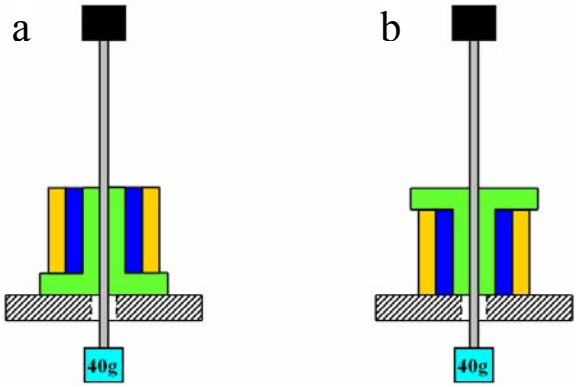

Figure 4.15: Friction Force Test Stand for Simulated Upward and Downward Motion of the Piston (Solenoid Not Shown)

The orientation of the Teflon top seal is changed for upward and downward motions (Figure 4.15). The calculated acceleration of the piston is used in Equation 8 to obtain the friction acting on the shaft due to the Teflon top seal.

$$\sum F_y : f_{teflon} - Mg = Ma_{piston}$$
$$f_{teflon} = M(g + a_{piston}) \tag{8}$$

Figure 4.16 shows the calculated velocity and acceleration for upward and downward piston motion respectively.

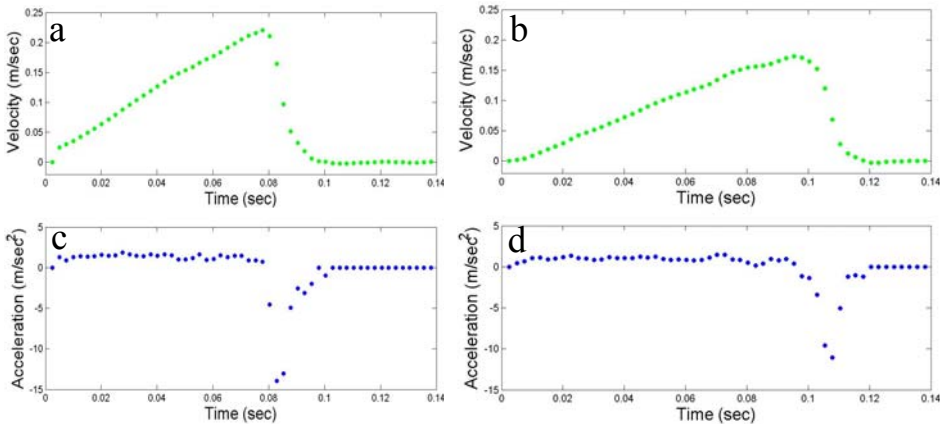

Figure 4.16: Velocity and Acceleration for upward (a,c) and downward (b,d) piston motions respectively as obtained from the friction force test stand

Inspection of Figure 4.16 shows that the velocity and accelerations calculated from the friction force test stand are time invariant during the motion of the piston, which means that the corresponding friction forces that are calculated from the accelerations can be used as constants in Equation 7. Comparison of Figure 4.16a and c with Figure 4.16b and d shows that the piston accelerates faster as it moves up than it does as it moves down because the same distance is traveled in less time. The average acceleration for the upward and downward moving piston are 1.42 m/s^2 and 1.05 m/s^2 respectively, which yields average friction approximations (f_{teflon}) of 0.504 N and 0.522 N respectively. The difference in the friction force is present because the Teflon top seal actually has small

helical ridges on the inside of the center hole from the machining process. These small ridges produce a greater friction force when the actuator shaft is moving down than when the piston is moving up, which partially accounts for the decreased acceleration of the downward moving piston as compared to the upward moving piston.

With the isolated measurement of the friction force due to the Teflon top seal (f_{teflon}), it is now possible to solve Equation 7 for the friction force which is attributable to the side loading on the piston head (f_{side}). Figure 4.17a and b show the resultant friction force acting on the piston and actuator shaft as well as the friction force due to the side loading on the piston head (f_{side}), the friction force due to the Teflon top seal (f_{teflon}), and the friction due to the inertia of the fluid ($f_{inertia}$) for the upward and downward motions of the piston respectively. The friction force due to the side loading on the piston head (f_{side}) was obtained by solving Equation 7.

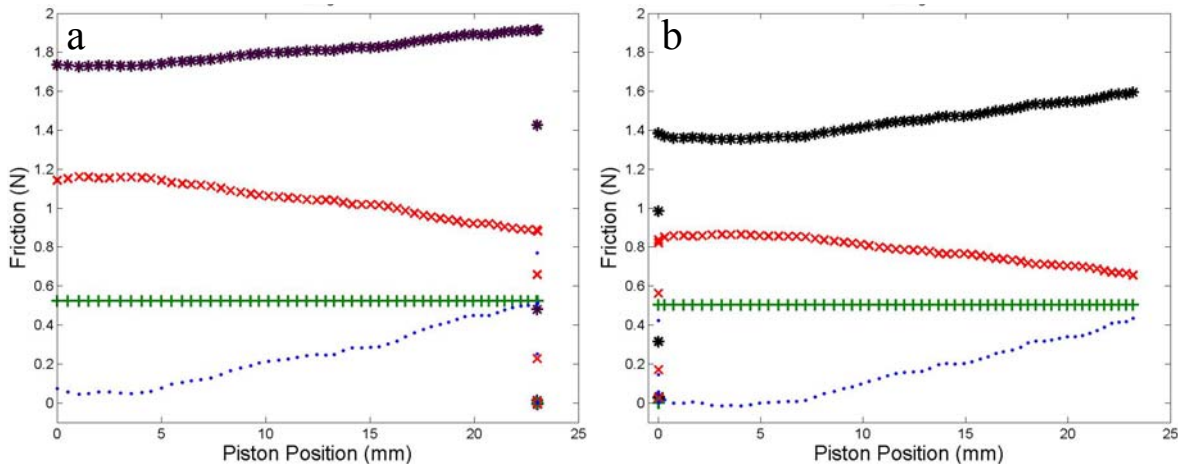

Figure 4.17: Friction forces acting on the piston head and actuator shaft F_{side} (•), F_{teflon} (+), $F_{inertia}$ (×), and F_{total} (*) for upward (a) and downward (b) piston motions

A comparison of Figure 4.17a and b further confirms that the decrease in velocity for the upward motion and the increase in velocity for the downward motion are a result of the increasing and decreasing side loading on the piston head. Figure 4.17 shows that as the piston rises, the side load on the piston head continually increases. As the side load increases due to the increased rigidity of the actuator shaft (Figure 4.13), the piston slows down. This reduction in velocity lowers the viscous losses associated with expelling the fluid from the upper cavity to the return tank as the piston moves through its range of motion, as seen in Figure 4.17. The resultant friction force acting on the piston as it moves downward is decreasing for the same reason that the resultant friction force acting on the piston as it moves upward is increasing. As seen in Figure 4.17, the side loading on the piston head (f_{side}) reaches a minimum at approximately 5 mm. This corresponds to the minimum pressure difference across the piston (Figure 4.12) and confirms that the misalignment of the shaft has an adverse effect on the resultant friction force acting on the piston head and actuator shaft. The pressure (viscous) losses as computed from poiseuille flow are approximately 40% smaller than the measured losses presented in Figure 4.17. This discrepancy may be attributed to small variations in the internal channel diameter where the tolerance owing to the stereolithography can be on the order of 0.25 mm.

4.8 5x5 System Implementation

Figure 4.18 shows an assembled 5x5 actuator array that integrates all of the components needed to drive a single actuator. The internal geometry of each actuator is identical to that of the actuator characterized in Chapter 2 of Garth's MS Thesis. However, a number of external modifications were made in order to accommodate an electronics board and allow the module to be easily plugged into the base plate and seal properly. When the fluidic actuator is plugged into the fluidic base plate it also plugs into an electronics board which contains communication ports for the control of each individual actuator. A pressure tank (pressurized by air) supplies pressurized fluid to the actuators through the fluidic base plate shown in Figure 4.18. The low pressure fluid from each actuator flows into the return tank and is pumped into the pressurized tank by built-in pumps.

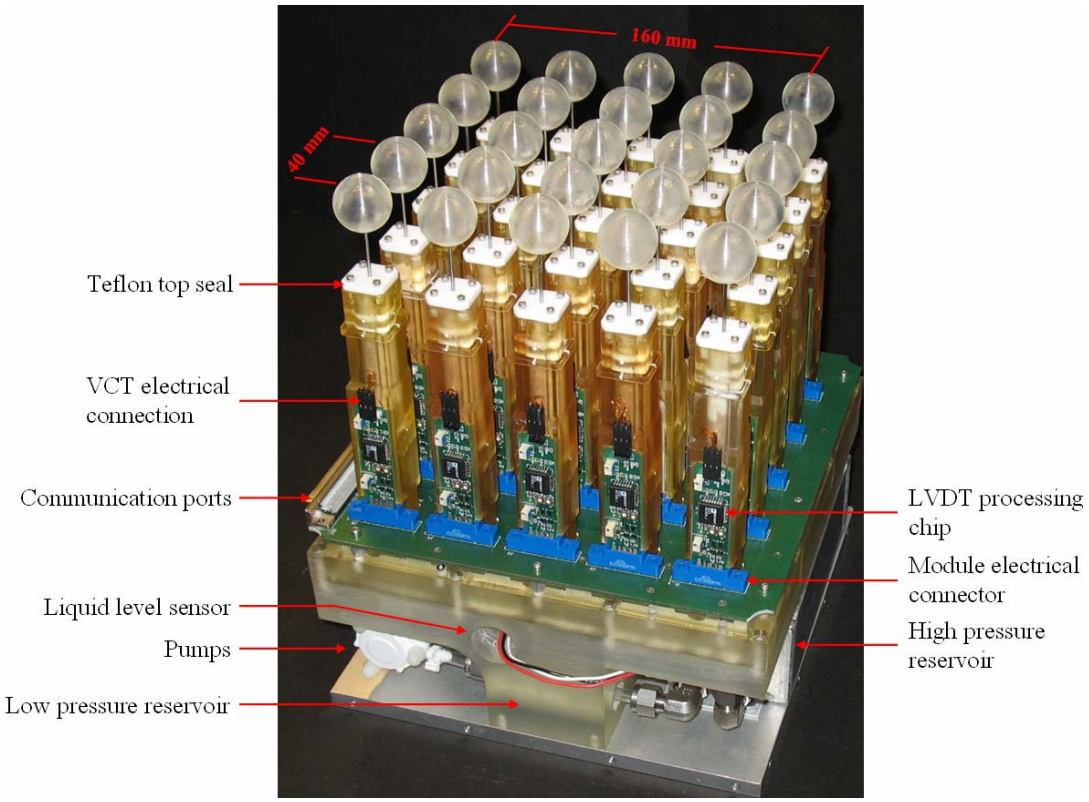

Figure 4.18: 5x5 Implementation

The pistons of the array are equally spaced on a square grid (3x3 cm) placed on a larger base plate. As shown in Chapter 4 (Figure 12), the pressure difference across the fluid line which connects the fluidic actuator to the return tank has nearly the same magnitude as the pressure difference across the piston head. For this reason, the fluid lines used to connect the actuators to the return tank in the 5x5 array are channels which go directly to the fluidic base. This augmentation greatly reduces the pressure difference needed to move the working fluid from the actuators to the return tank by reducing the losses in the channels. This reduction in losses provides a greater pressure difference across the pistons which will yield larger piston speed and force.

In the integrated 5x5 array, a linear variable differential transformer signal processing chip (AD 698AP) is used to excite the primary coil, read the induced voltage in the secondary coil, and demodulate the signal. The use of this chip reduces the hardware volume that is necessary to run the system and increases the modularity of each actuator. The demodulated signal from each actuator is sampled by a data acquisition computer, which is attached to the electronics board through the analog output communications ports. The control algorithm is used to control the 5x5 array. However, a packet containing the desired piston positions can be sent over the internet, allowing Digital Clay to be controller remotely.

As discussed in section 4.7, the piston head can become misaligned during the manufacturing process. The method used to attach the piston heads to the piston rods used in the 5x5 array is shown in Figure 4.19. The attachment method shown in Figure 4.19 uses a threaded end and nut to alleviate the need to enlarge the preexisting cavity in the graphite piston head.

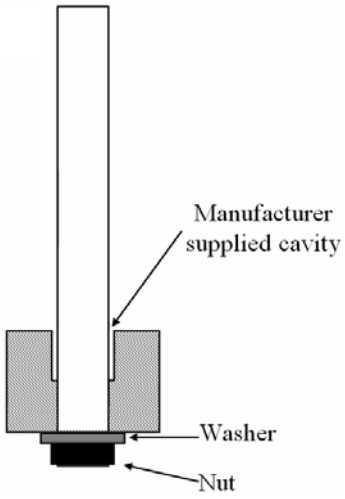

Figure 4.19: Improved piston head attachment method

While the attachment method discussed in section II.6 allows the piston rod to flex about its longitudinal axis the method shown in Figure 19 is significantly easier to manufacture and provides sufficient flexibility for practical applications of Digital Clay. Furthermore, the side loading on the piston head (section II.7) as the piston moves upward is significantly reduced.

1.1.1 II.9 Salient Characteristics of Digital Clay

The compact 5x5 Digital Clay array of fluidic actuators is easily scalable. The main hindrance to the scalability of a single fluidic actuator was the size of the solenoid valves that were used during the characterization of the single fluidic actuator (chapters 2-4 of Garth's MS thesis). However, such valves are inherently scaleable and can be fabricated at the micro-scale. It is anticipated that ultimately, the electronics boards attached to each

actuator and the desired output force will be the limiting scalability factors. While the inclusion of a hydraulics system to drive the array demands the presence of two reservoirs and a pumping system, the lack of mechanical actuators (e.g. FEELEX, Chapter 1, Garth, MS thesis) enables a compact and scalable solution.

The present Digital Clay provides substantially improved position monitoring over previous tactile arrays by using embedded absolute position sensors in each actuator rather than relying on external measurement devices or inferring position from integration of system parameters. The present approach not only yields a scalable tactile array, but provides a very modular solution in which each individual actuator contains all of the necessary hardware to be self functioning. This means that any actuator in the array can be easily removed and replaced/relocated at any time without loss of accuracy and functionality. The array contains all necessary components for its operation in a neatly packaged base which integrates the fluid system with the drive and control electronics and communications.

4.10 Future System Improvements

The form of Digital Clay presented in this work provides the ability for a user to economically represent and interact with a desk-top sized topography through a remote software package. However, there are a number of improvements that can be made. While Digital Clay is functional with respect to position control, it does not contain the ability to measure the force effected by or on the pistons. Therefore, the inclusion of force measuring capabilities would greatly enhance the present design of Digital Clay.

The linear variable differential transformer chip attached to each actuator of the 5x5 array consumes approximately 40 mA. This current can be significantly reduced if a finer wire is used to build the variable core transformer (currently made with 34 gauge wire). A smaller diameter wire will also enable a higher sensitivity along with additional turns per unit length of the coil.

As noted in Chapter 3 of Garth's thesis, the current VCT design suffers from reduced sensitivity at the end of the piston's range of motion (Figure 18 Chapter 3, Garth's MS thesis) because the piston rod is only partially immersed in the changing magnetic field of the primary coil. One way to mitigate this issue is to move the access hole in the glass tube closer to the top and modify the insertion depth of the Teflon top seal as shown in Figure 4.20b. This modification would allow the VCT to be wound on a longer segment of the glass tube and therefore allow the piston rod to have a longer immersion length in the magnetic field of the VCT in the fully extended position (Figure 4.20b).

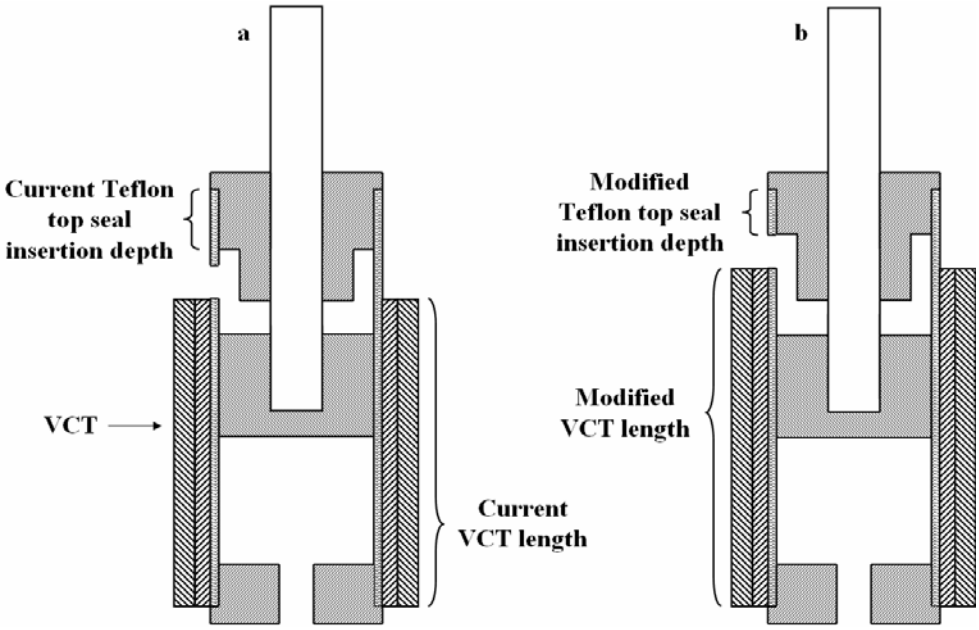

Figure 4.20: Current (a) and proposed (b) Teflon top seal and VCT

Finally, the use of pulse width modulation for actuation of the valves would add the ability to control the solenoid valves proportionally, which would give the Digital Clay system an enhanced ability to display moving curved surfaces, and changing velocity trajectories.

Section 5

Realization of a Functional Prototype Device (Book)

Test results of proposed control methods on the 5x5 prototype

A 5x5 fully functional cell array prototype has been designed and implemented as shown in Figure 5.1. The emphasis of the design was to provide the essential functionality in a scalable layout and control architecture. This has been achieve at a spatial pitch of 5mm and could potentially be achieved at even a finer pitch. Results included here on the above 5x5 array prototype are limited due to space but included to illustrate the satisfactory integrated functioning of all components. The first test is to create a stationary surface. As a test, the working surface is commanded to achieve a slanted plane as shown in figure 5.1. The commanded and measured (using machine vision) surface matrices of the working surface given below show less than 0.8 mm error (no filtering, no calibration). Please note that there are lots of means to measure the final surface. However, machine vision provides a simple independent way and requires less setup and cost for the preliminary experimental purpose.

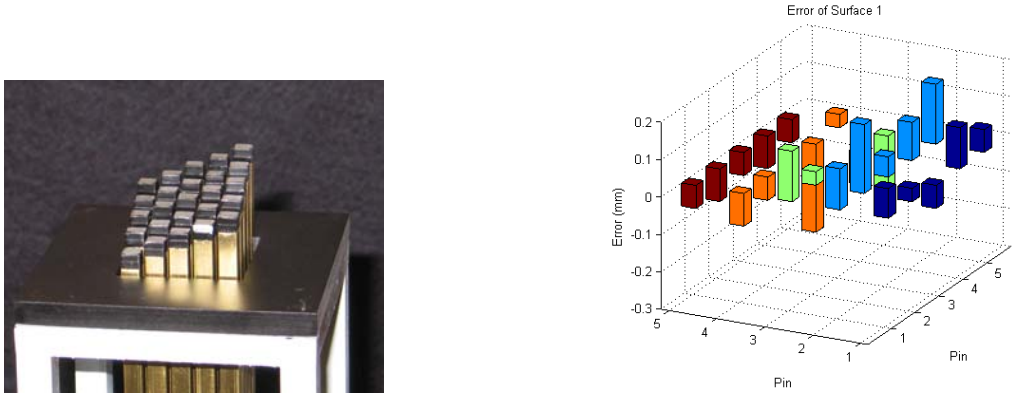

Figure 5.1 Slanted Plane Measured by Camera.

A number of shapes have been generated and the corresponding accuracy tested. For sake of brevity these will not be presented, but the typical error is less than 0.2 mm.

To test the velocity control ability of the proposed PWM flow control method, a single rod is commanded to track a sinusoidal trajectory. The measured results are shown in Figure 5.2. The dashed line is the commanded trajectory and the hollow dots represent the measured displacement.

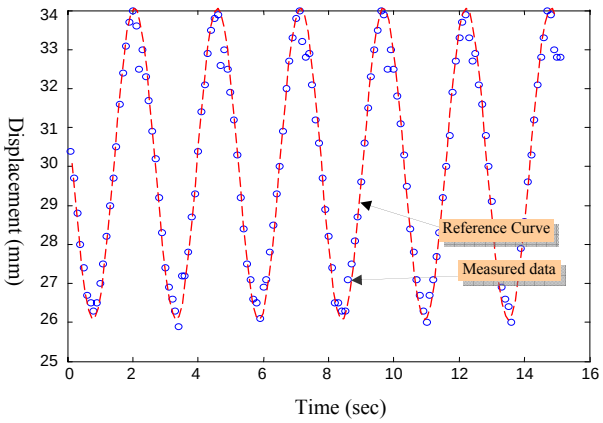

Figure 5.2 Tracking a Sinusoidal Curve

The novel position sensors are a critical component in achieving our goals. The accuracy of this approach is much greater than necessary for Digital Clay. Here we are limited by the uniformity of deposition of the resistive film which was done in our laboratory. The accuracy for the prototype is as shown in Figure 5.3.

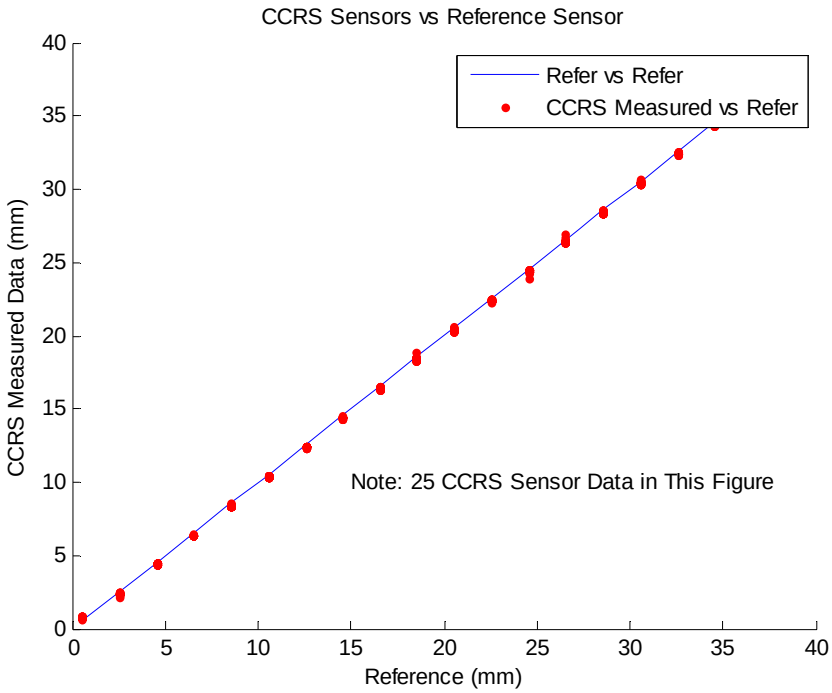

Figure 5.3a Position sensor readout for 25 sensors as the range of motion is covered.

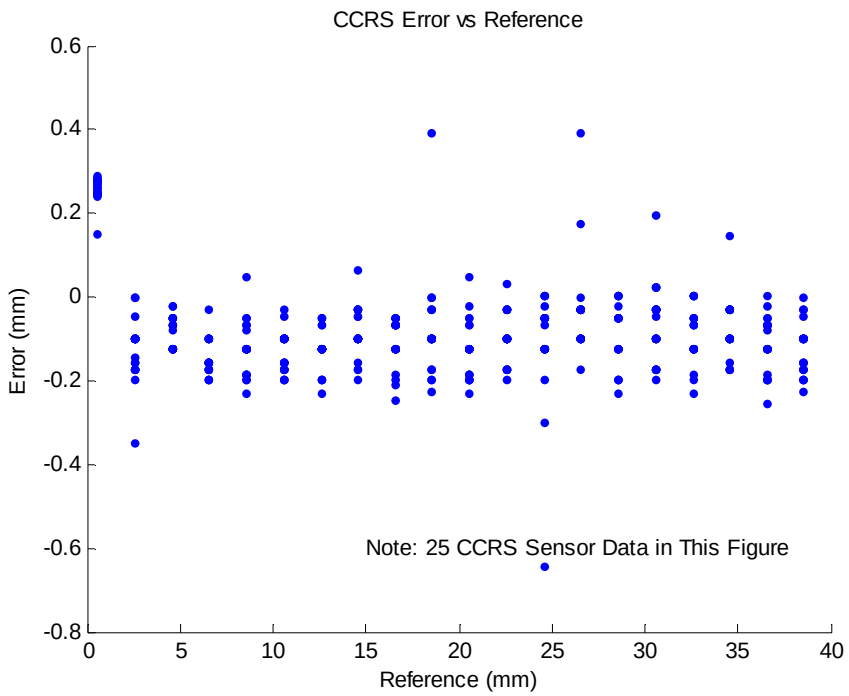

Figure 5.3b Sensor position errors over the range of motion.

Section 6

Paradigms for Direct Human-Shape Interaction (Rossignac)

We discuss the major findings for each one of the activities listed above:

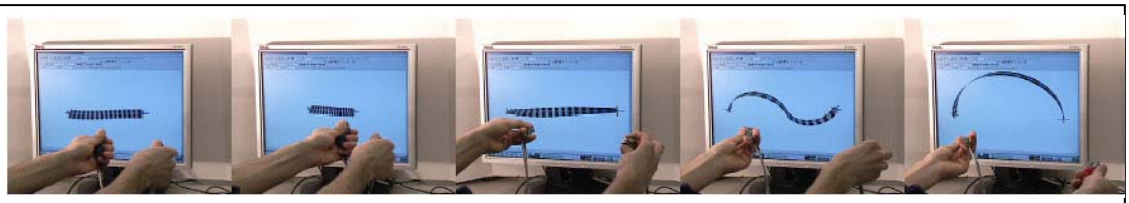

Intuitive control of a ribbon's shape and twist with two hands

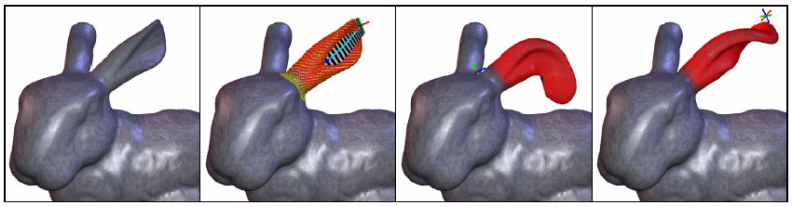

Using the ribbon to select, twist, and bend a portion of the model

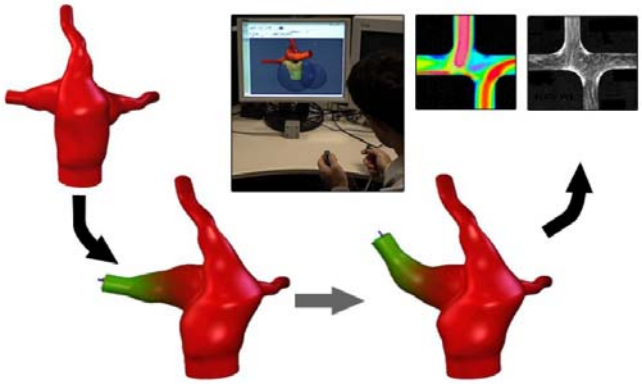

Figure 6.1. Bender is used in surgical planning to edit a 3D model of a junction of vessels. The resulting shape is used to evaluate blood flow using CFD.

Bender: Two models of a ribbon (one based on a **bi-arc** central wire and one on a screw interplation of the transversal twist) have been developed. The shape of the wire and the twist around it are easily controlled by the user by holding a 3D tracker in each hand. Various issues of numeric instability, tearing of space, and map discontinuities have been identified and resolved. A paper describing the Bender system and the underlying technology was presented at the ACM Symposium on Solid and Physical Modeling in June 2005. Bender has become one of the most popular demonstrations of the GVU

center, because it permits users to easily create and edit 3D shapes. Its functionality has attracted the attention of Prof. Yoganathan from the BioMedical Engineering Department at Georgia Tech. Jointly, we are exploring the use of Bender for the interactive design and offline simulation of pediatric cardiovascular surgeries such as the Fontan procedure. Quickly reshaping proposed blood vessel configurations will allow more rapid discovery of optimal shapes for efficient blood flow.

GeoFilter: Previously proposed shape filters have two limitations. First, they only use implicit or explicit forms that often limit the filter performance. Second, their parameters are not directly related to shape measures and are hence difficult to select. Terefore, filter design was usually a tedious trial-and-error process. We have developed a new filter design approach that utilizes both implicit and explicit forms by which a broader class of filters can be constructed. Also, our filter framework suggests how to relate the filter coefficients to the size of the mesh feature. We allow the user to select a feature by touching it. The extent of the feature is controlled by spraying a selective paint from the contact point. As the user waits or changes the contact point, the selective paint invades the desired region. Then the dominant frequency is extracted from the selected region and is used to set up the filter parameters. A novel filter formulation based on a rational quadratic polynomial provides a good compromise between computational cost and the power of the filter to select a narrow band and attenuate or exaggerate it. A paper describing this contribution was presented at the Eurographics conference in September 2005.

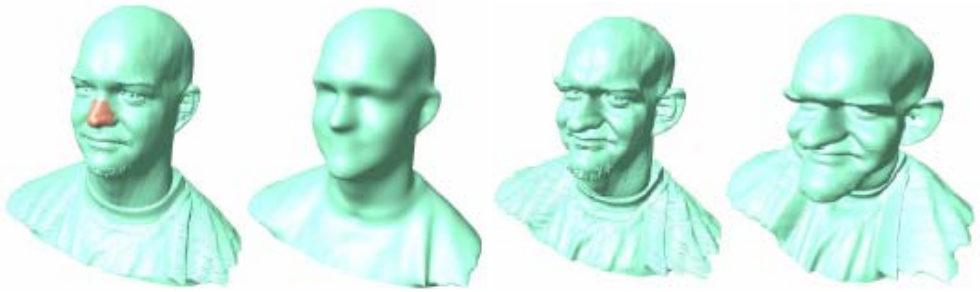

Figure 6.2. The user has touched the tip of the nose to select the feature. The measurements from the nose were used to define the parameters of three different filters: a low-pass smoothing filter, a high-pass exaggeration filter that makes the face look older, and a band-pass exaggeration filter.

Tritops: As a compromise between the interface popular today (2D mouse) and the not-yet-available full fledged version of Digital Clay, we have developed a new concept that is best described as a mouse with 3 horns. Hence the name "tritops". Each horn is a computer-controlled piston serving as an independent input and output device. By placing a finger at the tip of each horn, the user will be able to control the position and orientation of the mouse (mobile base) and to sense and apply pressure to the pistons. PhD student Ignacio Llamas and Master's student Gordon Brown under the joint supervision of Drs. Rossignac and Shaw have been collaborating with students and staff from ME to design and manufacture a passive prototype of the Tritops. It has been equipped with passive springs and a Polhemus 3D tracker and has been interfaced with the Twister software for preliminary testing. We have explored the suitability of this interaction mode. These preliminary studies have identified the need for further research in the mapping of the limited height range of the pistons to the desired wide range of motions needed for editing a digital clay model. Given that the hand motion controls both position and orientation of a selected portion of the surface, the mapping between the position and orientation of the tritops and the position and orientation of the selected surface portion must be exaggerated. Further research is needed to identify an exaggeration model that will be both intuitive and effective.

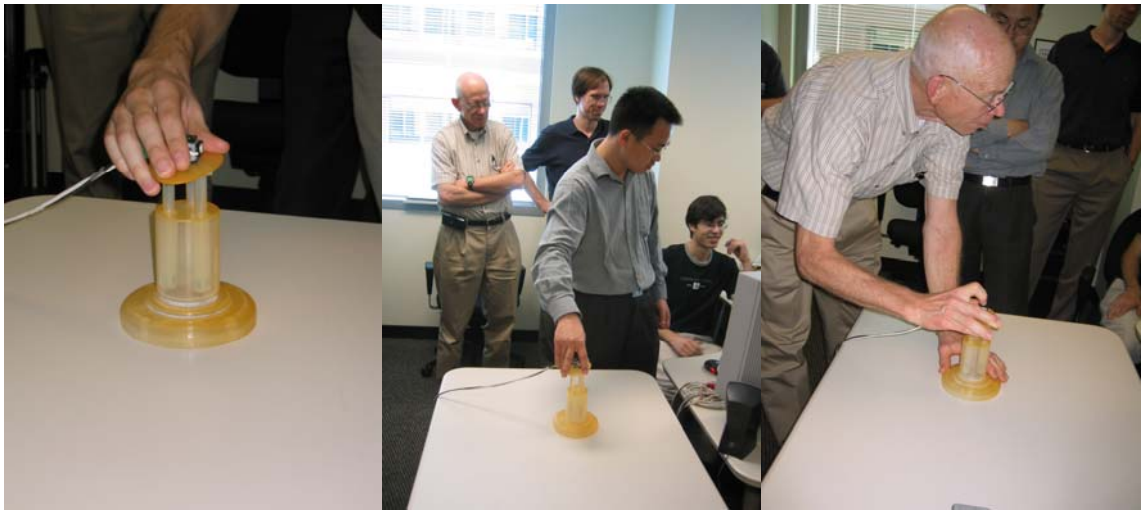

Figure 6.3 Using TriTops

FlowFixer: We anticipate that the Digital Clay will be capable of simulating not only the interaction with solid shapes, but also the interaction with responsive media, such as fluids. Hence, we are exploring new simulation techniques that strive for a compromise between accuracy, simplicity, and speed. The Back and Forth Error Compensation and Correction technique provides such a compromise. It avoids the unnecessary dissipation/diffusion of the momentum or any other property advected along the flow. Also it avoids the need for particle tracing when simulating the liquid/solid or liquid/air interfaces while preventing volume loss and undesirable advection. The results have been published in a workshop and an archival Journal.

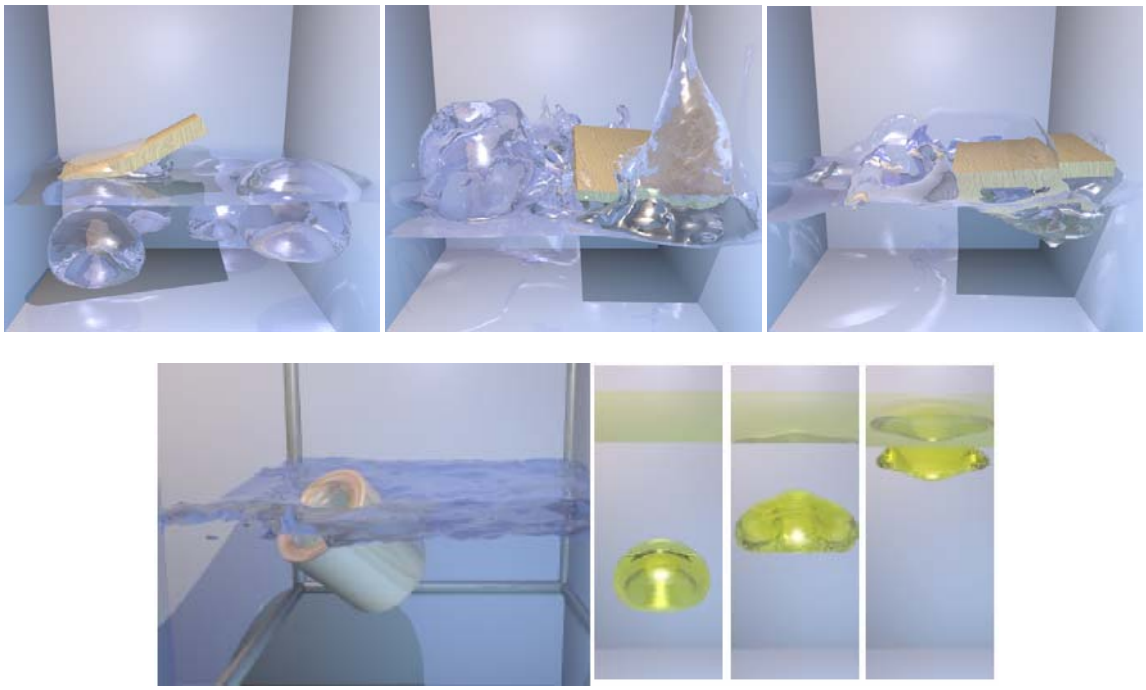

Figure 6.4. Fast and accurate liquid/air/solid interaction simulation using Back and Forth Error Compensation and Correction (BFECC). The use of BFECC avoids the need for the expensive and delicate particle tracing. Yet, it produces realistic simulations of the interaction of a liquid with air and floating or sinking solids and the behavior of oil bubbles rising in water.

Simulation of Thin Liquid Film: To further our understanding of how to simulate materials with a variety of haptic properties, we study the simulation of the thin liquid film towards the formation of realistic models of foam. The simulation of liquid films is challenging since they quickly become thinner than the grid resolution, which leads to premature bursting or merging of the bubbles. We prevent this thinning process by applying a disjoining force to the film, obtaining bubbles that last much longer without bursting or merging. The surface tension on the liquid film is the next difficulty. Since the level set is not differentiable at the center of the thin liquid film, the curvature computed from the level set gradient is noisy, and the thin liquid film ruptures quickly. To prevent this, we compute the surface tension from the local isosurface, obtaining long-lasting liquid films. However, since bubbles stay longer without bursting or merging, the volume loss of each bubble is noticeable. To solve this problem, we modify the pressure projection to produce a velocity field whose divergence is controlled by the proportional and integral feedback. This allows us to preserve the volume or, if desired, to inflate or deflate the bubbles. In addition to premature bursting and volume change, another difficulty is the complicated liquid surface, which increases memory and computational costs. To reduce storage requirement, we collocate the velocity and pressure to simplify the octree mesh. To reduce the computational complexity of the pressure projection, we use a multigrid method. This work is reported in a technical report GIT-GVU-0610 and will be submitted for publication.

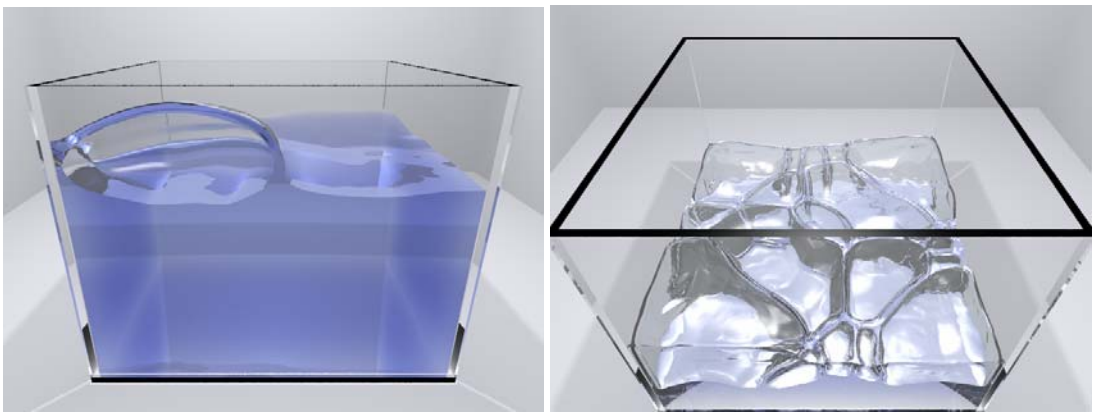

Figure 6.5. Simulation of a Thin Liquid Film

ACTIVITIES

Overview

The Digital Clay project sought to produce a computer interface that provided a tangible surface display to a user with appropriate haptic response. Digital Clay should accept direct tactile user input relevant to the shape displayed and it should relate that input to some of the tasks that shape definition and interaction are relevant to, such as engineering and artistic design, scientific and medical exploration, communication with the visually impaired and presentation of other topographical data. To achieve this formidable task, several specializations were enlisted. The performance of research in this grant was carried out under the direction of six faculty: Wayne Book, roboticist with interests in haptics, fluid power and controls who served as overall project director (Section 5); Imme Ebert-Uphoff, (Section 1), who studied various kinematic and structural approaches to the construction of surfaces; Jarek Rossignac, (Section 6), a computer scientist with special interests in shape creation and representation; David Rosen, (Section 3), with depth in rapid prototyping and manufacturing, and computer aided design; Mark Allen, (Section 2), a MEMS expert who works with fluid valves and actuators that assist in miniaturization of any device and Ari Glezer, (Section 4), an expert in fluid mechanics with interests in novel application of fluids. The final report on this project is assembled from information provided by each of these experts.

While many of the original objectives of the grant were achieved, some results were not available in time to be incorporated into an integrated experiment. Also, the reduction to one-half of the funding requested curtailed full integration of the project's results. For example, the prototypes constructed would have benefited from earlier availability of the MEMS valves which were available only near the end of the grant period. Nevertheless, as the report and the "nuggets" provided will show, scientific and technical results were achieved with valuable broader impacts.

The sequence in which the results are presented have a logic based on the evolution of the research. Note that earlier annual reports contain some work relevant to the final product which is not repeated here. The conceptualization of basic approach from a kinematic and structural viewpoint by Imme Ebert-Uphoff and her student is presented first. The MEMS research produced valves and actuators which were a basic component of implementation and thus Mark Allen's detailed report is presented second. Next, the work by David Rosen studying how one of the implementations could be manufactured is presented. Ari Glezer and his student present studies of the fluid mechanics issues in an implementation using fluid power for an implementation. The production of an integrated device that is capable of communicating with both the user and various computer programs is then presented as composed by Wayne Book and his student. Finally, shape creation and modification approaches that might employ the integrated device are presented by Jarek Rossignac. This last presentation could have arguably been presented first, but some of the devices used in that research are more easily understood if it is last.

Section 1

Assembly Sequence Generation for Shape Display (Ebert-Uphoff)

Sebastien Wolff focused on the concept of recyclable rapid prototyping. The proposed innovation consists of having an automated device assemble shapes instead of being the shape. The main idea is for a robot to autonomously be able to build a structure to fit any prescribed shape. The main challenge addressed here is to develop an assembly sequence that will ensure that the structure can be built in a statically stable manner. One way to think of the proposed device is as scalable and recyclable rapid prototyping: recyclable, since blocks used in one prototype can be disassembled and re-used for future prototypes, and scalable, since the procedure can be applied to a wide range of block sizes, ranging from tiny MEMS parts to huge hollow wood blocks.

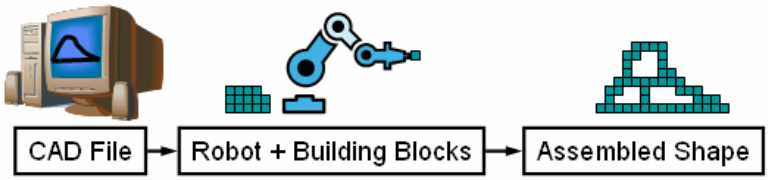

Figure 1.1 - Recyclable Rapid Prototyping

Figure 1.1 shows the basic procedure of recyclable rapid prototyping for shape display. The user provides a CAD file. A robot then assembles the shape from a large number of identical building blocks. Simple, identical 6-sided blocks are used for the block models for the time being. The intent is to keep the model general so that results are applicable for many block types.

The main contribution of this work was to make assembly sequence generation for a large number of parts time-feasible. There are **two primary challenges** for time-feasibility:

1. Exponential search space: The search space for assembly sequences is exponential in the number of parts and thus searching *all* possibilities is impossible.

2. Static stability tests are time-consuming, particularly with FEM testing: Even a search of only a polynomial number of assembly sequences may not be time-feasible if static stability has to be tested explicitly for every considered sequence.

The first challenge above (exponential search space) was addressed by viewing this problem as a search space reduction problem. In the developed algorithm, high-level rules drastically reduce the search-space by identifying a portion of the structure to be assembled first. A mid-level rule decides what order to assemble those blocks in. Low-level rules are invoked at every step to see what blocks are viable options. It should be noted that mid-level rules can also be used on their own to assemble structures, as well as in conjunction with high-level rules.

The second challenge above (time-consuming static stability test) was addressed by designing the rules specifically to address static stability as far as possible in open-loop. Namely, the rules are designed to generate an assembly sequence that is already likely to be statically stable, and static stability is only tested at the very end, once the final assembly sequence is generated. Therefore it was crucial to understand the behavior of all rules in various scenarios to be able to predict which ones yield the best static results.

The bulk of the work was in developing a large number of mid-level and high-level rules, which are detailed in the dissertation of Sebastien Wolff. Each rule was tested to see how they behaved and which yielded the smallest forces and moments at the block connections for each structure. The procedure derived to obtain a description of the general behavior of each algorithm is as follows:

1. Apply the algorithm to many (or all) sample structures to generate the assembly sequences. Both accessibility and connectivity is verified before assembling / removing any block.

2. For each assembly sequence, the analysis tools that were developed are used to investigate the largest forces and moments, which are the potential failures.

3. Visually inspect the assembly sequence using the animation tools to look for any unusual or unexpected behavior.

4. Assemble a list of all observations from (2) and (3) and identify the specific properties of the algorithm that are responsible for this behavior.

5. Summarize all findings and document them in the dissertation. There is certainly no guarantee that this procedure can identify all problems or issues that can arise for any of the algorithms, simply because the number and nature of sample structures being considered is limited. However, tremendous insight was gained in the general behavior of the algorithms that helps select the best candidates.

Simulation Framework: A testing and visualization package was developed, and allows the user to input a structure (matrix) and assembly sequence (list of matrices), and can output the maximum forces and moments that occur at the connections at any step of assembly, and can animate the entire assembly. All coding is performed in Matlab, using Femlab for finite-element modeling.

Prior Work in Annual Report: The early years of work by Ebert-Uphoff and her student, Bosch, created an alternative for a ball joint that could be readily fabricated using rapid prototyping techniques. This concept will be seen in the manufacturing work by David Rosen and his student.

Section 2
Development of Actuators for Scalable Arrays (Allen)

Major research and education activities of the project

The role of the MEMS group (led by Dr. Mark Allen) in this project is to develop scalable actuator arrays for digital clay, so that microactuator arrays can be built larger in overall extent while maintaining the high resolution offered by MEMS manufacturing techniques.

Our major research approach is the design and fabrication of the two crucial components, microfluidic valves and fluidic-driven actuators that are each controlled by a dedicated valve. While the fluidic-driven actuators acting together with a stereolithographically fabricated scaffold give the surface topography of three-dimensional objects.

The work during the current reporting period has concentrated on the development of non-conventional MEMS fabrication technologies for both valves and fluidic actuators, each described in detail in the following sections.

2.1 Development of microfluidic valves
2.1.1 Piezoelectric multilayer actuator

Piezoelectricity was selected as the actuation mechanism for the microvalves due to the inherent advantages of high bandwidth, large force, and low power consumption. We have been working on developing new MEMS fabrication scheme for the multilayer piezoelectric actuator. A proven fast and economical approach, dicing, was adopted to fabricate freestanding PZT grooves. PZT multilayer actuators were successful fabricated by the proposed method that involved bulk PZT dicing, SU-8 photolithography and laser ablation. Optimization has been made to the fabrication scheme to further simplify the process. PZT multilayer actuators which are fabricated through the optimized process were characterized.

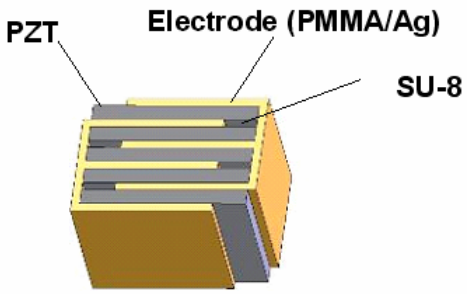

Figure 2.1 Schematic of PZT multilayer actuator

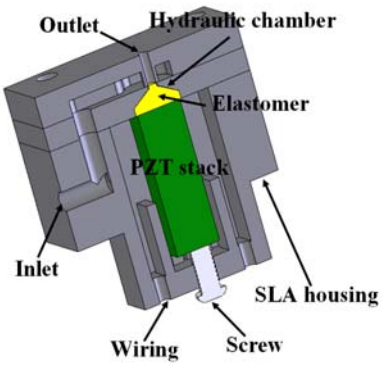

Figure 2.2. Schematic of the piezoelectrically driven and hydraulically amplified polymer microvalve

Piezoelectrically actuated microvalve with solid hydraulic amplification

Piezoelectric multilayer actuators are favorable for driving microvalves at high pressure and high frequency. However, their drawback is small stroke

(up to 0.1% strain) even at a large applied voltage, which restricts orifice gap and in turn limits maximum achievable flow rate. We developed a piezoelectrically-driven and hydraulically-amplified axial polymer microvalve. The normally open microvalve was fabricated and assembled primarily with stereolithographically (SLA) fabricated polymer components. An incompressible elastomer was used as a solid hydraulic medium to convert the small axial displacement of a piezoelectric actuator into a large valve head stroke while maintaining a large blocking force. Also, the axial design of the microvalve enables densely-packed valve arrays. The function of the microvalve as an on-off switch for a pneumatic microbubble tactile actuator was demonstrated.

2.2 Development of micro-bubble Actuators:

2.2.1 Endoskeletal microbubble actuator

Actuators for digital clay must possess the following attributes: (1) ability to generate large deflections for tactile input/output; (2) ability to generate large forces to interact with human input; and (3) mass-manufacturability to ensure the economical formation of large arrays.

After reviewing and comparing several possible types of pneumatic microactuators that can be fabricated by MEMS technology, we have developed and characterized a mass-manufacturable endoskeletal microbubble actuator as shown in Figure 2.3. These pneumatically-actuated devices combine the desirable large deflections of balloon-type actuators with the preferentially-axial deflection of bellows type actuators to produce actuators capable of large deflections in axial directions. This kinematic stabilization is achieved by use of integrated "skeletons" – structures to support desired deflections and suppress unwanted deflections, which underlie the actuator "skin" – elastic structures to help an extended actuator recoil to its original shape. The actuators have been fabricated and characterized, as well as compared with pure-bubble actuators (skin-only) and pure-bellows actuators (skeleton-only) of the same materials and dimensions.

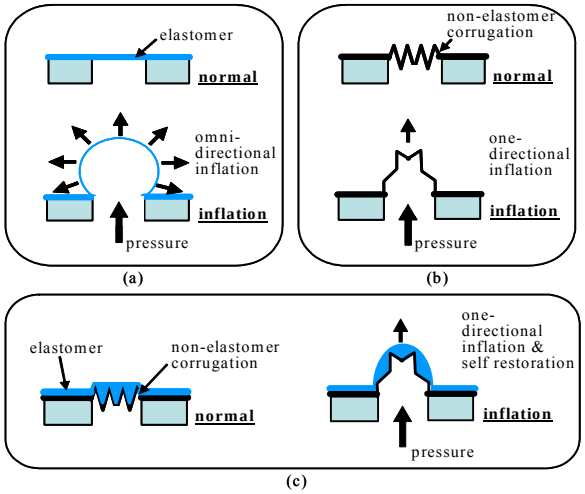

Figure 2.3. Various microbubble actuators: (a) elastomeric balloon, (b) non-elastomer-based corrugated diaphragm, (c) endoskeletal microbubble

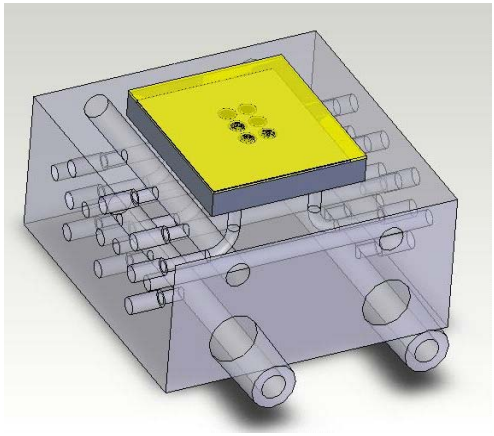

Figure 2.4. Schematic of the miniaturized refreshable Braille cell

Application of miniaturized microbubble actuator: refreshable Braille display

The design of endoskeletal microbubble actuator has been miniaturized and optimized. An array of 2 x 3 miniaturized microbubble actuator array was employed to form a cell of the refreshable Braille display (RBD) as shown in Figure 2.4. RBD is the device converting text information from a computer to Braille dots for the blind to read. In our design, the shape of the Braille dot is more distinguishable and large force can be obtained at large displacement compare with elastomer balloon actuator. Further, by minimizing overall bubble volume and maximizing overall bubble vertical deflection, the quantity of pneumatic gas used per cycle can be minimized.

The section on findings describes our research work in more detail.

Section 3

Creation of Formable Surfaces (Rosen)

Dr. Rosen is currently working with a Mechanical Engineering graduate student, Ted Anderson, to create a formable surface to be used in digital clay devices. This work is a continuation of previous students' research endeavors in the formable surface and manufacturing areas. Figure 3.1a shows the completion of a design from previous research for a compliant spherical joint (or unit cell), where the L_i's are the main kinematic links and the $\hat{a}_i$ vectors denote compliant revolute joints. Figure 3.1b illustrates how arrays of these joints can be fabricated to create a surface. The link connections between the compliant spherical joints, where the L_i's are located in Figure 3.1a, are rigid links. Figure 3.1c shows a modified model of the unit cell with leaf spring connections. Instead of having rigid links as illustrated in Figure 3.1b, the development of the leaf spring connections has made it possible for the surface to stretch. These leaf spring connections are the new L_i's where the unit cells are attached to one another to form the arrays that make up the surface.

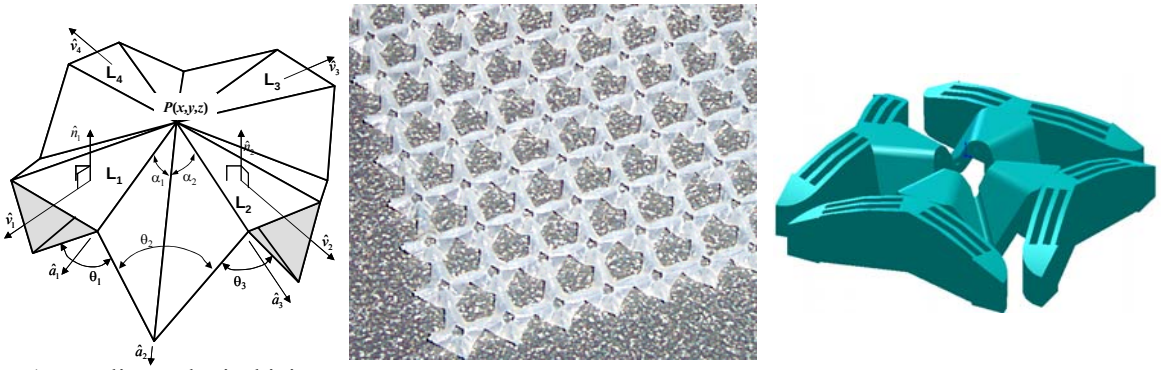

a) compliant spherical joint. b) array of joints. c) compliant spherical joint with leaf springs.

Figure 3.1 - Manufacturable crust

Three main activities were performed this year: modeling of deformed surface shapes, determining spring constants, and developing a digital clay demonstration device. The modeling of the deformed surface includes the capability of the surface to stretch and utilizes the physical properties, spring constants, of the manufactured unit cells.

3.1 Deformed Surface Modeling: Two different mathematical models were developed to predict the surface shape and form. These two models were then compared for how accurately they mimic the physical features of the formable surface. The CAD model of the formable surface is shown in Figure 3.2a. Both mathematical models are based upon translational springs to express the stiffness of the leaf springs. The first model had two rotational springs, one in the x-direction and one in the y-direction, in 180 degree formations to represent the stiffnesses of the compliant spherical joints. Figure 3.2b shows the spring representation of the first model. In addition to the two rotational springs in the first model, the second model had four rotational springs in 90 degree formations in the X-Y plane to model the stiffnesses of the compliant joints between neighboring links, as shown in Figure 3.2c. An energy minimization objective is used to find the location of the unit cells in the distorted surface.

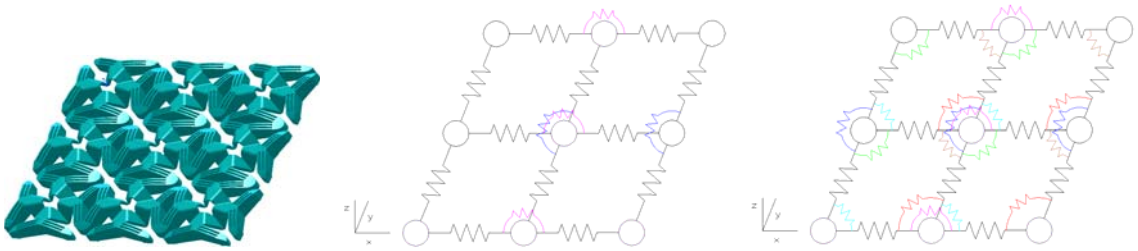

a) CAD model of surface. b) first math model of c) second math model of surface.

Figure 3.2 - Manufacturable crust

3.2 Spring Constant Determination: For the mathematical models to accurately portray the physical properties of the unit cells, the spring constants need to be found. Several unit cells were manufactured using stereolithography and tested to acquire the values of the spring constant of the leaf springs on the unit cells. The values obtained from the tests were then substituted into the mathematical models. An ANSYS model of the unit cell was constructed to ensure the experimental values of the leaf springs were correct. Since resin material properties can vary, a range was used in the ANSYS modeling for Young's Modulus and Poisson's Ratio, but the required force was kept constant.

3.3 Demonstration Digital Clay Device: The last part of this research involves the development of a manufactured model of the digital clay device. The digital clay device includes a computer-interfaced bed of nails array that is bounded by the formable surface. The bed of nails consists of densely packed actuators that displace vertically and can sense pressure changes and adjust the height to replicate a digital model through simulation or received data. See Figure 3.3 for an example of the bed of nails with the red surface representing the formable crust.

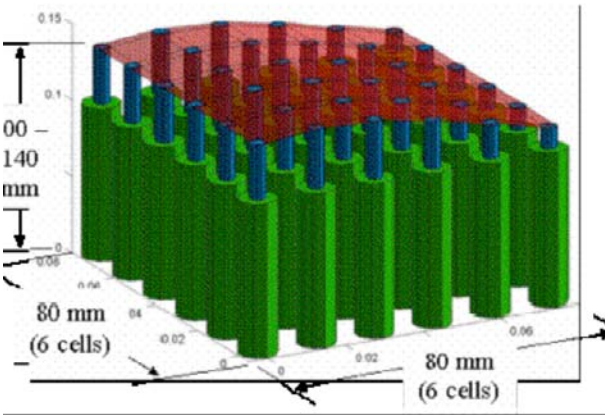

Figure 3.3 – A display of the bed of nails with the attached formable surface

Section 4
Fluidic Driven Digital Clay (Glezer)

4.1. Activities

Digital Clay is a tactile array of linear fluidic actuators which provide distributed sensing and position control through the use of an embedded position sensor. The actuator implementation is achieved by two-way hydraulically-driven pistons which are integrated with computer controlled valves. Each actuator is connected to an underlying base plate which is in fluidic communication with high and low pressure reservoirs. The research focuses on the aspects of the fluidics necessary to operate the actuators and control actuation of Digital Clay. The main objectives of this work are the characterization of the fluid flow through the system and the design and implementation of an embedded inductance-based position sensor. Each actuator in Digital Clay is individually addressable and is controlled through the use of a closed-loop proportional integral controller with position feedback from the embedded inductance-based sensor. Also presented in this work is the characterization of an individual fluidic actuator and the realization of a 5x5 tactile array of actuators.

The Georgia Tech Digital Clay project focused on the development of two test beds. The first test bed (TB1), developed by Zhu (Zhu 2005), was comprised of a 5x5 tactile array of hydraulically actuated cylinders. It uses pressure sensors for force feedback and a capacitance based position sensor. While the capacitance based sensor is capable of accurately measuring positions down to 0.3 mm, it requires a wire to be attached to the piston rod, which decreases the robustness of the system as it can easily be broken or detached from the piston rod. This Digital Clay test bed (TB1) uses a combination of water and air as the working fluids. Water is used to move the cylinder up and a constant air pressure is used to move the cylinder down. Therefore, if the driving pressure is less than the air pressure in the cylinder the piston moves down and vise versa. While this design alleviates the need to create a tightly sealed upper cylinder cavity, it reduces the available forces of the piston and limits its downward velocity.

The second test bed (TB2), which is described in the present dissertation, focuses on a somewhat different approach, namely, the modularity of the design, maximum output force of an individual actuator, embedded position sensor design, and driving fluid selection.

Similar to TB1, TB2 presented here consists of multiple fluidic actuator cells which are attached to a base plate that is in fluidic communication with a high- and a low-pressure reservoir. However, in this work, each fluidic actuator contains its own driving electronics and can, therefore, be inserted into any location on the base plate, allowing for multiple actuator arrangements to be constructed with out the need to change or modify the base plate. The cylinders used to create the actuators are significantly larger than those used in TB1, which allow for greater output forces by each individual actuator. The version of Digital Clay that is presented here (TB2) uses a Variable Core

Transformer (VCT) in place of the capacitance measurement system used in TB1 to create a more robust sensor. The VCT is more robust than the capacitance sensor used in TB1 because the VCT does not require a physical connection between the piston rod and the sensor electronics. Finally, silicone oil is used for the driving fluid in this work in stead of the water and air combination used in TB1. The notable characteristics of this particular fluid are its chemical compatibility with the mechanical elements of the system, its enhanced lubrication qualities, and its high permeability, which enhances the performance of the VCT.

Both of the Digital Clay test beds, developed in parallel, can be interfaced through a network, or internet connection running their respective host software packages. The capacitance based position sensor created for TB1 as well as the variable core transformer position measurement system created here are simple and economic to build and manufacture.

A single actuator is tested and characterized for implementation into a 5x5 array of actuators. In what follows, the design and implementation of the experimental apparatus and measurement techniques needed to drive and characterize a single fluidic actuator cell are presented in along with the appropriate calibration techniques. Also described below is the Variable Core Transformer used for embedded position measurement, its implementation, and its characterization.

4.2 ACTUATOR HARDWARE DEVELOPMENT

4.2.1 Fluid Loop

The operation of the actuator is shown schematically in Figure 4.1. When the piston is in motion, fluid flows from the high pressure reservoir, through the fluidic actuator, and into the low-pressure return tank. From the return tank the fluid is pumped through a filter and a check valve back into the high pressure reservoir. The system components of Digital Clay are described in detail below. Also described below are the measurement techniques that are used in the present work and their associated hardware. As seen in Figure 4.1, the primary components of the fluid loop are the fluidic actuator, the high – and low – pressure fluid reservoirs, the system pumps, a regulated pressurized air source, and the associated plumbing.

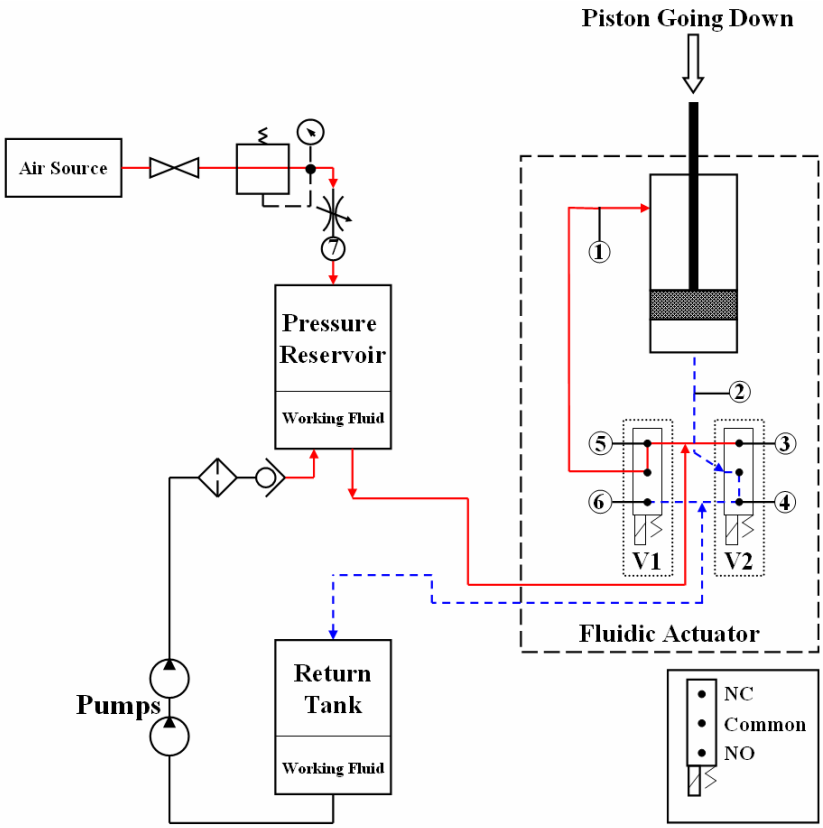

Figure 4.1: Diagram of Fluid System showing high (-) and low (--) pressure lines

The piston motion is controlled by two three port solenoid valves (V1 and V2) (Lee Company) which are shown schematically in Figure 4.1 enclosed in dotted boxes and labeled. The ports of a three-port valve are the normally closed (NC) port, the common port, and the normally open (NO) port. As seen in Figure 4.1, the pressurized fluid line is connected to the NC ports of V1 and V2 while the low-pressure fluid line is connected to the NO ports of V1 and V2. The common port of V1 is connected to the upper cavity of the cylinder and the common port of V2 is connected to the lower cavity of the piston. When either V1 or V2 is closed, it restricts fluid from flowing through the NC port, but allows fluid flow between the common port and the NO port. Similarly, when either valve is opened, it connects the NC port to the common port and allows fluid to flow between the NC port and the common port, while restricting fluid from flowing through the NO port. Therefore, when either valve is closed, the NO port is connected to the common port.

Since the piston can be actuated in either direction, both the bottom and the top cavity of the piston are filled with the working fluid at all times. In order to move the piston down, fluid must move from the pressurized reservoir, through V1, and into the upper cylinder cavity. This pressurized fluid forces the piston down while concomitantly pushing the fluid in the lower cylinder cavity through V2 and into the return tank. Both of these tasks are accomplished by opening V1. Valve V2 does not have to be open to allow fluid to flow through it as the piston moves down because the common port of V2 is connected to

the lower cylinder cavity and the valve is closed, which allows fluid to flow from the common port through the NO port and into the return tank as described above. Similarly, to move the piston up, pressurized fluid must enter into the lower cavity of the cylinder and push the piston up while the fluid that is above the piston is simultaneously allowed to exit the upper cylinder cavity and flow into the return tank; both of which are accomplished by opening V2.

Two small gear pumps (connected in series) are used to pump the fluid from the return tank back into the pressurized reservoir (30 psi) with sufficient head. Placing the pumps under the low pressure return tank provides continuous flow and alleviates the problems with pumping air bubbles through the system. A liquid level sensor within the low pressure return tank is used to turn the pumps on and off to maintain fluid between two desired levels in the return tank. A 40 μm filter between the second pump and the pressurized reservoir is used to remove particles from the working fluid.

4.2.2 Fluidic Actuator

The fluidic actuator, which is nominally 125 mm tall (30 mm travel), shown in Figure , is comprised of several components: a steel shaft, Teflon top and bottom seals, an o-ring injection sleeve, a glass cylinder, a graphite piston head, and a housing made out of stereolithography (SLA). The function of the SLA housing is to provide a modular element into which all of the above items can be inserted. The exterior of the SLA housing provides the appropriate connections and mounting surfaces for the valves and the high and low-pressure lines, which connect the actuator to the high and low-pressure fluid reservoirs, as shown in Figure 4.1. The interior of the SLA housing contains the fluid channels which connect the NC and NO valve ports to the high and low-pressure lines respectively as well as the fluid channels which connect the common valve ports to the upper and lower cylinder cavities. The glass cylinder has a hole that is approximately 2 mm in diameter drilled into its side that is nominally 17 mm from the top of the cylinder. It is through this hole that fluid passes into and out of the upper cylinder cavity. As seen in Figure , the graphite piston head is attached to the end of the steel actuator shaft and is inserted into the glass cylinder between the top and bottom Teflon seals, which are also inserted into the glass cylinder. The above assembly is wrapped with magnet wire to form the VCT, which is discussed in detail below, and inserted into a hole along the centerline of the SLA housing which is approximately 76 mm deep.

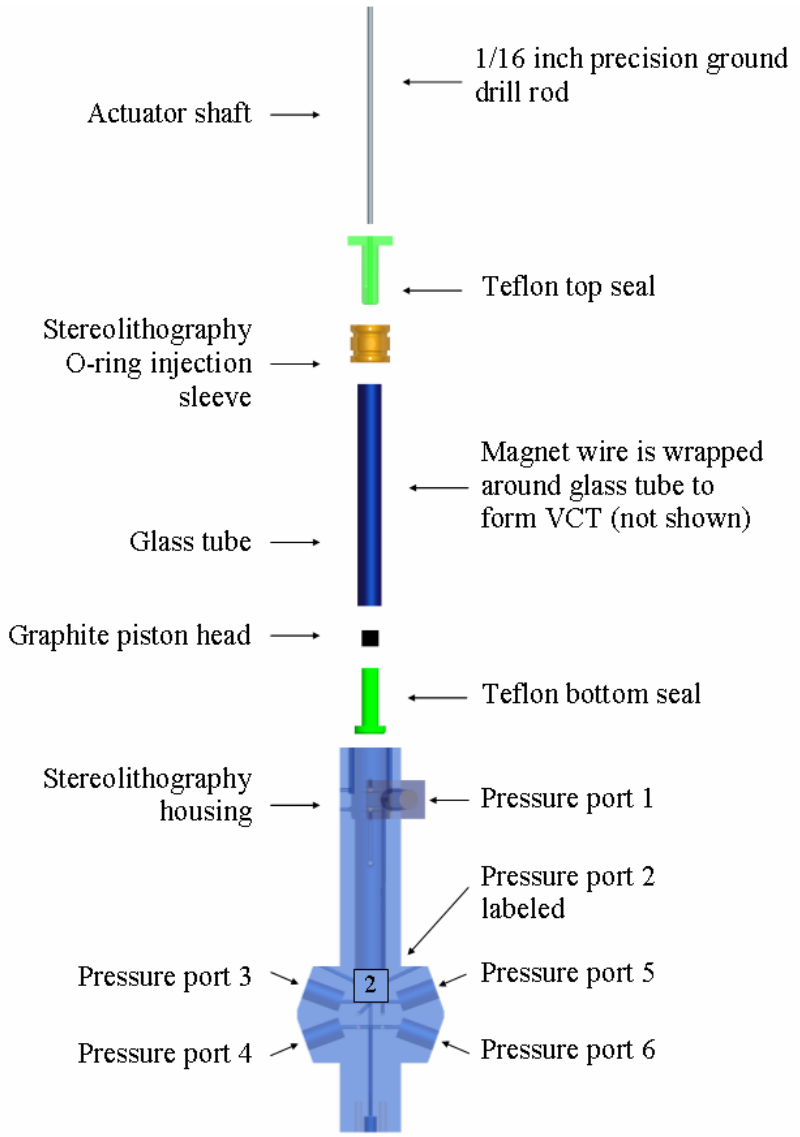

Figure 4.2: Exploded CAD model of Fluidic Actuator (Valves Not Shown)

However, there is a gap in the radial direction between the glass cylinder and the SLA housing when the glass cylinder is inserted into the SLA housing. An SLA O-ring injection sleeve, shown in Figure , slides over the glass cylinder and is used to fill the gap between the glass cylinder and the SLA housing in order to create a sealed channel through which fluid can flow into and out of the upper cylinder cavity. The O-ring injection sleeve has a hole in its side that is approximately 4 mm in diameter which is aligned with the 2 mm diameter hole in the glass cylinder. These holes are aligned with the channel which connects the common port of V1 to the upper cylinder cavity. Therefore, when the O-ring injection sleeve is installed, fluid is allowed to move from V1, through the channel in the SLA housing, through the sealed O-ring injection sleeve, through the hole in the glass cylinder, and into the upper cavity of the cylinder. The Teflon top seal bolts into the top of the SLA housing to further secure the assembly into the SLA housing. As seen in Figure , pressure ports 3 and 4 are symmetric to ports 5 and

6 about the centerline of the SLA housing, pressure port 2 is centered between ports 3 and 5 and is orthogonal to the axis of motion of the piston, and pressure port 1 is located towards the top of the piston where the working fluid enters and exits the upper cavity of the cylinder.

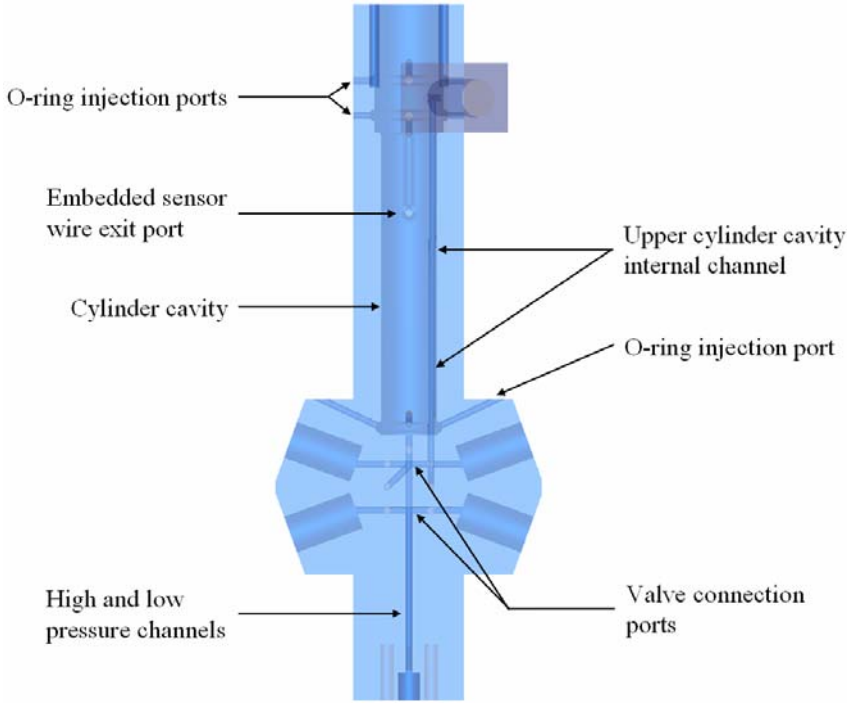

Figure 2.3: CAD Model of stereolithographed actuator housing

Figure 2 shows a CAD model of the stereolithographed actuator housing. This fabrication approach enables the construction of the actuator housing and the intricate internal channels and is particularly useful for prototyping purposes. The disadvantages of using SLA are that it is difficult to maintain tight tolerances, and it is not as dimensionally stable as metal or plastic. Therefore, segments of the actuator housing which require high tolerance, such as the diameter of the cylinder, cavity are reamed to ensure a tight fit.

The material selections of graphite and glass for the respective piston head and cylinder are preferable because of their mutually low static and kinetic coefficients of friction as well as for their availability. Drill rod is used for the steel shaft because of its high dimensional stability and surface finish.

One area of focus is the design of the seal that prevents fluid from leaking out around the reciprocating piston at the top of the actuator. Originally, a double lipped O-ring that fit tightly around the steel shaft was used. Although this method of sealing the reciprocating shaft was effective in preventing the leakage of fluid, it exerted excessive friction force on the steel actuator shaft. The solution was to fabricate a Teflon seal to minimize the static and kinetic coefficients of friction with the steel shaft. This sealing approach

allows the piston to be driven with lower pressures than with the previously mentioned O-ring design. A Teflon seal is also used to prevent fluid from leaking out of the bottom of the glass cylinder into the SLA housing.

4.2.3 Measurement Techniques

Three pressure transducers are used for the acquisition of the pressure data presented in this work. Two miniature pressure transducers (XPM5 343 and XPM5 344, GS Sensors) are used and are referenced hereafter as T1 and T2 while the third transducer (PMP 4010, Druck) is referenced hereafter as T3. All of the above pressure transducers have ranges of 0-30 psi and resolutions of 0.015 psi. Sensors T1 and T2 have accuracies of 0.25% full scale, and T3 has an accuracy of 0.08% full scale. As shown in Figure 4.1 there are seven numbered pressure ports which are located on the high and low-pressure sides of each valve, the channels leading into both the upper and lower cavities of the cylinder, and the supply line to the pressurized reservoir. Sensors T1 and T2 are used to monitor the pressures in the actuator (pressure port 1-6) while T3 is used to measure the pressure of the pressurized reservoir (pressure port 7).

4.2.4 Pressure Measurements

Ports 3 and 5 in Figure 4.1 are connected to the high pressure channels of the actuator and ports 4 and 6 are connected to low-pressure channels. However, ports 1 and 2 are connected to either high or low-pressure depending on the actuation direction of the piston. Air that is trapped in the pressure ports when the pressure transducers are removed is purged by slight pressurization of the system; the working fluid is collected and funneled back into a return tank. The fluidic actuator is constructed of translucent SLA which allows for a visual inspection of this method.

Table 4.1 details 5 combinations of T1 and T2 measurements that are needed to calculate the pressure difference across each of the system components.

Table 4.1: *Transducer Case Numbering Scheme*

Case	Ports		Pressure Drop Across	Piston Motion
1	1	2	Piston	Up and Down
2	1	5	V1/ HP Res to FA	Down
3	1	6	V1/ FA to LP Res	Up
4	2	3	V2/ HP Res to FA	Up
5	2	4	V2/ FA to LP Res	Down

The pressure difference across the piston as it moves either up or down is measured across ports 1 and 2 (case 1 Table 4.1). The pressure difference across V1 and its associated channels as the piston is moving down as well as the pressure difference from the NC port of V1 to the high-pressure reservoir, along with data from T3, are measured

across ports 1 and 5 (case 2 Table 4.1). The pressure difference across V1 and its associated channels as the piston is moving up as well as the pressure difference from the NO port of V1 to the low pressure reservoir are measured across ports 1 and 6 (case 3 Table 4.1). The pressure difference across V2 and its associated channels as the piston moves up is measured across ports 2 and 3 and, along with data from T3, provides the pressure difference from the high pressure reservoir to the NC port of V2 (case 4 Table 4.1). The pressure difference across V2 as the piston is moving down as well as the pressure difference from the NO port of V2 to the low-pressure reservoir is measured across ports 2 and 4 (case 5 Table 4.1). The pressure data are digitized at 1 KHz by an A/D board (AT-MIO-16-E1) that is controlled by LabView software.

4.2.5 Position Measurements

An optical displacement measurement system (optoNCDT 1605, Micro-Epsilon) was used to verify the position measurements obtained from the variable core transformer (VCT). The optical displacement measurement system functions on the principle of triangulation measurement whereby a laser beam is focused on the target and the diffuse reflection is focused on a position sensor as shown in Figure 4.4. The optical measurement system outputs a voltage that is linearly proportional to the measured distance between the measurement device and the target for the measurable range of the device (100 mm). Calibration data for the optical displacement measurement system and the VCT are shown below.

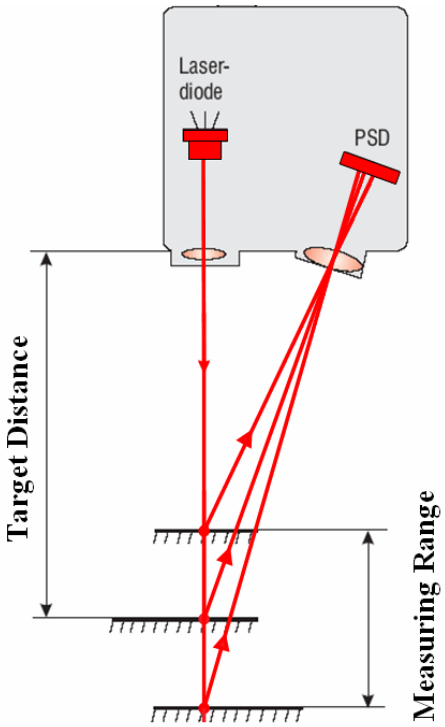

Figure 4.4: Optical Displacement Measurement System Operation Diagram (Courtesy of Micro-Epsilon)

An optical measurement pad is attached to the top of the piston rod to provide a measuring surface for the optical displacement measurement system. Position data was recorded from the optical displacement measurement system and the VCT for all of the cases that are described below and is presented below along with a description of the design and operation of the VCT. The VCT is constructed by wrapping magnet wire around the glass cylinder, which is inserted into the actuator.

In order to resolve the forces that are exerted on the piston it was necessary to independently measure the friction force between the steel actuator shaft and the Teflon top seal. The friction force test stand, shown in Figure, was constructed to facilitate the isolation of the friction force acting on the shaft as a result of the Teflon top seal.

When the Teflon top seal is attached to the actuator it is inserted into the glass cylinder as described below. The diameter of the Teflon top seal is approximately 0.03 mm larger than the inside diameter of the glass cylinder. Therefore, when the Teflon top seal is inserted into the glass cylinder a compressive force is exerted on the Teflon top seal by the glass cylinder. This compressive force acts on the steel actuator shaft which is inserted into a hole in the center of the Teflon top seal. The O-ring injection sleeve is pressed onto the glass tube, which adds to the compressive force acting on the steel actuator shaft.

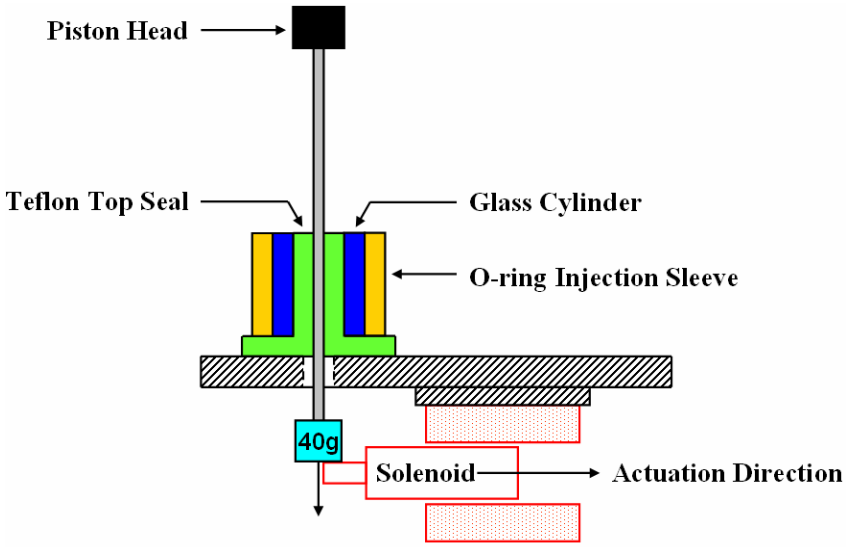

Figure 4.5: Friction Force Test Stand

The friction force test stand, shown in Figure, consists of a rigid base, a solenoid core and associated solenoid coil, a 40 gram mass, steel actuator shaft, Teflon top seal, glass cylinder, O-ring injection sleeve, and the piston head. The solenoid shown in Figure is actuated with a TTL signal from the data acquisition computer and the interface of the Teflon top seal and the steel actuator shaft is kept well lubricated with the working fluid. When the solenoid coil is energized the solenoid core moves to the right and the 40 gram mass pulls the steel shaft down through the Teflon top seal. A 40 gram mass was used

because it was experimentally determined to be large enough to immediately move the actuator shaft upon excitation of the solenoid, but no so large that damage was caused to the piston head upon termination of motion. In order to accurately measure the friction force exerted on the steel actuator shaft by the Teflon top seal a portion of the glass tube and O-ring injection sleeve were included in the friction force test stand as seen in Figure.

The optical displacement measurement system is placed above the piston head and used to sample the position of the piston head at 100 KHz for 0.11 seconds as the piston is pulled downward by the 40 g mass. The position data from this test is used to calculate the friction force acting on the steel actuator shaft and is presented along with the associated friction force calculations in the Findings Section.

4.3 Calibration

The pressure transducers, the optical displacement measurement system, and the variable core transformer (VCT) were calibrated periodically during the course of the measurements as described in this section.

4.3.1 Pressure Calibration

A calibration station was constructed in order to calibrate the three pressure transducers simultaneously using a test gauge and pressure regulator. The test gauge (Q-8638, Omega Engineering Inc) has an accuracy of 0.25% full scale, resolution of 0.2 psi, and a range of – 762 mm Hg to 30 psi. During calibration, pressure data are sampled at 1 KHz for 10 seconds from T1, T2, and T3 in 5 psi increments and recorded. The calibration curves for the three pressure transducers are shown in Figure 4.. Calibration is conducted by changing the supply pressure until the test gauge reads a specified value (0-25 psi in 5 psi increments) and measuring the respective output voltages of T1, T2, and T3. The values shown in Figure are obtained by calculating the difference between the pressure read on the test gauge and the pressure measured from the three transducers. These differences are the bias errors of the transducers.

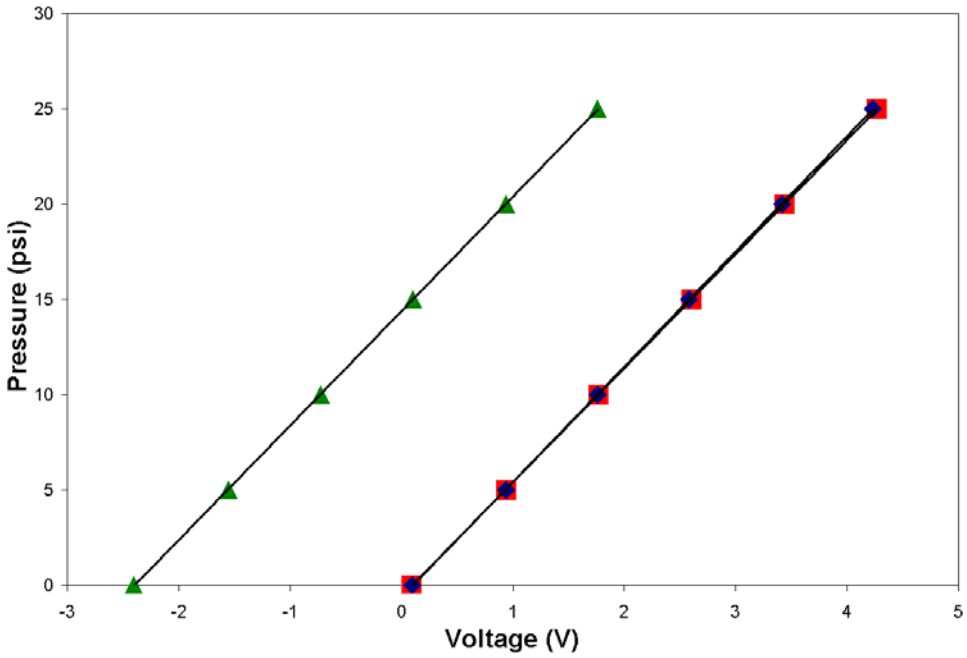

Figure 4.6: Transducer Calibration Curves for T1(■), T2(♦), and T3(▲)

The calibration curves for T1, T2, and T3 are shown in Equations 1-3 respectively

$$T1: \quad y = 6.02x - 0.43 \qquad (1)$$

$$R^2 = 1$$

$$T2: \quad y = 6.05x - 0.79 \qquad (2)$$

$$R^2 = 1$$

$$T3: \quad y = 6.01x + 14.27 \qquad (3)$$

$$R^2 = 1$$

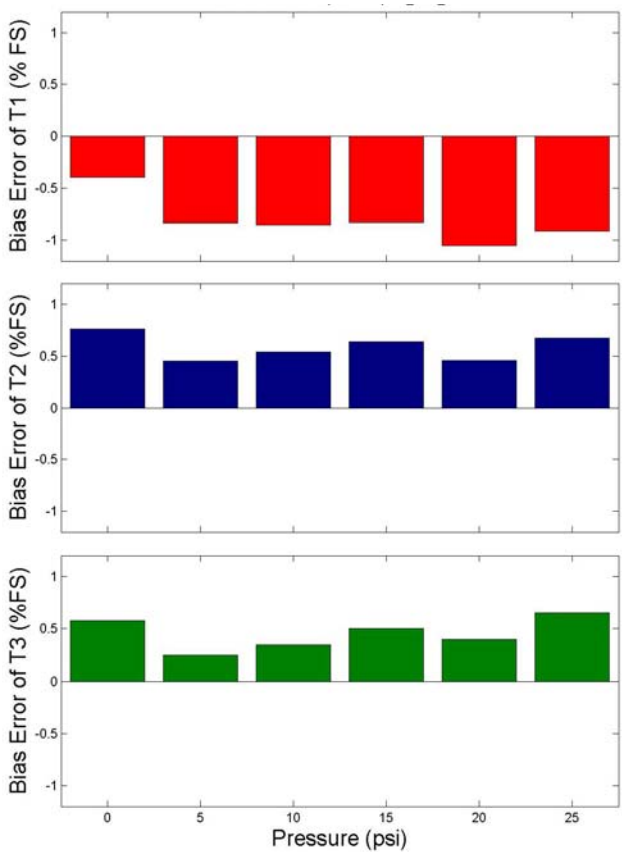

Figure 4.7: Bias Error of T1 (Top), T2 (Middle), and T3 (Bottom)

4.3.2 Position Calibration

A position calibration station was constructed and is shown in Figure 4.8. The position calibration station was constructed to calibrate the optical displacement measurement system and the variable core transformer concomitantly. The calibration station consists of an optical stand, the optical displacement measurement system (0.008 mm resolution), the actuator, and a traverse outfitted with a micrometer (63P 50305, The L. Sarrett Co). The micrometer barrel has a nominal range of 50 mm and a resolution of 0.0254 mm. The optical displacement measurement system is positioned on the optical stand so that the incident beam is centered on the top of the measuring pad of the actuator and the range of motion of the piston (30 mm) is within the measurable range of the optical displacement measurement system (100 mm) and the movable range of the traverse (50 mm).

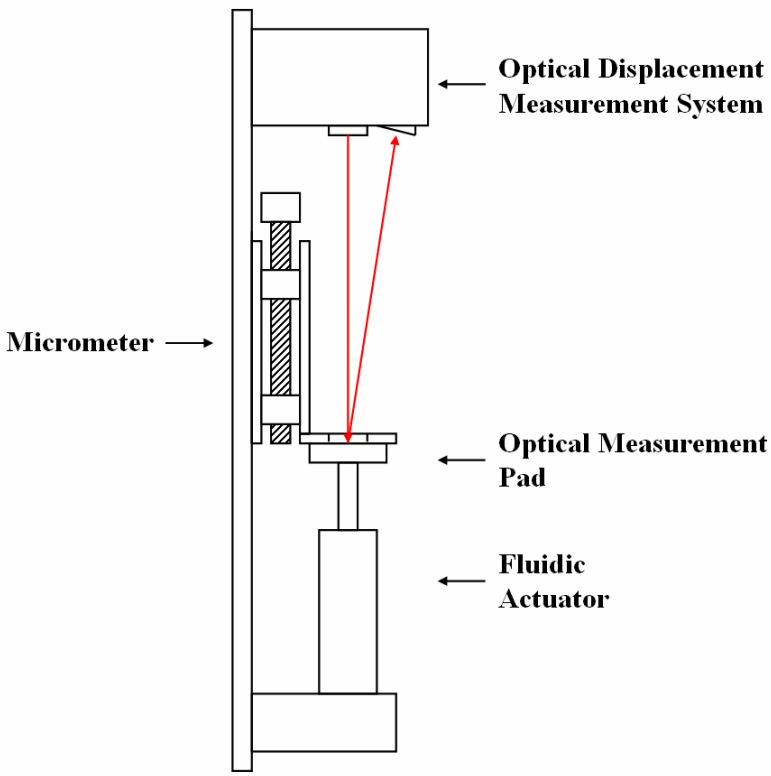

Figure 4.8: Position Calibration Station

The calibration curves for the optical displacement measurement system and the variable core transformer are obtained by moving the piston to its fully retracted position and setting that location as reference. The traverse is then moved through the range of piston motion in 0.635 mm (one turn of the micrometer) increments. The output of the optical displacement measurement system and the variable core transformer are sampled at 1 KHz for 10 seconds at each location and recorded. The calibration curves for the optical displacement measurement system and the variable core transformer as obtained from the position calibration station are shown in Figure .

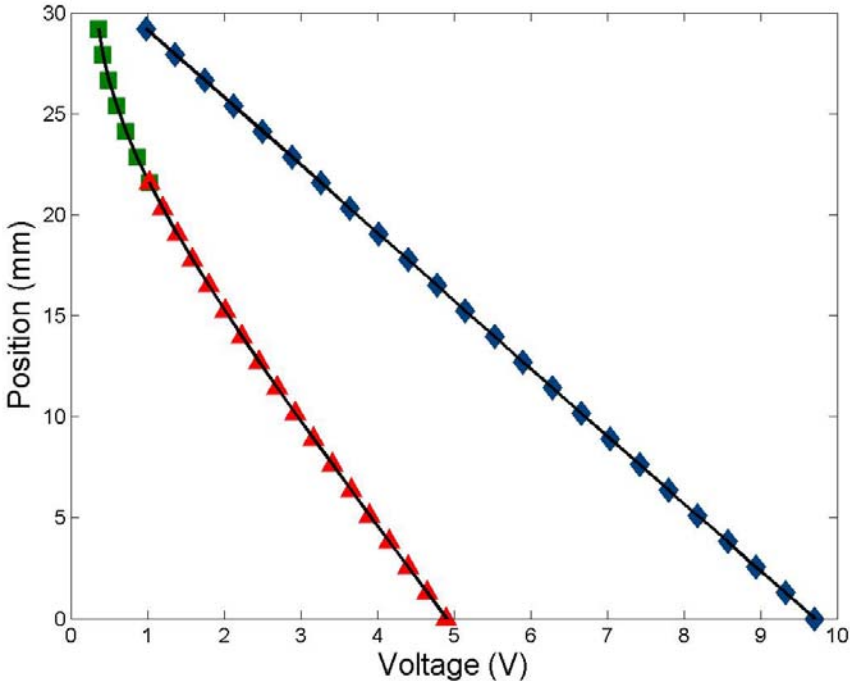

Figure 4.9: Laser(♦) and variable core transformer(■, ▲) curves

Least squares polynomial fits are shown in Figure for the calibrated optical displacement measurement system and the variable core transformer data. The calibration curves for the variable core transformer are Equations 1 and 2 and the calibration curve for the optical displacement measurement system is Equation 3. The respective goodness of fit parameters are also given.

$$y = -19.652x3 + 50.192x2 - 50.53x + 41.787 \quad (4)$$

$$R^2 = 1$$

$$y = -0.0711x3 + 0.8426x2 - 8.4182x + 29.351 \quad (5)$$

$$R^2 = 1$$

$$y = -3.351x + 32.505 \quad (6)$$

$$R^2 = 1$$

Figure 3 shows the position measured from the micrometer along with the calibrated optical displacement measurement system data and the calibrated variable core transformer data as obtained from the Equations 4-6 respectively.

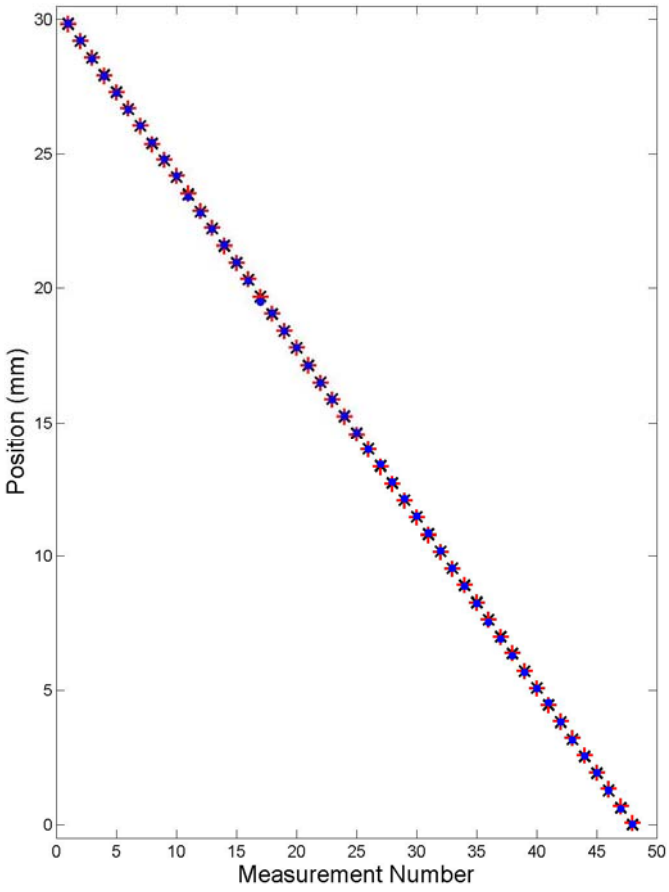

Figure 3: Micrometer Position (×), optical displacement measurement system position (+), variable core transformer Position (•)

The bias errors of the VCT and the optical displacement measurement system are obtained by subtracting the respective calibrated position measurements from the known position of the micrometer (Equation 7) where P_T is the position of the micrometer and P_S is the position measured by either the VCT or the optical displacement measurement system.

$$e_B = P_T - P_S \tag{7}$$

The variation of the bias errors of the optical displacement measurement system and the VCT with piston position are shown in Figure 4. The largest bias error of the VCT is -0.17 mm, which is approximately 0.6 % full scale. While largest bias error measured from the optical displacement measurement system is 0.08 mm, which corresponds to approximately 0.3 % full scale.

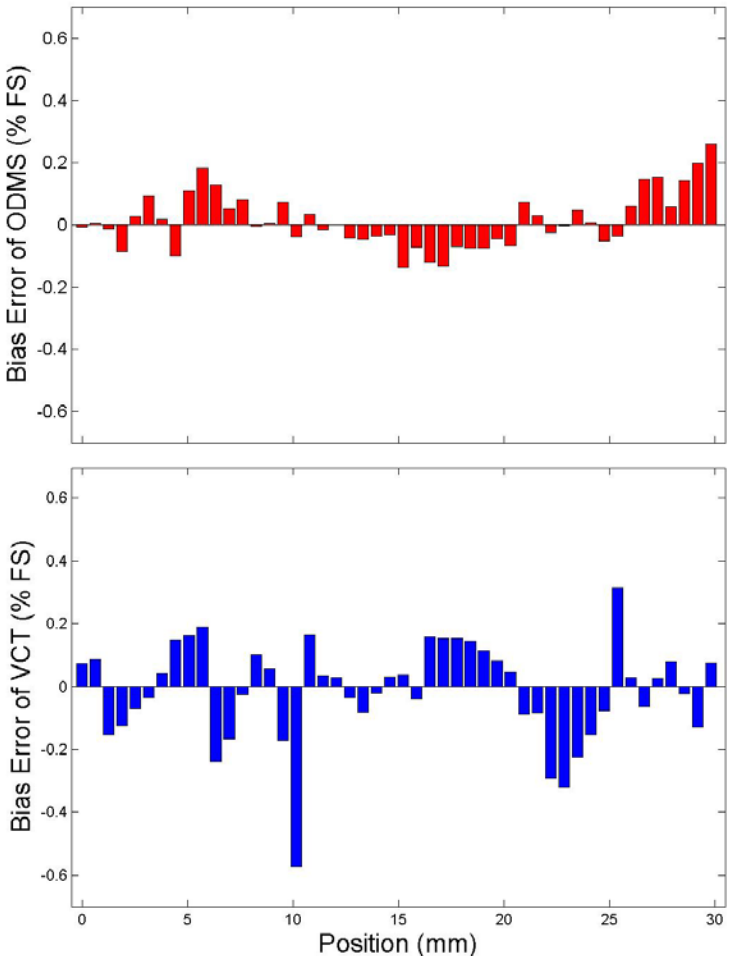

Figure 4: Bias Error of ODMS and VCT

The average bias error of the optical displacement measurement system is 0.014% full scale with a standard deviation of 0.09 % full scale while the average bias error of the variable core transformer is 0.014 % full scale with a standard deviation of 0.16% full scale. The variable core transformer is discussed in more detail below.

4.3.4 DEVELOPMENT of VCT for position measurement

A Variable Core Transformer (VCT) was designed, constructed, and integrated with the fluidic actuator for highly resolved position sensing. This chapter details the design and implementation of the VCT by focusing its principle of operation and practical implementation. As discussed below, the variable core transformer is developed based on a Linear Variable Differential Transformer (LVDT). The present variable core transformer has two overlapping coils where the excitation of the primary coil results in a magnetic field which induces a current in the secondary coil. The voltage induced in the secondary coil is controlled by the ratio of turns of the primary to the secondary coils. A full characterization of the VCT is presented in below, including sensitivity and resolution analysis, repeatability, and drift calculations as a function of piston position.

4.4 Theory of Operation

When an electric current flows through a wire coil a magnetic field is established. The magnetic flux Φ_B through a differential area $d\vec{A}$ in a magnetic field $\vec{B}$ is

$$d\Phi_B = \vec{B} \bullet d\vec{A} = BdA\cos\theta \tag{8}$$

(Young 1996) where θ is the angle between the magnetic field $\vec{B}$ and differential area dA (Figure 5).

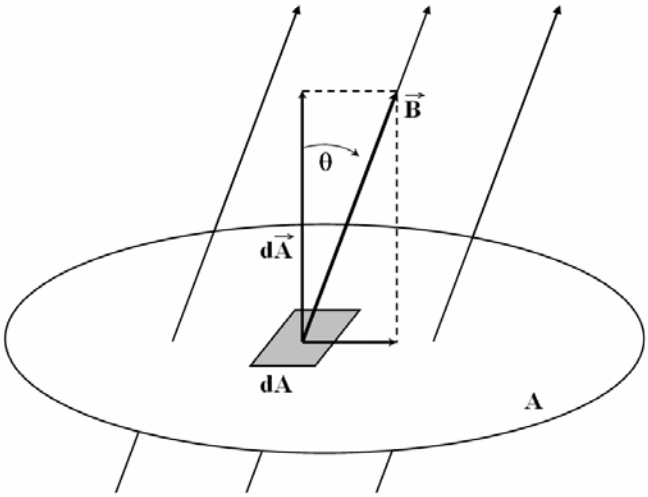

Figure 5: Magnetic Flux Through Differential Area dA

The total magnetic flux through area dA is given by integrating the magnetic flux over area A.

$$\Phi_B = \int \vec{B} \bullet d\vec{A} = \int BdA\cos\theta \tag{9}$$

If the magnetic field is uniform and orthogonal to area A then the magnetic flux through A.

$$\Phi_B = BA \tag{10}$$

Based on Faraday's induction law, if the area A, (Figure 5), is bounded by a conductor, then a changing magnetic flux through A induces an electromotive force through the bounding wire (Rizzoni 2000). One way to increase the induced voltage in the wire is to use a coil of wire (Figure 6) having N turns so that the induced emf, ε, in the coil is

$$\varepsilon = N\frac{d\Phi_B}{dt} \tag{11}$$

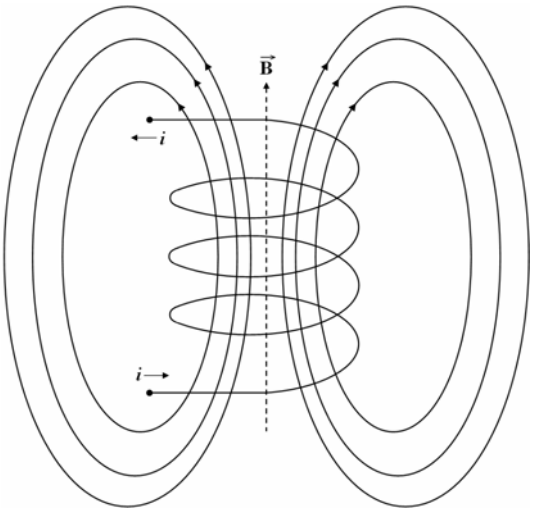

Figure 6.13: Induced emf in Coil

(Young 1996). In the absence of a time varying magnetic flux there is no induced voltage in the coil but an alternating current generates an alternating magnetic flux.

In a transformer excitation of the primary coil with an alternating (AC) voltage, creates a time varying magnetic flux through the magnetic core and induces a current in the secondary coil. The induced voltage in the secondary coil is

$$\varepsilon = \frac{n_2 \mu_0 \mu_r A}{l} \frac{di}{dt} \tag{12}$$

where n_2 is the number of turns in the secondary coil, μ_0 is the permeability of free space, μ_r is the relative permeability of the core, l is the length of the coil, A is the cross sectional area of the core, θ is the angle between the magnetic field B and the cross sectional area, as defined in Figure 5, and i is the current in the primary coil. In Equation 12, it is assumed that the windings of the transformer coils about the magnetic form are sufficiently close so that the induced voltage is not affected by the spacing of the wire on the form (Welsby 1950). Therefore, fixing the length, l, of the transformer and increasing the diameter of the wire used in the secondary coil effectively decreases the number of turns in the secondary coil, and decreases the induced voltage in the secondary coil. Equation 12 also shows that increasing the diameter of the transformer core increases the cross sectional area A and the induced voltage in the secondary coil. The induced voltage in the secondary coil (V_2) is proportional to the excitation voltage of the primary coil (V_1) by the turns ratio of the transformer (N) which is the ratio of the number of turns in the secondary coil to the number of turns in the primary coil.

$$\tilde{V}_2 = N\tilde{V}_1 \tag{13}$$

4.5 System Implementation

A Linear Variable Differential Transformer (LVDT) is a robust position measurement device which works on the principle of magnetic flux coupling. LVDTs consist of an arrangement of primary and secondary coils, inside of which is a movable magnetic core

(Figure 7). The primary and secondary coils are wound such that movement of the magnetic core induces a voltage in the secondary coils which varies linearly with displacement. Attached to the magnetic core is a non-magnetic rod, which is mechanically coupled to the variable of interest for position measurement. Linear variable differential transformers only have one moving part (magnetic core) and are typically designed in a way which isolates the coils from their surroundings, allowing them to function well in hostile environments.

In a Linear Variable Differential Transformer (LVDT) the voltage from a primary coil induces a voltage into the secondary coils as described below. Figure 7 shows the coil arrangement of a typical LVDT where positive and negative displacements of the core are measured with respect to the core's center position.

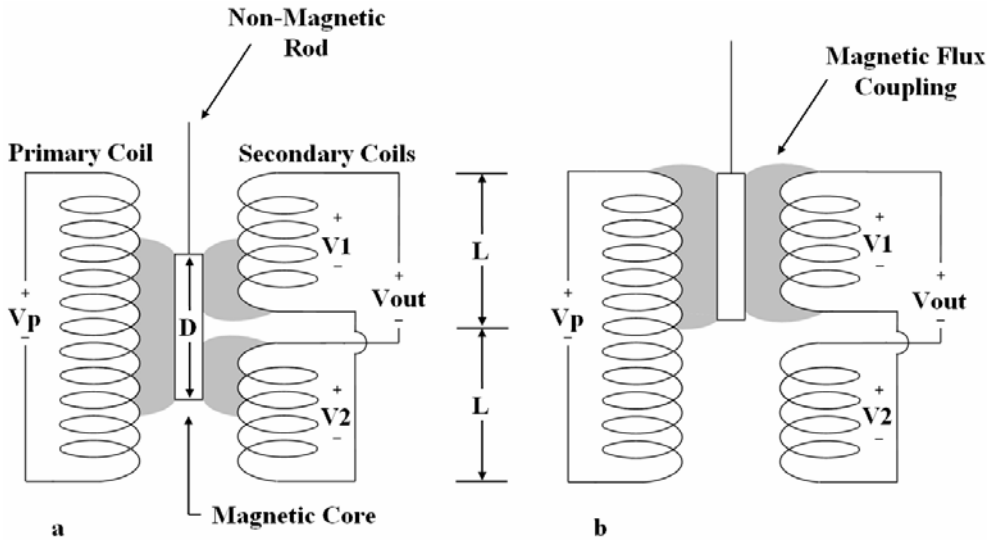

Figure 7: LVDT Schematic Showing Flux Coupling

The time varying magnetic field created by the excitation of the primary coil is greater in the region surrounding the magnetic core than it is in regions which are not in close proximity to the movable magnetic core. Assuming that the secondary coils are identical, when the magnetic core is in its center position, as shown in Figure 7a, the changing magnetic flux of the primary coil engages the same number of turns in the upper secondary coil as it does in the lower secondary coil, which induces voltages of the same magnitude in the upper (V_1) and lower (V_2) secondary coils. However, the coils are connected such that the output voltage, V_{out}, is the subtraction of V_2 from V_1, which gives an output voltage of zero. If the magnetic core is moved upward with respect to the center position by moving the non-magnetic coupling rod, as shown in Figure 7b, then the magnetic flux from the primary coil engages more windings on the upper secondary coil and the induced voltage (V_1) in the upper secondary coil increases with "positive" core displacement. Similarly, V_2 increases with "negative" core displacement.

As shown in Figure 7, the LVDT output is zero when the magnetic core is in the center of its range of motion only if the "upper" and "lower" secondary coils are identical. Once the core is in a position where the magnetic flux is coupled completely with one of the secondary coils (Figure 7b), any additional motion of the core does not yield a further change in voltage because the same number of windings are being added as are being subtracted. This means that for a typical LVDT the measurable range of the sensor is limited by the length of the core and the distance between the upper and lower secondary coils. The upper bound for the measurable range of an LVDT is limited by the geometry of the device. Also labeled in Figure 7 are the lengths of the upper and lower coils (L) as well as the length of the magnetic core (D). The length of the magnetic core (D) is necessarily larger than L so that the core is always engaging both of the secondary coils. Therefore, the upper bound of the motion of the core is slightly less than 2D. For many applications the size of the sensor is inconsequential, however, for small systems where space is critical, traditional LVDTs may be harder to implement.

The Variable Core Transformer (VCT) operates on the same magnetic flux coupling principle as the LVDT, but has a different geometry which is more suitable for use in compact applications such as the fluidic actuator. The design of the VCT takes advantage of the fact that the sensor does not make physical contact with the piston and therefore, does not contribute additional friction forces to the piston. Because there is no mechanical interaction between the VCT and the piston rod there is no wear on the VCT, which gives the VCT long service life.

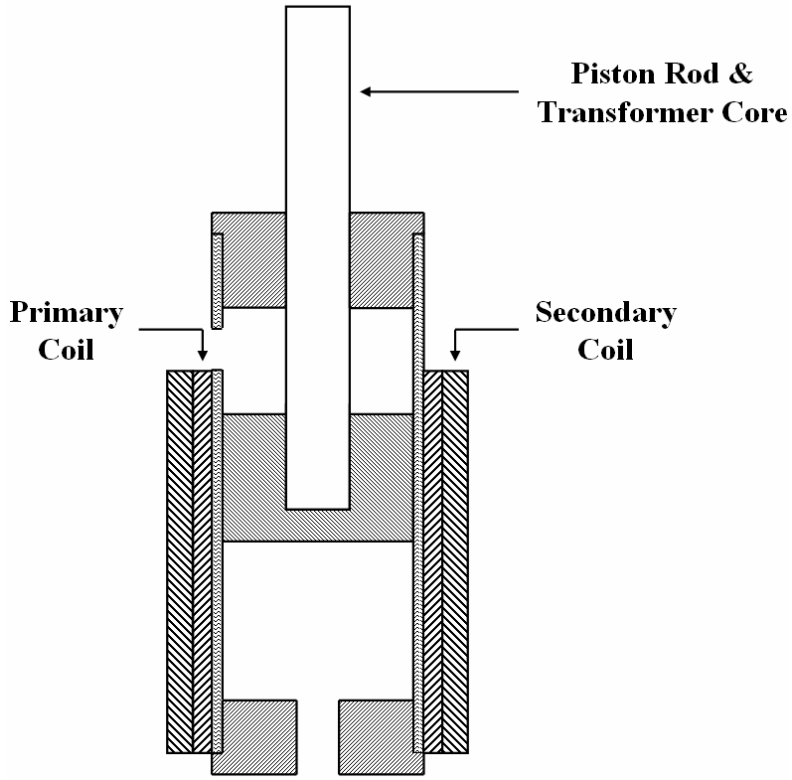

Figure 4.15: Variable Core Transformer Implementation

Figure 4.15 shows the piston, cylinder, Teflon seals, and the windings needed to make the VCT operate as a piston and a position measurement system. The VCT uses overlapping primary and secondary coils. With this design, the induced voltage in the secondary coil is continuously increasing as the transformer core, or piston rod, moves into the cylinder cavity. The salient characteristics of the steel core are its availability, surface characteristics, and mechanical properties. Although a ferromagnetic rod could provide a stronger magnetic flux, and therefore, a larger induced voltage in the secondary coil, the mechanical properties of ferromagnetic materials are inferior compared to those of steel.

The output of the VCT is an amplitude modulated AC voltage. In order to obtain a DC voltage which is directly proportional to the position of the core, the output of the VCT must be demodulated.

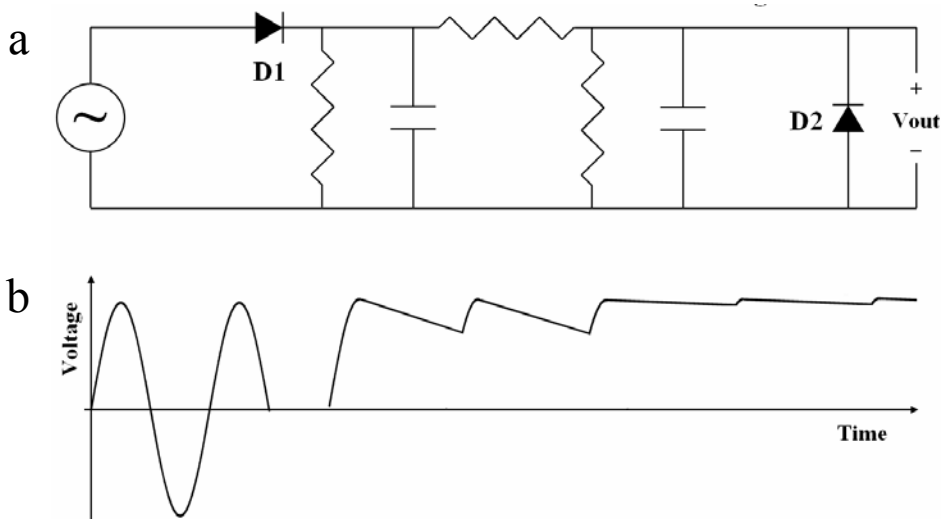

Figure 4.8: Half Wave Rectifier Bridge with Filter Network (a) and associated output waveform (b)

Figure 4.8a shows a half wave bridge rectifier with a filter network which is used for the rectification of the induced AC voltage in the VCT. The voltage source is the induced voltage in the secondary coil of the VCT and the output voltage (Figure 4.8b) is the rectified DC signal which is sampled by a 12 bit data acquisition board. Diode D2 is not needed in the rectification of the AC input signal, but is present to prevent the data acquisition computer from electronically loading the VCT in the event of a hardware failure. The AC voltage measured from the VCT and its transformation to a DC signal are shown in Figure 4.8b. The addition of capacitance reduces the perturbations in the output voltage of the circuit.

In the present configuration, the VCT is constructed by wrapping 34 gauge magnet wire around a nominal 8 mm diameter glass tube, which serves as the cylinder cavity (Figure 4.15). The secondary coil is made with the same wire and is wrapped directly on top of the primary coil. The secondary coil, however, has twice as many turns as the primary, giving a turns ratio of 2 and thus amplifying the output voltage as shown in Equation 13. Due to the compact nature of the fluidic actuator, a greater turns ratio could not be accommodated.

A relatively low (7 KHz) excitation frequency was originally selected in order to minimize high frequency noise in the system. However, higher excitation frequencies yield greater output voltages as shown in Figure 4.9, where the demodulated output voltage range is the voltage difference in the output of the VCT (before amplification) given by moving the piston through its entire range of motion. Demodulated output voltage range also increases as the excitation amplitude is increased.

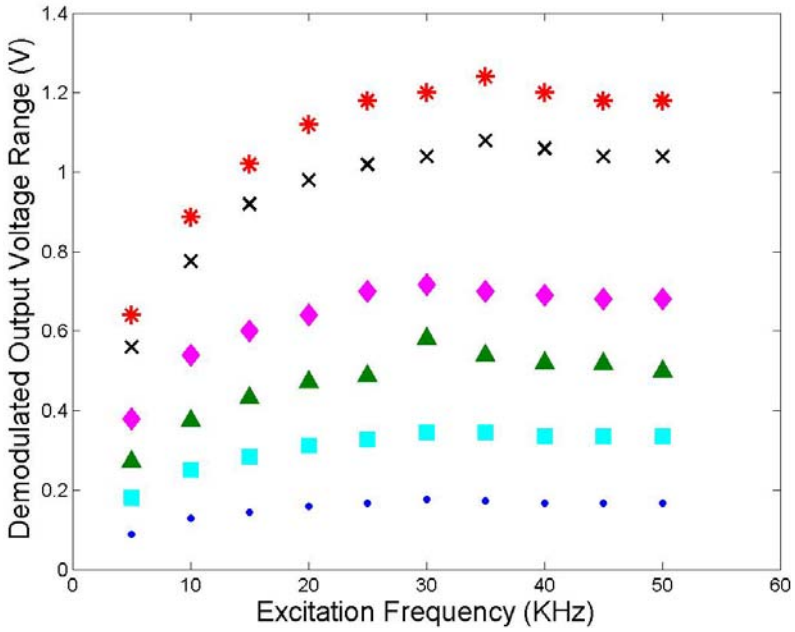

Figure 4.9: *Demodulated output voltage range as a function of excitation frequency for excitation amplitudes of 2.5(•), 5(■),* ***7.5(▲), 10(♦), 15(×), and 17.25(*) Vpp***

Using an excitation voltage of 7 KHz (17.25 Vpp) and amplifying the output signal of the circuit shown in Figure 4.8 using an instrumentation amplifier yields a DC output voltage of 0-5 V as shown by the calibration curves in Figure .

4.5.1 VCT Characterization

Because a small change in the position of the core results in a change in the induced voltage. The resolution of the VCT depends on the ability to resolve this voltage. The limiting factors are the resolution of the data acquisition board, and the electric's noise. The sensitivity of the VCT is determined from its calibration curves (Section 4.3.2).

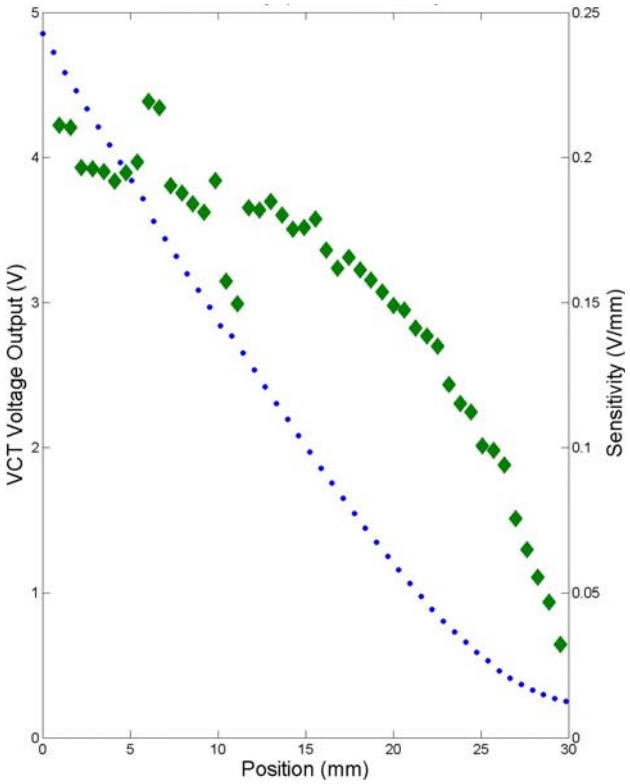

Figure 4.18: *VCT Sensitivity (♦) and VCT Voltage*

Figure 4.18 shows the output voltage and corresponding sensitivity of the VCT obtained using the calibration technique described above. These data show that the sensitivity of the VCT decreases as the piston moves up. At the top of the range of motion (30 mm) the length of the primary coil which is engaging the magnetic core of the VCT is smaller. Given that the resolution of the data acquisition board is 0.24 mV the theoretical resolution of the VCT is nominally 0.008 mm. However, the actual resolution of the VCT is limited by the noise on the output signal, which can be quantified by the standard deviation of the measured piston position at different locations throughout its range of motion. The variation of the standard deviations, or resolution, of the piston position (based on 10,000 samples of the variable core transformer and the optical displacement measurement system) as a function of piston position is shown in Figure 4.19.

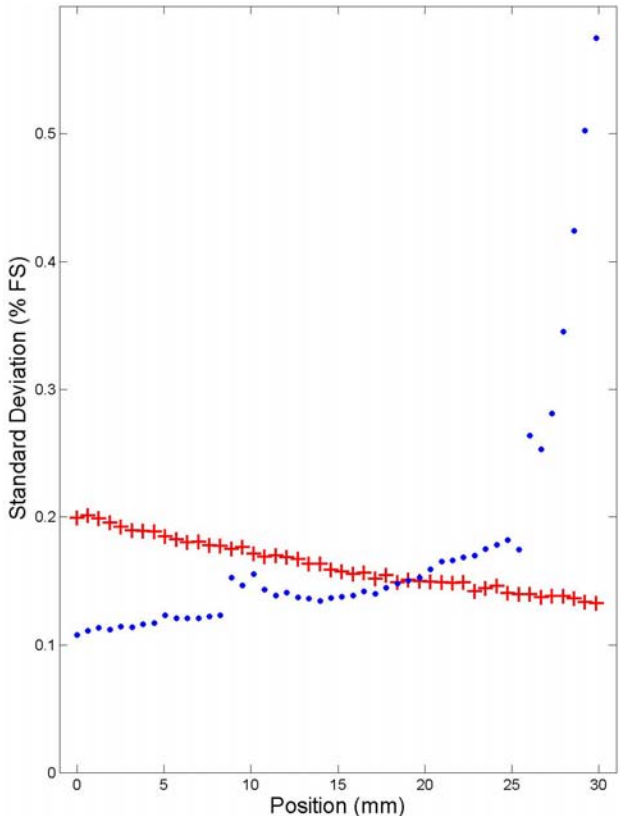

Figure 4.19: *Standard Deviation of Piston Position as Measured by the variable core transformer (•) and optical displacement measurement*

The standard deviation of the VCT signal increases dramatically from approximately 25-30 mm due to end effects. This happens when the piston is fully extended (30 mm) and not while the piston is fully retracted (0 mm) because the Teflon seal in the bottom of the piston extends into the primary and secondary coils approximately 17 mm, which stops the actuator shaft before it reaches the end of the coils of the VCT. While the Teflon top seal extends into the glass cylinder, it only extends into the primary and secondary coils approximately 3 mm. Therefore, when the actuator shaft is in its fully extended position it is only partially immersed in the changing magnetic flux of the primary coil, which produces an induced voltage which has more noise than when the shaft is more fully engaged by the primary coil. Averaging the standard deviation values (Figure 4.19) yields an average resolution of the VCT of 0.17% full scale and an average resolution of the optical displacement measurement system of 0.16% full scale, with respective standard deviations of 0.1% full scale and 0.02% full scale. The repeatability error as a percentage of the Full Scale (FS) of the piston's range of motion is given by (Figliola 2000)

$$e_R = \frac{2 * S_x}{FS} * 100 \tag{14}$$

where S_x is the standard deviation of measured position of the piston. Figure 10 shows the repeatability error of the VCT has an identical trend as the standard deviation of the

VCT. This is because the repeatability error is determined by scaling the standard deviation of the measured position of the piston as shown in Equation 14.

The overall errors of the optical displacement measurement system and the VCT are calculated by the addition of the repeatability error and the bias error as well as the addition of the error due to drift and hysteresis. However, the calculated drift and hysteresis errors of both the optical displacement measurement system and the VCT are less their respective resolutions. Therefore, the overall errors are calculated by combining Equation 7 and Equation 14 as shown in Equation 15 (Figliola 2000).

$$e_{overall} = P_T - P_S + 2S_x \tag{15}$$

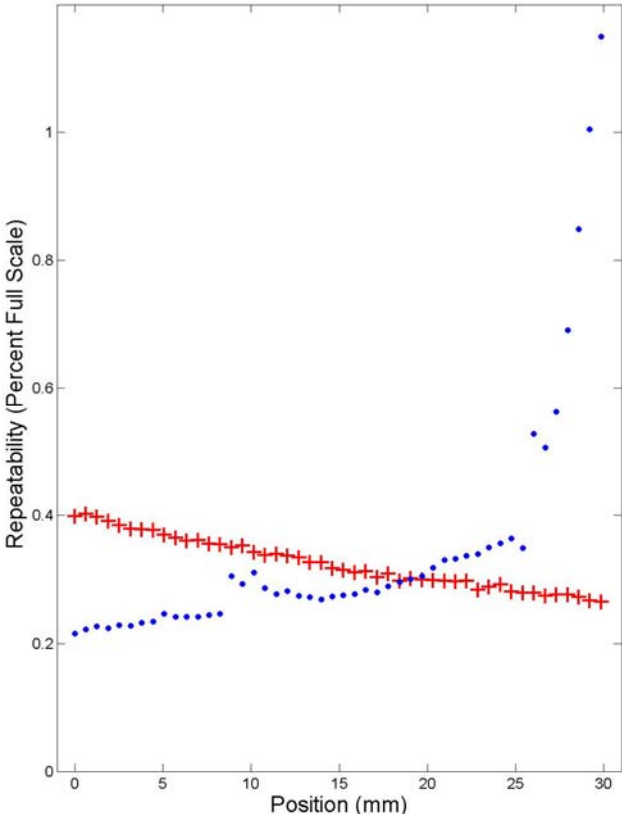

Figure 10: *Repeatability of VCT (•) and optical displacement measurement system (+)*

Figure 4.11 shows the overall errors of the piston position as measured by the optical displacement measurement system and the VCT as a function of piston position.

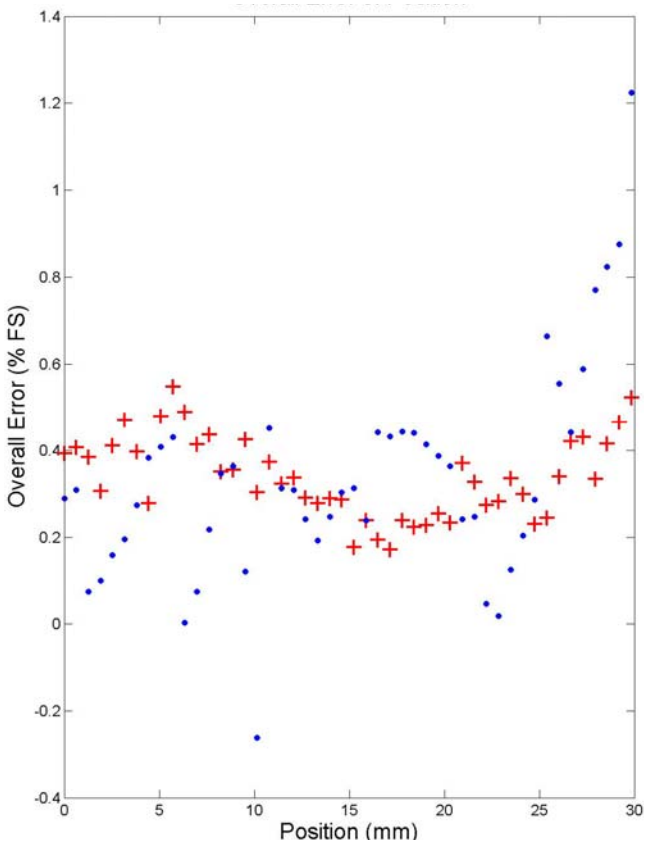

Figure 4.11: *Overall Errors of the VCT (•) and optical displacement measurement system (+)*

The overall error of the VCT is comparable to the optical displacement measurement system for the majority of the range. Even at the edges, the VCT is still accurate to less than 0.4 mm, which is approximately 1.3 % FS. Comparison of Figure 10 and Figure 4 (Garth's MS thesis, chapter 2) shows that when the overall error of the VCT deviates from total error of the optical displacement measurement system (25-30 mm) there is no deviation in the bias error, but there is a variation in the repeatability error. Therefore, the increase of the overall error of the VCT through the approximate range of 25-30 mm is largely attributed to the repeatability error of the VCT.

Section 5
Realization of a Functional Prototype Device (Book)

Dr. Book and Dr. Zhu (whose Ph.D. was completed through this research project in 2005) are working on the practical realization of the Digital Clay concept in a fine pitch and scalable form factor. The prototype is shown in Figure 5.1. The pitch of the provided prototype is 5 mm. Each actuator size is 4mm in outside diameter (OD). The prototype is readily scaled up, i.e. the number of actuators in the array can be increased without change the design scheme.

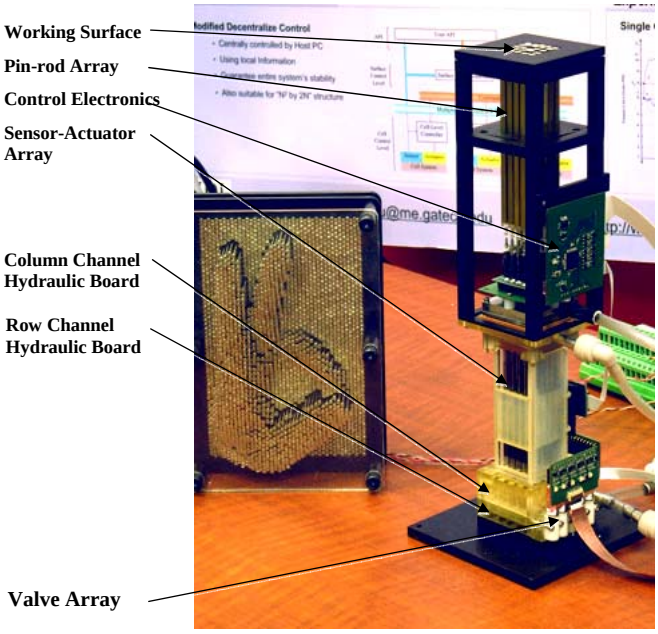

Figure 5.1 Digital Clay 5×5 Prototype

Major activities this year are:

1) Designed and set up the prototype for concept proof, and control methods testing
2) Research on control methods based on the Fluidic Matrix Drive to drive the actuator array with greatly reduced components, i.e. valves and related control resources
3) Remote control the Digital Clay though internet using other haptic devices such as a Phantom®.haptic manipulator

Practical Design and Implementation of the 5x5 Digital Clay Prototype

On the **Mechanical Design** side two major challenges were overcome: the sensor embedded miniature actuator (array), the hydraulic system to drive the actuator array.

Actuator Embedded Displacement Sensor

As shown in figure 5.2, the actuator consists of a precision glass tube, a graphite piston, an electrically conductive hollow cylinder rod, an electrically conductive rod, a resistance film deposited outside the glass tube, and a coaxial cable. The space occupied by the sensor is negligible because it requires only a thin film on the glass tube. This is critical

for a massive actuator array.

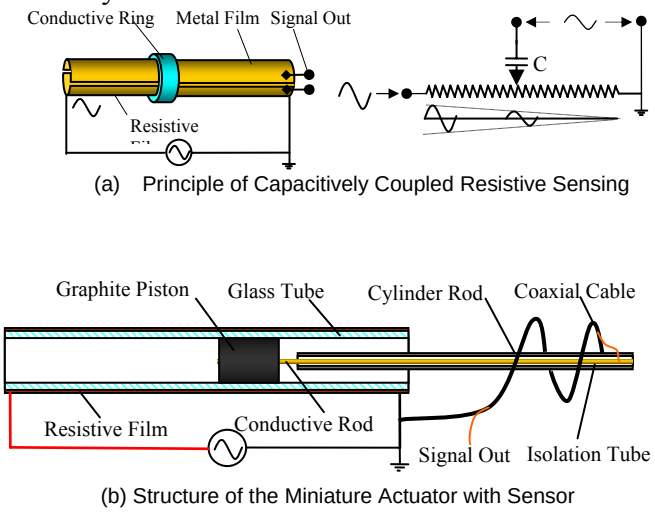

Figure 5.2 Cylinder with Displacement Sensor Embedded

The glass tube and the graphite piston form a cylinder with low friction. To measure the displacement, apply an alternating voltage across the resistance film. The amplitude of the alternating voltage along the film will have a linear distribution as shown in the right of Figure 5.2a. When the piston moves inside the tube, the alternating voltage is coupled by the capacitance between the piston and the resistance film to a accessible output. The coupled voltage is further sent out through the conductive rod and the coaxial cable. The hollow cylinder and the conductive rod form a coaxial structure, which provides shielding for the signal. Comparison of the amplitude of the output signal to the amplitude of the excitation signal yields the position of the piston.

5.1 Actuator Array

A practical realization of the massive actuator array is shown in Figure 5.3. Actuators in the array share a common constant retracting pressure for retraction. If the pressure in the bottom chamber is higher than the retracting pressure, the piston will move up and vise versa.

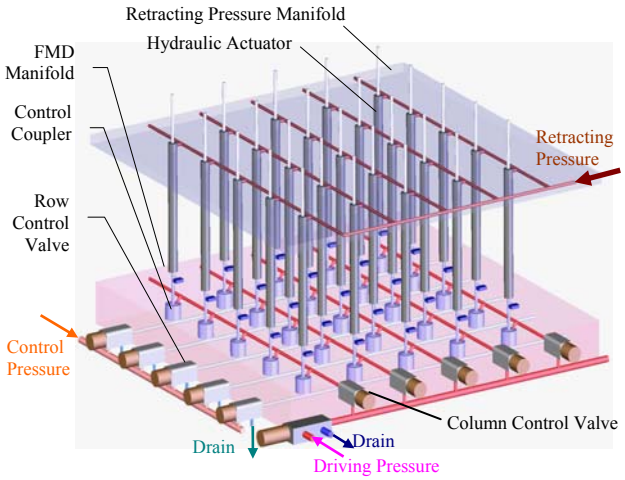

Figure 5.3 Structure and Composition of the Actuator Array

5.2 Fluidic Matrix Drive

To achieve a high-resolution display, a large number of cells are required. As a consequence, the corresponding hardware and computing load could make the system difficult to manufacture and control. To solve the problem, a scheme termed as Fluidic Matrix Drive is proposed. As shown in Figure 5.4, the Fluid Matrix Drive (FMD) is composed of two arrays of control valves and an array of control couplers. The row control valves and the single pressure source selection valve are 3-port/2-way on/off valves. The common ports of these valves are connected to the array of actuators and the other two ports are connected to the high pressure source and the drain. Under this scheme, an M×N actuator array can be independently driven using only (M+N+1) valves in stead of 2×N×M valves.

Each row control valve opens and closes the control couplers in that row, while each control coupler controls the passage from the column control valve to the corresponding actuator. As a consequence, a specific actuator can be activated only when the corresponding row valve and the corresponding column valve are both open.

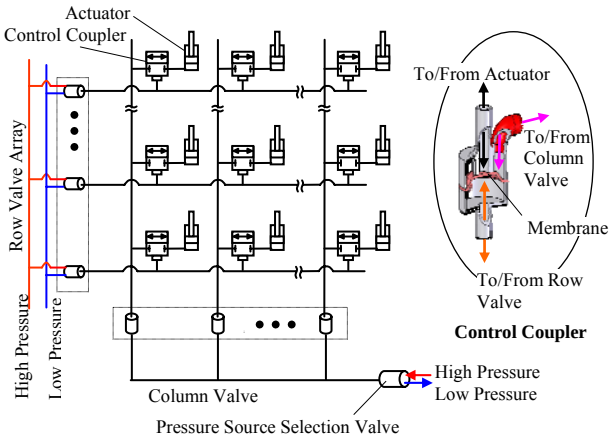

Figure 5.4 Fluidic Matrix Drive Concept and Realization

For the **Control Electronics, a** DSP microprocessor (dsPIC4013) system is used as the onboard low level controller. A PC is used as the high level controller. Control electronics are introduced here briefly. Figure 5.5 shows the general layout. The assembled system is shown in Figure 5.1.

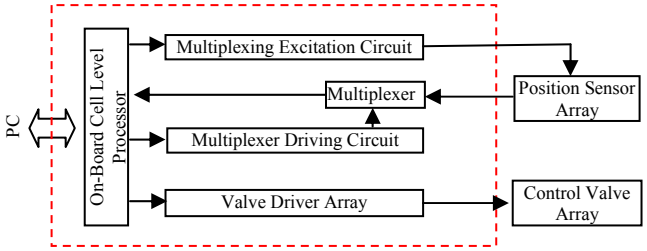

Figure 5.5 On-Board Control Electronics

5.3 Control Methods based on the Fluidic Matrix Drive

5.3.1 Matrix Representation of the Surface Refresh Process

To explain control using the FMD scheme some preliminary concepts are first introduced. An operation Θ is defined here as an operation subject to following rule:

$$\mathrm{A}=\begin{bmatrix} a_1 \\ \vdots \\ a_i \\ \vdots \\ a_n \end{bmatrix};\ \text{and}\ \ \mathrm{B}=\begin{bmatrix} b_1 & \cdots & b_j & \cdots & b_n \end{bmatrix};\qquad \text{Then } \mathrm{A}\Theta\mathrm{B}=\begin{bmatrix} \mathrm{g}(a_1,b_1) & \mathrm{g}(a_1,b_2) & \cdots \\ \mathrm{g}(a_2,b_1) & & \\ \vdots & \ddots & \\ & & \mathrm{g}(a_i,b_j) \\ & & \end{bmatrix}$$

$$where, a_i = f_1(\delta_i); b_j = f_2(\delta_j);\ 0 \le \mathrm{a_i}, \mathrm{b_j} \le 1$$

In the above definition, δ_i is the PWM duty cycle on the row valve array and δ_j is the PWM duty cycle on the column valve array. Functions $f_z(\delta_k)$ *(where z=1, 2)* depend on variables such as pressure drop, discharge coefficient, etc. Function g(x, y) produces the actuator's *speed* as a result of the given choice of the row and column valves' PWM duty cycles. The preferred form of g(x, y) will be determined in future investigations.

For simplicity the current approach fully opens (i.e., $\delta_i = 0\%$, $a_i = 0$) and fully closes (i.e., $\delta_i = 100\ \%$, $a_i = 1$) the row control valves. For column valves, we apply different PWM duty cycles to control the speed of each actuator in the fully enabled rows. Therefore, if x=1, g(x, y) = y and if x=0, g(x, y) = 0. Based on above definition, three control methods are summarized in the following paragraphs.

5.3.2 One-time Refresh Method

Using the one-time refresh method, actuators are controlled to reach their final positions (given by the desired surface matrix) row by row. For example, if the desired final surface matrix is: (unit: cm)

$$\mathrm{C}=\begin{bmatrix} 0 & 1 & 2 & 3 & 4 \\ 0 & 0 & 1 & 2 & 3 \\ 0 & 0 & 0 & 1 & 2 \\ 0 & 0 & 0 & 0 & 1 \\ 0 & 0 & 0 & 0 & 0 \end{bmatrix}$$

Assume the maximum speed of current actuator is 5 cm/sec; refresh settling time (for valves to stably open and close) is 0.05 sec. No action is needed for the first row (from bottom to top). The vectors for controlling the valve arrays for the 2nd row refresh are A1 and B1, and the surface matrix is C1.

$$\mathrm{A1}=\begin{bmatrix} 0 & 0 & 0 & 1 & 0 \end{bmatrix}';\quad \mathrm{B1}=\begin{bmatrix} 0 & 0 & 0 & 0 & 1 \end{bmatrix};$$

$$\mathrm{C1}=\mathrm{A1}\Theta\mathrm{B1}*t_1=\begin{bmatrix} 0 & 0 & 0 & 0 & 0 \\ 0 & 0 & 0 & 0 & 0 \\ 0 & 0 & 0 & 0 & 0 \\ 0 & 0 & 0 & 0 & 1 \\ 0 & 0 & 0 & 0 & 0 \end{bmatrix};\ \text{where } t_1 = 0.2\ \text{sec}$$

For 3rd row: $A2 = [0 \quad 0 \quad 1 \quad 0 \quad 0]'; \quad B2 = [0 \quad 0 \quad 0 \quad 0.5 \quad 1];$

$$C2 = C1 + A2 \Theta B2 * t_2 = \begin{bmatrix} 0 & 0 & 0 & 0 & 0 \\ 0 & 0 & 0 & 0 & 0 \\ 0 & 0 & 0 & 1 & 2 \\ 0 & 0 & 0 & 0 & 1 \\ 0 & 0 & 0 & 0 & 0 \end{bmatrix}; \text{ where } t_2 = 0.4 \sec$$

Similarly for 4th row and 5th row,

$$A3 = [0 \quad 1 \quad 0 \quad 0 \quad 0]; \quad B3 = [0 \quad 0 \quad 1/3 \quad 2/3 \quad 1];$$
$$C3 = C2 + A3 \Theta B3 * t_3, \quad \text{where } t_3 = 0.6 \sec$$
$$A4 = [1 \quad 0 \quad 0 \quad 0 \quad 0]; \quad B4 = [0 \quad 0.25 \quad 0.5 \quad 0.75 \quad 1];$$
$$C4 = C3 + A4 \Theta B4 * t_4, \quad \text{where } t_4 = 0.8 \sec$$

The total time used is $t_1+t_2+t_3+t_4+4\times$Settling Time (i.e., 0.05) = 2.2 sec. The one-time refresh method is the simplest surface refresh method, but shows an obviously discontinuous movement of the pin-rods. This may be undesirable for a user interface.

5.3.3 Gradual Refresh Method

A solution to make the surface refresh smoother is to gradually achieve the final surface through several intermediate surfaces. Take the same desired surface in section B as an example. By dividing the final surface matrix into 4 intermediate surfaces which may be solved as follows:

$$\begin{bmatrix} 0 & 0 & 0 & 0 & 0 \\ 0 & 0 & 0 & 0 & 0 \\ 0 & 0 & 0 & 0 & 0 \\ 0 & 0 & 0 & 0 & 0 \\ 0 & 0 & 0 & 0 & 0 \end{bmatrix} \Rightarrow \begin{bmatrix} 0 & 1/4 & 1/2 & 3/4 & 1 \\ 0 & 0 & 1/4 & 1/2 & 3/4 \\ 0 & 0 & 0 & 1/4 & 1/2 \\ 0 & 0 & 0 & 0 & 1/4 \\ 0 & 0 & 0 & 0 & 0 \end{bmatrix} \Rightarrow \begin{bmatrix} 0 & 1/2 & 1 & 3/2 & 2 \\ 0 & 0 & 1/2 & 1 & 3/2 \\ 0 & 0 & 0 & 1/2 & 1 \\ 0 & 0 & 0 & 0 & 1/2 \\ 0 & 0 & 0 & 0 & 0 \end{bmatrix} \Rightarrow \begin{bmatrix} 0 & 3/4 & 3/2 & 9/4 & 3 \\ 0 & 0 & 3/4 & 3/2 & 9/4 \\ 0 & 0 & 0 & 3/4 & 3/2 \\ 0 & 0 & 0 & 0 & 3/4 \\ 0 & 0 & 0 & 0 & 0 \end{bmatrix} \Rightarrow \begin{bmatrix} 0 & 1 & 2 & 3 & 4 \\ 0 & 0 & 1 & 2 & 3 \\ 0 & 0 & 0 & 1 & 2 \\ 0 & 0 & 0 & 0 & 1 \\ 0 & 0 & 0 & 0 & 0 \end{bmatrix}$$

The time used to realize each intermediate surfaces using one-time refresh method can be found as: 0.7 sec (max. speed is 5 cm/sec). Therefore the total time for the surface generation is 2.8 sec. The more intermediate surfaces are used, the smoother the surface generation process is, but the longer time it takes. The extra time is spent on the refresh settling period (for valves to stably open and close). For the actuator array constructed in this work, the refresh settling time is around 50~100 ms.

5.3.4 Approximation Gradual Refresh Method Concept

The one-time refresh method and gradual refresh method are both processed one row after another. To make the surface refresh more efficient, investigation is currently on the possibility of actuating multiple rows simultaneously. It is called approximation gradual refresh method because the intermediate surfaces used in this method usually are not proportional to the final surface, but the superposition of these intermediate surfaces yields the final surface. By this approach, the total refresh time can be reduced and a smoothly changing surface can be achieved.

5.4 High Level Control

The high level control is realized using Real Time Linux – RTLinux. Multi-threaded programming enables each module of the control system to be running almost simultaneously. Furthermore, control modules can be later realized in separate micro controllers instead of one computer. The structure of the control system currently implemented for Digital Clay is shown in Figure 5.6.

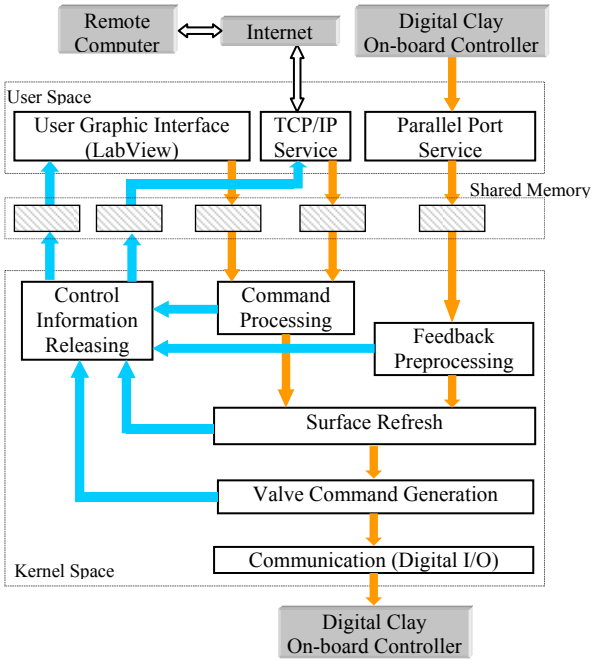

Figure 5.6 General Control Structure of Digital Clay

5.4.1 Information Structure

The information transferred between modules is very simple. At the current stage, all information is in the form of a matrix with each element representing the elevation of the corresponding actuator. This matrix is called the surface matrix.

5.4.2 Surface Refresh Module

For simplicity, the surface control introduced here is based on the one-time surface refresh method described before. This module takes and compares the processed desired surface matrix with the current feedback surface matrix, and gives out the desired speed for each actuator to the Valve Command Generation module. The Valve Command Generation module calculates the desired PWM duty cycle for each actuator based on the input from the Surface Refresh module.

The surface refresh is processed row by row. The following pseudo-code illustrates how the surface refresh module works. Assume the desired surface matrix is A and the current feedback surface matrix is B. Current index of the row being processed is k. The speed surface matrix is C, with each element representing the speed of corresponding actuator.

```
enable the k-th row;
do
{    for (column = 1 to number of columns)    {
       if (B(k, column) < A(k, column))
              C(k, column) = - function(B(k, column), A(k, column));
       elseif (B(k, column) > A(k, column))
              C(k, column) = function(B(k, column), A(k, column));
       else
              C(k, column) =0;
     }
} while (C(k, : ) > lower speed threshold )
disable the k-th row;
```

In the above program, function() is used to determine the speed required. It has been implemented most successfully as a proportional position feedback loop. The surface refresh module runs repeatedly from the first row to the last row and back to first row again. Whenever a new value of C(k, column) is calculated, it is sent to the valve command generation module. Moreover, when any actuator in the enabled row is not in position (i.e., the calculated speed is too large), the surface refresh module will not switch to the next row. On the other hand, if the actuators in that row are all in position, the surface refresh module will do nothing but switch to the next row.

Command Processing Module

The command processing module can take the desired surface matrix from either the user graphic interface or a TCP/IP service program, depending on which one comes first. If using gradual surface refresh method, the desired surface matrix is further divided into several intermediate surface matrices and then sent to the Surface Refresh Module.

Communication through Internet

Currently, a server computer is used for several client devices (including the computer controlling the Digital Clay) to communicate with each other. Each client device will search for the IP address of the server (which is fixed) first. Once the IP address is found, client computers then establish connections with the server. The information format between the server and client are the same as presented before – desired surface matrices. At this time, if two or more clients want to command the desired surface (e.g., one Digital Clay device sends out a surface matrix different than another Digital Clay device), then the server will average two desired matrices and send the averaged surface matrix to these two Digital Clays. In this way, the two users can feel the conflict between themselves. In the future, more information matrices such as material property matrix, desired speed matrix will be implemented as well. At the current stage, only one Digital Clay prototype is available. Tests are conducted between a haptic manipulator (e.g. Phantom®) and the Digital Clay.

Section 6

Paradigms for Direct Human-Shape Interaction (Rossignac)

As part of the Digital Clay project, Dr. Jarek Rossignac and Dr. Chris Shaw, both from the College of Computing, have continued to investigate new paradigm for the Direct Human-Shape Interaction. The investigation comprises the following venues:

- **Bender**: A system for editing shape using a two-handed space warping operator. The guiding metaphor is of a **ribbon** held by the designer at each end. The designer can bend, twist, and move the ribbon and use it to grab portions of the surface and deform them. Currently, in a collaboration with faculty members from the Bio-Medical Engineering department, the team is investigating how Bender may be used as a virtual tool for cardio-vascular surgery planning. The project involved PhD student Ignacio Llamas and Master's student Alex Powell. It is jointly supervised by Drs. Rossignac and Shaw.
-
- **GeoFilter**: The project focuses on new technologies allowing the designer to interactively attenuate or emphasize features of a particular size throughout a surface. The user selects one such feature by touching it and spreading a selective paint over it using dynamic flow on the surface. Then, the selected feature is measured automatically and the measure is used to compute the parameter of a rational quadratic filter capable of exaggerating or attenuating selected shape frequencies. This investigation was carried out by PhD Student Byung-Moon Kim under the supervision of Dr. Rossignac.
-
- **Tritops**: This project explores a new force-feedback device for the two-hand tactile exploration and haptic editing of surfaces. It was conducted by Master's student (Gordon Brown) under the joint supervision of Drs. Rossignac and Shaw. Through a collaboration with students and staff from ME, the team has designed, built, and refined a prototype of the device and has integrated it with Twister for preliminary testing. Usability tests have revealed interesting challenges for haptic interaction.
-
- **FlowFixer**: We anticipate that the Digital Clay will be capable of simulating not only the interaction with solid shapes, but also the interaction with responsive media, such as fluids. Hence, we are exploring new simulation techniques that strive for a compromise between accuracy, simplicity, and speed. This project is being carried out by PhD Student ByungMoon Kim and supervised by Dr. Rossignac.